5-9-2014

Structural Health Monitoring of an In-Service Highway Bridge with Uncertainties

Jingcheng Li
invinciblehs@gmail.com

Structural Health Monitoring of an In-Service Highway Bridge with Uncertainties

Jingcheng Li, Ph.D.

University of Connecticut, 2014

In recent years, structural health monitoring (SHM) has become increasingly important for the assessment and maintenance of aging infrastructure. However, some challenges remain in applying SHM in the field. For example, high cost of wired sensors limits the SHM application to small number of structures within a network. Wireless smart sensors (WSSs), on the other hand, provide a versatile, cost-effective method of monitoring dynamic conditions of structures in near real-time. While the wireless sensor technology has been available for nearly a decade, there have been limited numbers of full-scale applications due to its intrinsic limitations such as power supply issue. In this dissertation, based on the power consumption of the Imote2 wireless sensor platform, a vibration-based piezoelectric energy harvester has been developed and validated.

The feasibility of structural monitoring by means of a WSS system has been validated using a lab-scale truss bridge and an in-service highway bridge in Meriden, Connecticut. The results from the WSS system have been compared with the results from traditional wired sensors as well as finite element model to show the efficiency of SHM using WSSs.

One of the major objectives of SHM is to detect damage in the monitoring structures based on changes in their mass, damping, and stiffness. These parameters are also affected by operational and environmental variability, which challenge the reliability of damage detection. In this study, a full year

monitoring results from a long-term SHM system on the Meriden Bridge is presented. Especially, the variations in the identified modal frequencies have been observed, and these changes have been shown to be strongly correlated with temperature measurements.

The ultimate goal of this research is to detect structural damage in presence of uncertainties. In order to achieve this goal, damage detection procedure based on machine learning algorithms has been developed. Two machine learning algorithms have been employed: a linear algorithm based on the Mahalanobis Squared Distance (MSD), and a nonlinear algorithm based on the Auto-Associative Neural Network (AANN). The MSD and AANN algorithms have been tested on the lab-scale truss bridge as well as the one-year monitoring data measured from the Meriden Bridge.

Structural Health Monitoring of an In-Service Highway Bridge with Uncertainties

Jingcheng Li

B.S., Huazhong University of Science and Technology, 2009

M.S., University of Connecticut, 2011

A Dissertation

Submitted in Partial Fulfillment of the

Requirements for the Degree of Doctor of Philosophy

at the

University Of Connecticut

2014

APPROVAL PAGE

Doctor of Philosophy Dissertation

Structural Health Monitoring of an In-Service Highway Bridge with Uncertainties

Presented by

Jingcheng Li, B.S., M.S.

Major Advisor: _____

Dr. Shinae Jang

Associate Advisor: _____

Dr. Jiong Tang

Associate Advisor: _____

Dr. Richard Christenson

Associate Advisor: _____

Dr. Michael Accorsi

Associate Advisor: _____

Dr. Kay Wille

University of Connecticut

2014

ACKNOWLEDGEMENT

I feel so lucky of coming to the University of Connecticut (UConn) and pursuing my M.S. and Ph.D. degrees in the past five year, which has been most exciting period of my life.

First of all, I would like to thank my advisor, Professor Shinae Jang, for her support throughout my Ph.D. study and research. She gave me this fantastic opportunity and spared no effort to provide me guidance along my journey. She has also been a good friend sharing her time, experience and knowledge to help me achieve my goal.

I am greatly indebted to my committee members, Professor Jiong Tang, Professor Richard Christenson, Professor Michael Accorsi, and Professor Kay Wille. Many thanks to Professor Jiong Tang and Professor Richard Christenson, my research and work in this dissertation would not have been possible without their research collaboration. I would also express my appreciation to Professor Michael Accorsi, and Professor Kay Wille for serving as both of my M.S. and Ph.D. committee members.

I thank my colleagues at the Smart Infrastructure Lab. Especially I would like to acknowledge Sushil Dahal and Priscilla Mensah-Bonsu. Their work on SHM with WSSN provided the foundation of this research. Many thanks go to Edward Eskew, Chenhao Jin, and Rosana Martinez-Castro for their help. Most importantly, I appreciate their friendship during my time at UConn.

I would like to acknowledge the generous assistance offered by my colleagues from the Department of Mechanical Engineering, Qi Shuai, Matthew Cremins, Jiawen Xu, Ji Zhao and Kai Zhou, with whom I collaborated to create the energy harvesting framework presented in this research.

I am very thankful to Dr. Sarira Motaref and Masoud Mehrraoufi on my research of the Meriden Bridge. Their valuable advice and extensive knowledge are very much appreciated.

I thank my other colleagues at UConn, Dr. Iliya Yut, David Jacobs, Zhaoshuo Jiang, Majid Cashany, and Kan Xiao. The entire experience at UConn would not have been so much exciting without them.

I am extremely grateful to my parents for their endless support and encouragement during my study at UConn. Never once did they question my pursuit of the goal in my life.

Last but most importantly, there are not enough words to express my gratitude to my fiancé, Siyuan. I can't imagine my life at UConn without her. I appreciate her endless love, support and confidence in me.

TABLE OF CONTENTS

LIST OF FIGURES

LIST OF TABLES

CHAPTER 1 INTRODUCTION

1.1 Motivation of Structural Health Monitoring (SHM)

Civil infrastructure is the foundation of modern society and is directly related to the economic success of a nation. However, much of civil infrastructure like buildings, bridges, offshore oil platforms and other lifeline systems deteriorate with time due to various reasons including fatigue failure caused by environmental factors, and extreme events such as an earthquake. In addition, many of these structures are currently nearing the end of their original design life. The situation of aging infrastructure has become a national concern, especially for highway bridges in the United States. According to the 2013 Report Card for America's Infrastructure, the Federal Highway Administration (FHWA) calculates that more than 24.9 % of the nation's 607,380 bridges are either structurally deficient or functionally obsolete (ASCE 2013). Therefore, how to continuously evaluate the structural condition, detect existing damage in bridge structures at the earliest possible time, and timely maintain the aging bridges is critical so that the bridges can continue to be safely used, and further improve the public safety.

In order to maintain the safety of highway bridges, all the states in the United States are mandated by the National Bridge Inspection (NBIS 1998) program to periodically, usually once every several years, inspect all highway bridges. To date, the primary way used to perform these inspections is schedule driven and relies on visual inspection. However, such visual inspections have limited efficiency and reliability. The variation of inspector's experience and invisibility of serious damage can make the damage be overlooked, whereas the propagation of the damage between two inspections can potentially put the bridge at risk (FHWA 2001). Therefore, a much more effective and reliable way to monitor and assess the integrity and functionality of the nation's bridges is needed.

Structural health monitoring (SHM) provides a way to continuously capture structural response and assess structural condition in real-time. It is a process of implementing a damage detection strategy to a structure, which involves inspection of the structure using spaced measurements, extraction of damage-sensitive features from the measurements, and analysis of these measurements to determine the current

damage state of the monitored structure (Wenzel 2009). SHM can be applied to characterize loads *in situ*, thereby be useful to predict the structural response due to extreme loading condition. SHM can also be used to access post-extreme event condition due to natural hazards or man make disasters. This could potentially allow the authority to get access to the affected area faster and eventually reduce economic and social impact of damage. In summary, SHM has great advantage against the traditional visual inspection in terms of real-time monitoring and assessment, timely maintenance practices, and rapid response after extreme event.

1.2 Existing SHM Methods and Challenges

The essential purpose of the SHM for bridge structures is to detect the existing damage in the systems. The damage can be defined as changes in material properties and/or geometric changes such as boundary conditions and system connectivity. Vibration-based SHM methods for bridge structures have evolved in 1980s. The vibration-based SHM method is based on tracking changes in structural characteristics, such as mass, stiffness and damping. By studying and comparing the changes in monitored vibration response between initial and current structural condition, the unknown damages of structural properties can be identified (Farrar and Worden 2013).

The procedure of vibration-based SHM methods consists of measurement of structural dynamic response, characterization of an initial bridge condition, continuous monitoring the dynamic response of bridge structures, and evaluation of current bridge condition compared to the initial condition. The measurement of structural dynamic response is achieved by data acquisition systems installed on the bridges. This portion of the SHM for bridge structures involves selecting the excitation method, the sensor types, number of sensors, and data acquisition, storage and transmission hardware. While most vibration-based SHM methods require both input and output excitation, measuring input excitation from a bridge is quite difficult due to the uncertain nature of bridge loading. Thus, research on vibration-based SHM methods have been focused on the use of only ambient vibration data (Sohn 2003).

Bridges are individual structures that have very little in common with each other in terms of type and size, so the data acquisition system, type of sensors, and number of sensors will be different for different bridges. How to determine the data acquisition system, especially for the number of sensors, is a big challenge in applying SHM methods on bridge structures. This is even more difficult when the budget for deploying SHM system is limited. For example, a total number of 236 sensors with seven different types were installed on the Ting Ku Bridge, Hong Kong, China, in 1998 to monitor the structural health and performance under in-service conditions (Wenzel 2009). The bridge is one of the limited instances of using multi-span cable-stayed bridges in practice. It comprises two main spans of 448m and 475m, respectively, and two side spans of 127m each. Almost at the same time, similar data acquisition systems were also installed on the 2.2km long Tsing Ma Bridge, Hong Kong, with more than 350 sensors to monitor the general health conditions of the bridge, in terms of structural durability, reliability and integrity. Over millions of USD were spent on the SHM systems.

In order to develop an effective data acquisition system with the capability of generating informative structural models and detecting critical damages, a dense array of sensors is desired to be installed on the structure (Rice 2009). This is because a dense sensor network will be helpful to gain a clear understanding of the structural behavior and better detect local damage such as corrosion, cracking, fracture, etc. However, due to limited budget, such a dense sensor network is difficult to implement with traditional monitoring systems. Traditional wired data acquisition systems are comprised of a network of sensors distributed throughout a bridge. These networks typically rely on a central station to take care of power supply and data acquisition and therefore require cables to collect the sensors with the central station. This makes such a system extremely costly, sometimes thousands of dollars per sensor. (Rice 2009).

Developments in wireless technology have made much lower-cost wireless smart sensor network (WSSN) an attractive alternative to traditional wired monitoring systems. The cost of wireless smart sensor (WSS) unit used in the monitoring system could be only hundreds of USD compare to thousands of in the wired system (Jang 2010). This makes the scalability of SHM system to a large network with dense array of sensors on bridge structures. A total number of 71 wireless sensor nodes with 427 sensor

channels were installed on the Jindo Bridge in South Korea in 2009. The Jindo Bridges are twin cable-stayed bridge with each of them consists of a 344m central main span and two 70m side spans. It is, up to date, the largest WSSN application on a full-scale bridge in the world. This project provided an important insight into the potential use of wireless technology for long-term bridge monitoring (Jang et al. 2011).

However, one of the biggest challenges for the long-term bridge monitoring with WSSN is how to supply power to the WSS nodes. A solar panel was applied to the wireless sensors in the Jindo bridge project, and reasonable results were obtained to increase the battery life (Jang et al. 2011). However, for those places where sunshine is not enough, solar power might not be an efficient way for supplying power. For an alternative way, vibration-based energy harvesting by using piezoelectric materials could be a potential solution since it is available to convert vibration energy to electrical energy.

When a SHM system is installed on a field bridge which is exposed to outside environment, the damage detection process will have to deal with uncertainties from operational and environmental influence. The uncertainties from operational condition include live traffic, while environmental condition includes temperature and moisture. Without considering this, changes in the measured response caused by operational and environmental variability may be mistaken as an effect of damage (Farrar and Worden 2013). Therefore, when operational and environmental variability is an issue, how to separate changes in the measured system response caused by the variability from changes caused by real damage is also a challenge to the field implementation of a robust SHM system.

1.3 Objectives and Organization of Dissertation

The objective of this research is to provide field deployment of SHM system on bridge damage detection with uncertainties. The contributions of the research are the development of vibration-based energy harvesting system, implementation of WSSN on bridge SHM, and application of machine learning algorithms on bridge damage detection with uncertainties. The following paragraphs outline the contents of the research presented in this dissertation.

Chapter 2 provides the background information in this research. It includes state-of-art of SHM and its applications to real world followed by a review of existing WSSNs. Since one of the main focuses in this dissertation is implementation of WSSN, a summary of vibration-based energy harvesting system is provided. A brief review of vibration-based damage detection methods used in SHM system will be presented. The methods to detect damage in presence of operational and environmental variability are also discussed in Chapter 2 of this dissertation.

A vibration-based piezoelectric energy harvesting system is described in Chapter 3. The wireless smart sensor used throughout this dissertation Imote2 is firstly introduced. Then, the power consumption of the Imote2 wireless node under different applications is evaluated. Next, the design of a vibration-based wide-band piezoelectric energy harvester with target power generation value, is discussed. The energy harvesting system is assembled by multiple pieces of bimorph piezoelectric cantilever beams with different resonant frequencies. This design enables the energy harvesting system to continuously supply similar amount of energy at a particular frequency range.

Chapter 4 shows the implementation of WSSN on full-scale bridge SHM. The deployment of WSSs on an in-service highway bridge demonstrates how the WSSN is used for bridge health monitoring. The design and deployment of WSSN are discussed in detail. In addition, a long-term wired monitoring system with multiple types of sensors has also been installed on the highway bridge for full-scale implementation. A FE model of the highway bridge is also developed in SAP2000. System identification results from the two monitoring systems and FE model are also compared in this Chapter.

The temperature effects on the natural vibration frequencies of bridges are discussed in Chapter 5. The discussion is based on a full-year monitoring data from the long-term wired monitoring system installed on the highway bridge. Regression analysis with linear and nonlinear fit is employed to study the relationship between temperature and natural frequencies.

Chapter 6 introduces a machine learning algorithm for damage detection with uncertainties. First, a brief summary of two machine learning algorithms – Mahalanobis Squared Distance and Auto-Associative Neural Networks - and the effect of operational and environmental variability on computation results are provided. Then, the two machine learning algorithms for damage detection with uncertainties are validated by a laboratory test of a 12-bay truss bridge. Finally, the two machine learning algorithms are applied to analyze the one-year monitoring data from the highway bridge.

Chapter 7 summarizes the research in this dissertation. Several important conclusions are drawn. In addition, potential future works are also discussed.

CHAPTER 2 BACKGROUND

This chapter provides a brief review of some important background related to this research. First, a survey of structural health monitoring (SHM) is given, followed by previous applications in the area of bridge health monitoring. Second, the background of wireless smart sensor (WSS) is presented. It includes an overview of existing wireless sensor platforms. Furthermore, an introduction of vibration-based energy harvesting system for WSS is provided. Moreover, existing vibration-based damage detection algorithms are shown followed by the limitations for full-scale bridge implementation. Finally, data normalization and machine learning algorithms are provided for damage detection under operational and environmental conditions. The objective of this chapter is to identify the hurdles that applying WSSs for full-scale bridge health monitoring in presence of operational and environmental variability.

2.1 Structural Health Monitoring

Structural health monitoring (SHM) is the implementation of a damage identification strategy to civil engineering infrastructure aimed at assessing the existing performance of the structure. It is mainly motivated by the potential life-safety and economic impact to the public society. It can be also motivated to understand complex load-response relationships, assess novel construction or design techniques, evaluate the condition of a structure following an extreme loading event, monitor construction procedure, evaluate retrofit measures and monitor long-term structural degradation of deterioration (Farrar and Worden 2007, Brownjohn 2007).

According to the 2013 ASCE Report Card for America's Infrastructure, over 24.9% of the bridges in the United States are structurally efficient or functionally obsolete. The average age of the nation's bridge is currently 42 years which almost reaches their 50 years design life. Figure 2.1 shows the number of structural deficient and functionally obsolete bridges from 2005 to 2012. Figure 2.2 presents the distribution of structural deficient and functionally obsolete bridges over the United States. Twenty two states have a higher percentage of structurally deficient bridge compares to national average. Though the

overall number of structural deficient and functionally obsolete bridges continues to decline, there is still a lot works to decrease the total number from 24.9% to below 15% over the next decades (ASCE 2013).

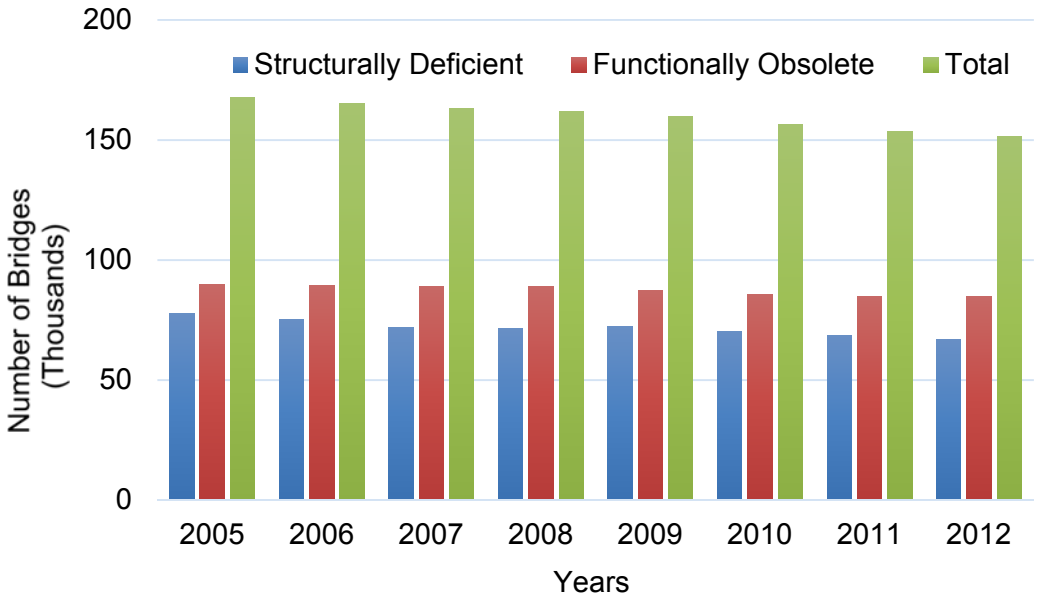

Figure 2.1 Structural deficient and functionally obsolete bridges by year (ASCE 2013)

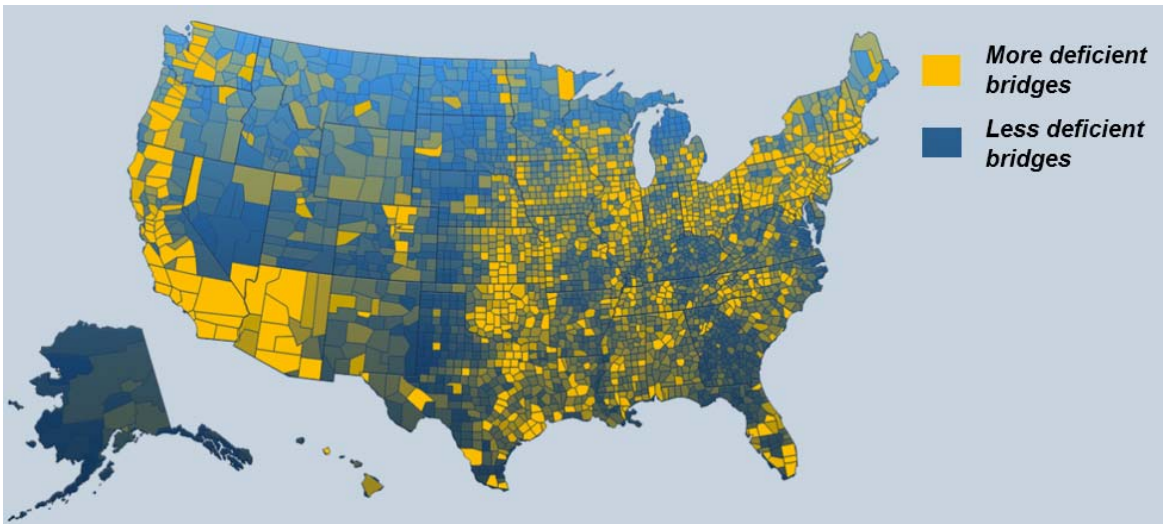

Figure 2.2 Deficient bridges in the United States (ASCE 2013)

In general, damage in structures can be defined as changes to the material and/or geometric properties such as boundary conditions and system connectivity that affect the current or future performance of these structures. Damage begins at the material level progresses to component and system level at various rates under different loading scenarios. Those system level damage cause structure failure when the damage progresses to a point where the system can no longer perform its ordinary functions. In this case, the damage is associated with fatigue or corrosion. This situation can be found from various bridge collapses (Doebling et al. 1998).

The damage identification process is generally summarized into the following five-step procedure:

1) Verify of presence of damage
2) Identify of the location of damage (where is location of the damage;
3) Classify the damage type.
4) Determine severity of damage
5) Assess the remaining service life of the structure.

An early practice of SHM can be found in the aerospace industries, which assessed the condition of materials and structural components by using non-destructive evaluation (NDE) methods (Doebling et al. 1998). This method employs a high-speed wave sent through a structure and observes the response signal to determine the structure condition. An extensive literature has been published on SHM over the last three decades, which shows increase in importance of SHM for condition assessment. Different from the NDE method which limited to local damage detection, existing SHM is rather a global damage approach to the assessment of civil engineering infrastructure. Changes in structural characteristics, such as mass, stiffness and damping, will affect the global vibration response of the bridges. By studying and comparing the changes in monitored vibration response between initial and current structural condition, the unknown damages of structural properties can be identified. Two comprehensive reviews of the SHM for more detailed discussions are in Doebling et al. (1998) and Sohn et al. (2002).

Multiple full-scale SHM applications have evolved over the last few decades. The motivations for those implementations are varying from short-term assessment to long-term monitoring. Dynamic responses are measured in terms of acceleration, strain, or displacement. Due to different measurements, sensor types, and sensor density are also different for different projects. With the development of SHM, more and more new structures install SHM system during construction and keep the system for long-term monitoring after the construction is done. Due to the development of wireless technology, long-term bridge monitoring using WSS is also promising in near future. The following paragraphs provide examples of traditional wired bridge SHM implemented in the last few decades. The application of WSS in SHM is presented in next section.

Several monitoring efforts have been made to the Golden Gate Bridge in the San Francisco, CA. A SHM system including 28 accelerometers with 12 on the main span, 10 on the pier-lower structures and 6 on the side span were installed on the bridge by Abdel-Ghaffar et al. (1985). The natural frequencies, mode shapes and effective damping of the bridge were determined in order to understand and predict the bridge's dynamic performance under wind and earthquake loading. A good agreement was found between the measured results and calculated results.

A short-term assessment of the Alamosa Canyon Bridge in New Mexico was conducted by Doebling and Farrar (1997) and Farrar et al. (1997). A total number of 31 accelerometers and 5 temperature sensors were installed on the bridge. Two different vibration sources were introduced to the bridge included ambient vibration and impact hammer. The results in terms of modal frequencies and mode shapes from two vibration sources were compared. In addition, the dynamic performance of the bridge due to variable environmental factors was also studied. A fluctuation of about 5% in the natural frequency was observed over a 24-hour period due to temperature changes.

The dynamic performance of the Hakucho Bridge in Japan under wind loads was studied by Abe et al. (2000). The time domain method was applied to calculate the natural frequencies, model shape and effective damping. Similar research was also conducted on the Humber Bridge in the UK by Brownjohn (2007). A total of 63 sensors were deployed on the bridge to evaluate the aeroelastic properties of the

bridge under wind excitation levels. Other examples of short-term assessment are Melk Bridge M6 (Austria), Warth Bridge (Austria), Z24 Bridge (Switzerland), Pioneer Bridge (Singapore), I-40 Bridge New Mexico (USA) (Wenzel 2009).

Several full-scale applications of long-term bridge SHM have been implemented around the world. Hong Kong Wind and Structural Health Monitoring System (WASHMA) installed long-term SHM on three bridges: the Ting Kau Bridge, Kap Shui Mun Bridge, and Tsing Ma Bridge (Wong et al. 2000a, Wong et al. 2000b). A large amount sensors include anemometer, temperature sensor, accelerometer, strain gauge, displacement transducer, weight-in-motion sensor, global positioning system, Fiber Bragg Grating (FBG) sensors were installed on the bridges to monitor the dynamic response in terms of acceleration, displacement, strain, as well as environmental measurement includes wind and temperature. For example, an approximately 236 sensors were in the Ting Kau Bridge system, while over 350 sensors were in the Tsing Ma Bridge (Chan et al. 2006). By installing the long-term SHM system on these three bridges, the WASHMS is able to monitor the structural health condition of the three bridges, provide information for facilitating the planning of inspection and maintenance activities, and verify design assumptions and parameters for future construction of cable-supported bridges. Similar study can be found in the Bill Emerson Memorial Bridge in Cape Girardeau, Missouri, where a long-term monitoring system includes 84 accelerometer channels was also installed (Caicedo et al. 2002, Celebi 2006). The purpose of the project was to evaluate dynamic response of the bridge under seismic data and get insight view for future cable stayed bridge designs. Other examples of recent long-term SHM are the Tamar Bridge (UK) (Cross et al. 2013), the Xibin Bridge (Taiwan) (Yen et al. 2014), the Zhanjiang Bay Bridge (China) (Sun et al. 2013), the Huangpu Bridge (China) (Guo and Yan 2014).

From previous review, SHM has been adopted to monitor mainly bridge performance under natural excitation such as earthquake, wind and other live loads using the wired sensing systems. However, those traditional wired monitoring system has shown three drawbacks: 1) it may disturb the normal operation of the structure due to wires run all over the structure; 2) the cost of the hardware is high; 3) the installation and maintenance costs are also high. For example, the cost of the SHM on the Tsing Ma suspension

bridge in Hong Kong was over $8 million, which was thousands of dollars per monitoring channel (Farrar 2001). Those drawbacks have limited the potential application of SHM on more bridges, especially for those with limited budget.

2.2 Wireless Smart Sensors for Bridge SHM

With the recent development of Micro-Electro-Mechanical Systems (MEMS), and network technology, wireless smart sensor network (WSSN) has shown significant potential for replacing conventional wired SHM systems. Compared to wired monitoring system, the SHM system with WSSN has shown some advantages: 1) lower cost for per channel monitoring; 2) easy installation and maintenance procedure; 3) on board computation capacity can be used for signal processing and mitigate the data inundation problem in densely instrumented system. (Spencer and Cho 2011, Jang 2010). For example, the wireless sensor installed on the Jindo Bridge cost less than $500 for per channel monitoring (Jang et al. 2011).

Many researchers have deployed WSS in full-scale bridge health monitoring. Early field validation of wireless technology for bridge monitoring was performed by Maser et al. (1996). Two levels of wireless communication strategies were included in their wireless monitoring system named Wireless Global Bridge Evaluation and Monitoring System (WGBEMS). The total cost of the wireless system was about $1000 per sensor node and $2000 for the data repository.

The performance of a wireless sensing prototype developed by Lynch el al. (2003) was validated on the Alamosa Canyon Bridge in New Mexico. A total number of 7 wireless sensors were installed to measure the bridge response to forced excitation induced by hammer. The wireless monitoring system took only half the time to install compared to the conventional wired SHM system.

Pakzad et al. (2008) designed and deployed a WSSN with 64 nodes on the Golden Gate Bridge in San Francisco for structural vibration monitoring and system identification. Each node has four channels. The data obtained from the wireless sensor nodes were used to examine the scalability of the network and the data quality. The test results showed accurate ambient vibration data from external environment for determining bridge vibration mode.

The largest WSSN implementation for bridge health monitoring was conducted on the Jindo Bridge in South Korea. A total number of 70 wireless sensor nodes with 427 sensor channels were installed on the bridge. The Jindo Bridges are twin cable-stayed bridge with each of them consists of a 344m central main span and two 70m side spans. This project provided an important insight into the potential use of wireless technology for long-term bridge monitoring (Rice et al. 2011, Jang et al. 2011, Cho et al. 2010).

Recently, a customized wireless sensor network platform with a flexible design was presented and applied on a highway bridge by Hu et al. (2013). The wireless sensor includes an S-Mote, an acceleration sensor board, and a strain sensor board. The monitored data were used to assess the network performance and structural response of the bridge. Experimental results show promising application of the SHM system with WSSN for continuous monitoring for the in-service highway bridge.

Example of WSSN on bridge health monitoring can also be found in many other literatures. Lynch and Loh (2006), Spencer et al. (2004) provide a comprehensive review on SHM with wireless sensor technology. Spencer and Yun (2010) also illustrate the advances of WSS for monitoring civil engineering infrastructure.

2.3 Vibration-Based Energy Harvesting

For a long-term application of WSSN for bridge health monitoring, a perpetual power supply need to be created to eliminate the need to frequently replace batteries. The process of extracting ambient energy and converting it to usable electrical energy is known as energy harvesting. Several energy harvesting technologies are available nowadays, however, an appropriate way to power the sensor nodes need to be selected carefully based on the constraints and requirements of the application.

The main sources of ambient energy are sunlight, wind, thermal gradient, vibration etc. A wealth of literature is available on energy harvesting from ambient energy. Glynne-Jones and White (2001), Roundy et al. (2004) and Paradiso and Starner (2005) reviewed possible energy source for energy harvesting, and compared the efficiency of various harvesting technologies. Among those, solar energy harvesting shows the most powerful energy efficiency. Many applications of solar panel for powering

wireless sensors are available (Raghunathan et al. 2005, Corke et al. 2007, Jang et al. 2011, Azarbayejani et al. 2011). However, one of the major drawbacks for solar power is the instability for power supply. For those places where sunshine is not enough, or with most cloudy days during a year, solar power may not be an appropriate solution for powering wireless sensors.

For bridge health monitoring with WSSN, vibration energy from the bridge induced by traffic is a large amount energy. How to harvest the vibration energy is a promising solution for supplying long-term stable energy to wireless sensors. In Williams and Yates's (1996) early work, three basic vibration to electric energy conversion mechanisms for microsystem are electromagnetic, electrostatic, and piezoelectric transductions. Beeby et al. (2006) and Cook-Chennault et al. (2008) reviewed over hundreds of publications that have appeared using these three mechanisms for energy harvesting. It can be found that among them piezoelectric transduction has received the greatest attention due to the main advantages of large power densities compared to electromagnetic and electrostatic, and ease of application. Development of piezoelectric material for energy harvesting can be found in several publications (Sodano et al. 2004, Anton and Sodano 2007, Abdelkefi et al. 2013).

Most piezoelectric energy harvesters are in the form of cantilever beam with unimorph (one piezoceramic layer) or bimorph structure (two piezoceramic layers). The piezoelectric cantilever beam is mounted on a vibrating structure and the dynamic strain induced in the piezoceramic layers result in an alternating voltage output across their electrodes. This structure usually vibrates at the resonant frequency to maximize power generation. duToit et al. (2005) investigated a bimorph piezoelectric energy harvester under different excitation frequencies. A maximum power of 200μW was measured at resonant with optimal resistance from 2.5m/s^2 base excitation. A bimorph piezoelectric cantilever beam generator with proof mass on the free end was developed by Roundy et al. (2003, 2004), and a power density of 70μW/cm^3 was demonstrated. After optimal design, the power density could be improved to be 250μW/cm^3 from a vibration source of 2.5m/s^2 at 120Hz. Erturk and Inman (2009) also studied the effect of proof mass on bimorph piezoelectric energy harvesting based on a distributed parameters model. A maximum power density of 6.8 (mW/g^2/cm^3) with an optimal resistor was measured. Adding proof mass

to the free end of piezoelectric cantilever beam can not only increase piezoelectric harvester's power generation efficiency, but also be used to tune the structural resonant frequency. It is a promising technology for piezoelectric cantilever structure.

In order to design a cantilever piezoelectric energy harvester which can provide considerable power to wireless sensors, a theoretical model for predicting the energy output is needed. In literature, single degree of freedom (SDOF) model and distributed parameter model based on Euler-Bernouli theory can be found to model such problem. The SDOF harmonic base excitation model was first described by Williams and Yates (1996) for electromagnetic energy harvester. Roundy et al. (2003, 2004) used the SDOF model to investigate the piezoelectric generator as a power source for wireless sensor. Meanwhile, the SDOF model was employed by Lu et al. (2004) to model and analysis of micro piezoelectric energy harvester for micro-electromechanical-systems applications. An electro-mechanical coupling was added in the model to take the electro mechanical effect in to account. Furthermore, duToit et al. (2005) presented a 1-D electromechanically coupled piezoelectric energy harvesting model based on the SDOF harmonic base excitation, and it was validated by a bimorph cantilever beam with a tip mass on the free end. Recently, the piezoelectric energy harvesting of bimorph cantilever beam with parallel and series connection were compared by Liao and Sodano (2008, 2010) based on an equivalent SDOF model. The model can accurately predict the energy output and optimal resistant when the system is excited at the resonant frequency.

On the other hand, the distributed parameter model based on Euler-Bernoulli theory was studied by some other researchers. A bimorph piezoelectric cantilever beam modeled by Euler-Bernoulli beam theory and Timoshenko beam equations was investigated by Ajitsaria et al (2007) for voltage generation. The general solution of a distributed parameters model based on Euler-Bernoulli theory for unimorph and bimorph cantilever beam generator from based excitation was then proposed by Erturk and Inman (2008, 2008a and 2009). The mathematical model was validated by experimental test. However, one of the major drawbacks of the distributed parameters model based on Euler-Bermoulli beam theory is that it is very complex. It is difficult to apply this model to design an appropriate piezoelectric energy harvester. Since

an equivalent SDOF solution with distributed parameters based on the work of Liao and Sodano (2008, 2010) is accurate enough to predict the power generation of piezoelectric energy harvester from base excitation, the equivalent SDOF model with distributed parameters is utilized in this study.

Since most piezoelectric cantilever beam designed at resonance, power generation decreases significantly out of resonant frequency. How to widen the working frequency of piezoelectric energy harvester is a challenge. Zhu et al. (2010) reviewed several strategies for increasing the operating frequency range of piezoelectric harvester. Using generator array by assembling multiple pieces of piezoelectric cantilever beams with different operating frequencies is a straightforward method. In Xue et al. (2008), by connecting multiple pieces of piezoelectric cantilever beams with different resonant frequencies in series, the operating frequency band of the piezoelectric harvester can be widened and shifted to the excitation frequency from ambient environments for more effective energy harvesting. Similar research has also done by Shahruz (2006). Therefore, a wide-band vibration-based piezoelectric energy harvester is much more robust in terms of power generation compared to single resonant piezoelectric harvester.

2.4 Vibration-Based Damage Detection Algorithms

The basic principle of vibration-based damage detection algorithm is that changes in structural characteristics, such as mass, stiffness and damping, will affect the global vibration response of the structure. Conceptually, the general procedure of the vibration-based damage detection consists of the following steps: 1) Measuring structural response, such as strain, acceleration, displacement; 2) Characterization of an initial bridge state based on monitoring data; 3) Continuing monitoring the bridge to get up-to-date data; 4) Evaluation of the up-to-date data to determine the damage with damage detection methods.

Damage detection methods based on various structural responses and characteristics such as natural frequencies (Cawley and Adams 1979, Patil and Maiti 2003), natural frequencies and mode shapes (Lee et al. 2002, Kim et al. 2003), modal strain energy method (Carrasco et al. 1997, Shi et al. 2002,

Seyedpoor 2012), parameter estimation method (Shin and Hjelmstad 1994, Pothisiri and Hjelmstad 2003), damage locating vector method (Bernal 2002, Gao et al. 2004), flexibility matrix method (Pandey et al. 1991, Huth et al. 2005, Li et al. 2010). This section is by no means intended as a comprehensive review of vibration-based damage detection algorithms, such an exercise has already been performed by Doebling et al. (1998), Sohn et al. (2002) and Fan (2011). They summarized various vibration-based damaged detection methods applied in SHM. Details for each method and their application to bridges, offshore platforms, and aerospace structures are provided in the reports.

2.5 The Effect of Uncertainties on Structure Modal Properties

One of the major limitations of many types of vibration-based damage detection algorithms is that many uncertainties from external environment can affect the structural properties, which make it hard to determine if changing of structural properties is caused by real damage or uncertainties. Uncertainties in the structural response can be associated with operational and environmental variability. Varying operational conditions include traffic, speed of operation, and changing excitation sources. Varying environmental conditions includes temperature, wind, and moisture (Figueiredo et al. 2010).

In terms of operational variability, the traffic on the bridge plays an important role, since a significant volume of the traffic on the bridge can increase the total mass of the structure, and consequently decrease the natural frequencies. Soyoz and Feng (2009) studied the traffic effect on modal frequencies of a box-girder concrete bridge located in Irvine, California. 10% variation of first natural frequency was found. Further investigation concluded that about 10% mass variation and about 5% variation of the natural frequency were caused by the traffic. Previously, the effect of vehicle weight on natural frequencies of three different bridges were also investigated by Kim et al. (2003). From their investigation, the measured natural frequency of the short span bridge changed up to 5.4% from traffic-induced vibration.

On the other hand, temperature is the greatest impact on structural properties in environmental variability (Xia et al. 2012, Nguyen et al. 2014) Temperature variations affect most material properties

(elastic modulus, mass density, yield stress, etc.), and cause geometric distortion of the structure from normal conditions. Farrar et al. (2000) investigated the temperature effect on modal frequencies from the Alamosa Canyon Bridge in New Mexico. An approximately 5% variation of the natural frequencies were found during 24 hours period. Peeters et al. (2001) analyzed one-year monitoring data from the Z-24 Bridge in Switzerland. 14% to 18% variation of the natural frequencies were explained by the temperature changes during that period. Recently, Moser and Moaveni (2012) performed a study on the continuous monitoring on the Dowling Hall Footbridge. Monitoring data from January 2010 to April 25 2010 were analyzed. The natural frequencies were observed to vary by 4% to 8% based on the measured temperature ranged from -14 to 39 ^{o}C.

From the literature, there is a wide array of uncertainties from operational and environmental variability influence the modal frequencies of bridge structures. Those impacts could be large enough to mask the changes from real damage in the structure and cause false assessment. Since structural response data will be continuously collected under varying uncertainties, the vibration-based damage detection methods will not be feasible to be applied on full-scale bridge monitoring without robust algorithms that are capable to normalize the effect of operational and environmental variability in the measured response data.

2.6 Data Normalization and Machine Learning Algorithms

As it is applied to SHM, data normalization is defined as the process of separating changes in the features derived from structural response data caused by damage from those caused by uncertainties. It is important for applying SHM technology on *in situ* structures. Currently, there are two well-known approaches in data normalization. The first approach consists of measuring operational and environmental parameters such as temperature, humidity, and traffic loads as well as structural vibration response at different locations. Then, regression analysis can be performed to parameterize the structural modal properties as a function of different operational and environmental parameters. With such a regression analysis, novelty detection processes can be utilized to detect damage when the measured up-to-date

structural response deviates from the normal condition that corresponds to the operational and environmental conditions. The second approach uses machine learning algorithms to develop models that assess the influence of operational and environmental variability from structural response data while no need to measure the operational and environmental parameters. Since it is virtually impossible to account for all operational and environmental parameters, the machine learning algorithm appears to be a natural approach for SHM purposes (Worden and Manson 2000, Worden et al. 2002, Worden and Manson 2007).

Machine learning is first defined by Arthur Samuel as a "field of study that gives computers the ability to learn without being explicitly programmed." (Cherkassky and Mulier 1998). It focuses on predicting unknown parameters from a training set of known properties. With regard to bridge health monitoring, machine learning is used to 'learn' the relationship among some damage-sensitive features derived from the undamaged bridge state (training data). If the relationship between these features is not similar to that in an undamaged state, an outlier, or say damage can be found. The machine learning algorithms used in data normalization usually fall into two categories. When training data available from both the undamaged and damaged structure state, supervised learning algorithms can be used; On the other hand, unsupervised learning problems arise when only data from undamaged structure state are available for training. Outlier or novelty detection methods based on unsupervised learning are the primary class of algorithms used in bridge monitoring because in most cases, only undamaged data are available (Farrar and Worden 2013).

A detail discussion of machine learning algorithms and the mathematical formulations can be found in Cherkassky and Mulier (1998). Even though these algorithms have different mathematical formulations, they are implemented in a common sequence of steps: 1) each algorithm is trained by damage sensitive feature vectors extracted from time-series data of undamaged structure under operational and environmental conditions; 2) all the machine learning algorithms transform the feature vectors into a global damage indicator which is invariant for feature vectors extracted from the normal condition; 3) setup threshold for certain level of significance; 4) calculate damage indicator for feature vectors extracted from damaged condition under operational and environmental variability. This damage indicator

should be classified as outlier if robust data normalization has been achieved. Figueiredo et al. (2010) applied four different machine learning algorithms for a building structural damage detection under simulated operational and environmental variability. The four algorithms are auto-associative neural networks (AANN), factor analysis, Mahalanobis squared-distance (MSD), and singular value decomposition. A direct comparison of their relative data normalization performance was conducted. In terms of overall performance, the AANN algorithm has some advantages in terms of finding nonlinear correlations among damage sensitive feature vectors, while the MSD algorithm has advantages for reduced computational efforts, and easy implementation since no assumptions are required to design network architecture.

In general, one can make progress in outlier detection by assuming a particular form for the probability distribution of the damage sensitive feature vectors that define normal condition. The MSD algorithm mentioned above is tailored to the Gaussian distribution and, therefore, depends on the assumption that the features can be characterized by the mean and variance. This is not always a case. However, if one is confident of Gaussianity, then it is easy to setup a rigorous confidence interval for an outlier detection. Two applications of the MSD algorithm on SHM are available in Worden and Manson (2007) and Noh et al. (2009).

The AANN algorithm is able to cope with non-Gaussian distribution assumption, which was first introduced by Kramer (1991). It is a feedforward, multilayer perceptron neutral network that maps the input on to itself through a hidden bottleneck layer. The network architecture contains three hidden layers which are mapping layer, bottleneck layer and de-mapping layer. Once the network has been trained using damage sensitive feature vectors from undamaged condition, the assumption is that the prediction error of the AANN will grow when the feature vectors that from a damaged condition are fed to the network. Despite the advantages dealing with non-linear correlation among feature vectors and non-Gaussian distribution assumption, the network architecture need to be designed appropriately to get better performance. This increases large amount work when the architecture is complex, and large data sets will increase computing time.

From literature, the MSD and AANN methods are widely accepted for data normalization. However, advantages and disadvantages of the MSD and AANN machine learning algorithms exist. In this research, these two methods will be implemented for *in situ* bridge damage detection. A comparative study of the two algorithms will also be performed.

2.7 Summary

This chapter provided the background of this dissertation on SHM, bridge health monitoring applications, wireless smart sensors for SHM, vibration-based energy harvesting system, vibration-based damage detection algorithms, effect of uncertainties on bridge modal properties, data normalization and machine learning algorithms. It showed the steady progression of SHM towards a long-term monitoring system to increase structural reliability and reduce potential tragedy.

Many examples of traditional wired monitoring systems have been used on bridge monitoring. However, the traditional wired SHM system is expensive and difficult to install on large scale bridges. The introduction of WSSs has opened the door to overcome the cost problem while remaining the versatile functionality. The advantages of SHM system with WSSN compared to traditional wired system have been shown in many field applications.

One of the problems in applying WSSN for long-term full-scale bridge monitoring is how to supply power to wireless sensors. Vibration-based energy harvesting provides a viable solution for continuous conversion of the vibration energy to the electrical energy. While piezoelectric cantilever beam systems appear to be widely used, most of those systems are designed for a resonant frequency. The power generation decreases significantly outside the resonance. Therefore, this research is concerned with design of a wide-band operational frequency range piezoelectric energy harvesting system.

The core objective in SHM is to detect damage in the structure. Numerous vibration-based damage detection algorithms have been developed. However, one major drawback of those methods is lack of considering uncertainties from operational and environmental conditions such as temperature, humidity, traffic etc. Without a robust normalization method, it is not easy to separate changes in the features

derived from structural response data caused by damage from those caused by uncertainties. The machine learning algorithms in data normalization provide a solution to detect damage without direct measuring operation and environmental parameters. Two main machine learning algorithms for detecting bridge damage with uncertainties - MSD and AANN - are implemented in this research.

CHAPTER 3 VIBRATION-BASED ENGERGY HARVESTING SYSTEM FOR WIRELESS SMART SENSORS

3.1 Introduction

This chapter describes the process of developing a wide-band piezoelectric energy harvester for WSSs. Since the relationship between power consumption and supply is important for an effective design of the energy harvester, the energy consumption of the Imote2 wireless sensor platform for typical SHM applications has been evaluated in this dissertation. Based on the demand, a wide-band vibration-based piezoelectric energy harvester is developed to supply power for the system. A mathematical model for predicting power generation of the piezoelectric harvester is first given. Then the feasibility of the wide-band piezoelectric energy harvester is experimentally validated.

3.2 Evaluation of Imote2 Wireless Sensor Node

3.2.1 Description of Imote2 wireless sensor node

The WSS platform used in this research is Imote2 which was developed by Crossbow (2007). The advantage of its high processor speed and large RAM size make it an ideal wireless platform for high-frequency sampling and intense data processing required for SHM. An Intel's X-scale processor (PXA271) is embedded on the Imote2 board, and can run at different speeds depend on application requirement, resulting in different power consumption. The maximum CPU speed of the Imote2 is 416MHz. In addition, the memory size is 256k for SPAM, 32 MB for FLASH and 32MB for SDRAM (Rice 2009). A picture of the Imote2 can be found in Figure 3.1.

Figure 3.1 Imote2, top (left) and bottom (right)

The SHM-A sensor board developed by the Illinois SHM Project (ISHMP) has been employed for sensing and data acquisition, connected to the Imote2 (ISHMP 2009). The SHM-A sensor board has three axes accelerometers (LIS344ALH), a temperature/humidity (SHT11) sensor, and a light sensor (TSL2561). A 4-channel Quickfilter (QF4A512) signal conditioner and an ADC are also available on the board. A detailed description of the sensor components can be found in Rice and Spencer (2009). A picture of the SHM-A sensor board is presented in Figure 3.2. A stacked sensor node with Imote2 sensor platform and SHM-A sensor board is shown in Figure 3.3.

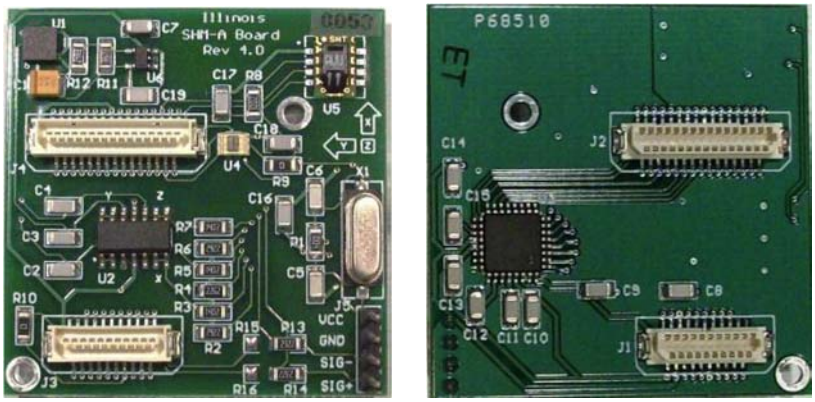

Figure 3.2 SHM-A sensor board, top (left), and bottom (right)

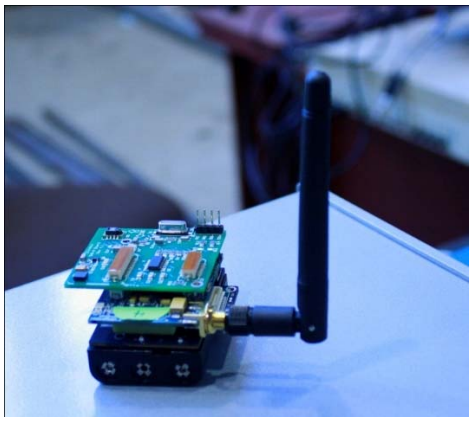

Figure 3.3 Wireless sensor node with Imote2 and SHM-A (Dahal 2013)

The software core of the Imote2 for SHM is the ISHMP Services Toolsuite including three primary categories: *foundation services*, *application services*, *tools and utilities*. It is open source and free to download from ISHMP website (shm.cs.uiuc.edu/software.html). For completeness, this section summarizes each component of the ISHMP Toolsuite shown in Rice (2009).

Foundation services support gathering synchronized sensor data, communicating reliably data, and providing accurate timestamps. Four main foundation services are unified sensing, time synchronization, resampling, and reliable communication services.

Application services provide numerical algorithms, like correlation function estimation (CFE), eigensystem realization algorithm (ERA), stochastic subspace identification (SSI), Stochastic damage locating vector (SDLV), and frequency domain decomposition (FDD) to implement SHM application on the Imote2 sensor node.

Tools and utilities are used for large-scale long-term WSSN implementation. They are necessary to evaluate the network conditions at structures, determine appropriate values of system parameters, and most importantly, assess power consumption and longevity issues. The applications can be categorized as those operating on a single wireless sensor node or those on multiple nodes. The single node application include *autocomm* (a terminal program for interfacing with the Imote2 through the Imote2 interface board's USB port), and *SnoozeAlarm* (energy saving strategy using a sleeping mode, and frequent wake

for maintaining network functionality). A typical *SnoozeAlarm* application consists of cycles of deep sleep and wake up. Sometimes it is not necessary to continuously collect data from the structure all the time, the data can be collected once in a while, for example, once in one hour. In this case, WSSs will be in *SnoozeAlarm* condition for most of time. Once it is waked up every hour, it will collect data, transmit data and then go back to *SnoozeAlarm* condition again. This can significantly reduce the power consumption of WSSs, which is very important for long-term SHM applications.

The multiple nodes application in higher level network operation includes *RemoteSensing*. The *RemoteSensing* provides a high level of flexibility in the choice of sensing and network parameters. The network is synchronized prior to sensing, and timestamped data is collected then. It is applicable to single-hop and multi-hop communication.

3.2.2 Power consumption of the Imote2 sensor node

The amount of power that the Imote2 consumed is based on the power consumption of different working states. The Imote2 includes the PXA271 processor which can run at varying speeds depends on application requirements, resulting in different power consumptions. With battery board and sensor board attached, the Imote2 has five primary power consumption states which are:

- Deep sleep mode
- Startup – initial state when Imote2 is turned on or wakes from deep sleep mode
- Imote2 processor at 13MHz (lowing operating speed)
- Imote2 processor at 104MHz (intermediate operating speed)
- Imote2 sensing with the Imote2 processor at 104 MHz

For different applications, the average power consumption of the Imote2 sensor node is determined by the amount of time the sensor node in each power state in a given period time with some network and application parameters, which can be summarized into five categories: network parameters, sensing parameters, *SnoozeAlarm* times, *RemoteSensing* times, and *ThresholdSentry* times. How those parameters affect the overall power consumption of the Imote2 nodes in the wireless network can be found in Rice

(2009). In order to find the power consumption of the Imote2 node in real world application, an assessment of how much power is consumed in each power state was studied in this research. By using Crossbow battery board and SHM-A sensor board, the power consumption of each work states using one sensor node, sampling frequency 100Hz, sampling points 10000, and 3-channel accelerations can be found in Figure 3.4.

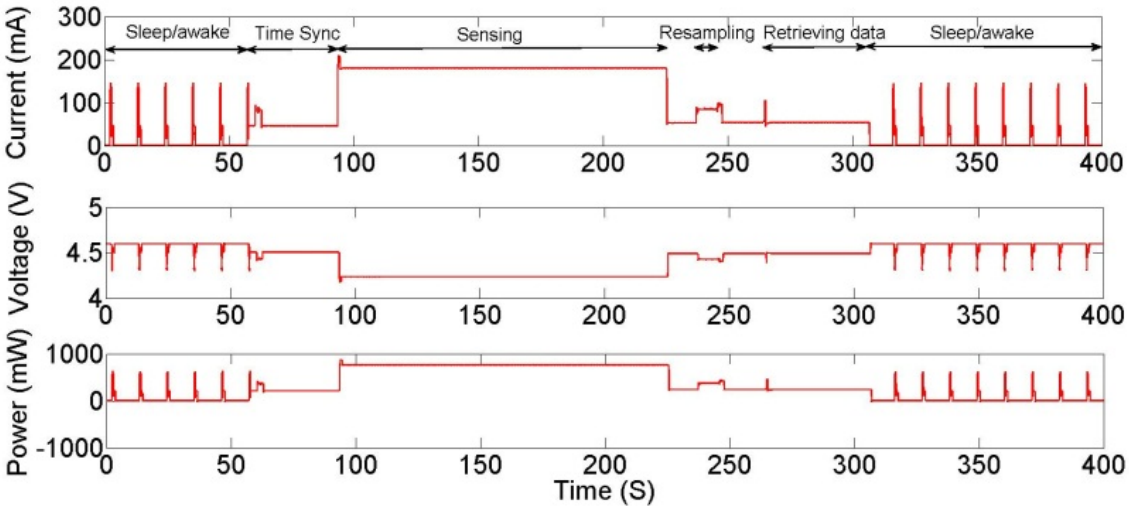

Figure 3.4 Power consumption in *SnoozeAlarm* and *RemoteSensing*

During the test, a constant voltage 4.6V was applied to the Imote2. In the *SnoozeAlarm* application, the sensor nodes can save a lot of power allowing the nodes to be in deep sleep/awake cycle in the majority of the time when they are not involved in other applications. The power consumption associated with the *RemoteSensing* includes waiting, sensing, and communication for each node. Most of the power is consumed in this state. The *ThresholdSentry* application operates on only those sensor nodes that are expected to measure the vibration of critical members such as a bridge middle span, so more power will be consumed by the sentry nodes. However, sensor nodes without the *ThresholdSentry* application will not consume extra power. The *ThresholdSentry* is not considered in the experiment test. A summary of average power consumption for each work states with *SnoozeAlarm* and *RemoteSensing* from Figure 3.4 and can be found in Table 3.1.

Table 3.1 Summary of power consumption and duration of power states for Imote2

Applications	Steps	Power States	Power (mW)	Time duration (s)
SnoozeAlarm	Deep Sleep	Deep Sleep	2.4	9.6
	Startup	Startup	630	0.7
	Startup	Idle@13MHz	208	0.7
RemoteSensing	Time synchronization	Idle@13MHz	208	30
	Extra wait time	Sensing@104MHz	764	21
	Extra sensing delay	Sensing@104MHz	764	13
	Sensing	Sensing@104MHz	764	100
	Wait time	Idle@13MHz	208	10
	Resampling	Idle@104MHz	380	17
	Retrieving data	Idle@13MHz	208	30

The average power consumption during a time period for the Imote2 is given by

$$P_{avg} = \frac{P_{slp}t_{slp} + P_{start}t_{start} + P_{13}t_{13} + P_{104}t_{104} + P_{sense}t_{sense}}{T} \tag{3.1}$$

where P_{slp} is Imote2 deep sleep power consumption, t_{slp} is total deep sleep time, P_{start} is Imote2 startup power consumption, t_{start} is total startup time, P_{13} is Imote2 idle at 13MHz power consumption, t_{13} is total time of idle at 13MHz, P_{104} is Imote2 idle at 104MHz power consumption, t_{104} is total time of idle at 104MHz, P_{sense} is Imote2 sensing at 104MHz power consumption, t_{sense} is total time of sensing at 104MHz, and T is total time at certain amount time.

From Equation (3.1), it can be found that, the overall total energy consumed by the Imote2 sensor node is determined by the power consumption and duration at each power state. The power consumption for each power state doesn't change once the hardware is chosen. While the duration for each power state is determined by different applications, for example how many *RemoteSensing* events in certain amount time. The more *RemoteSensing* events, the more power is consumed. Based on Equation 3.1 and data provided in Table 3.1, Figure 3.5 shows the average power consumption of an Imote2 wireless sensor nodes with different number of *RemoteSensing* events per day. The average power consumption was calculated based on one sensor node, sampling frequency 100Hz, sampling points 30000 (5 minutes monitoring data), and 3-channel accelerations for each *RemoteSensing* event. As can be seen from the

figure, the average power consumption of the Imote2 sensor node with 24 *RemoteSensing* events per day (one *RemoteSensing* event per hour) is about 103 mW. That means for a typical SHM system with WSSs, if 5 mins monitoring data is collected every hour, then at least average power 103mW should be generated from energy harvesting system.

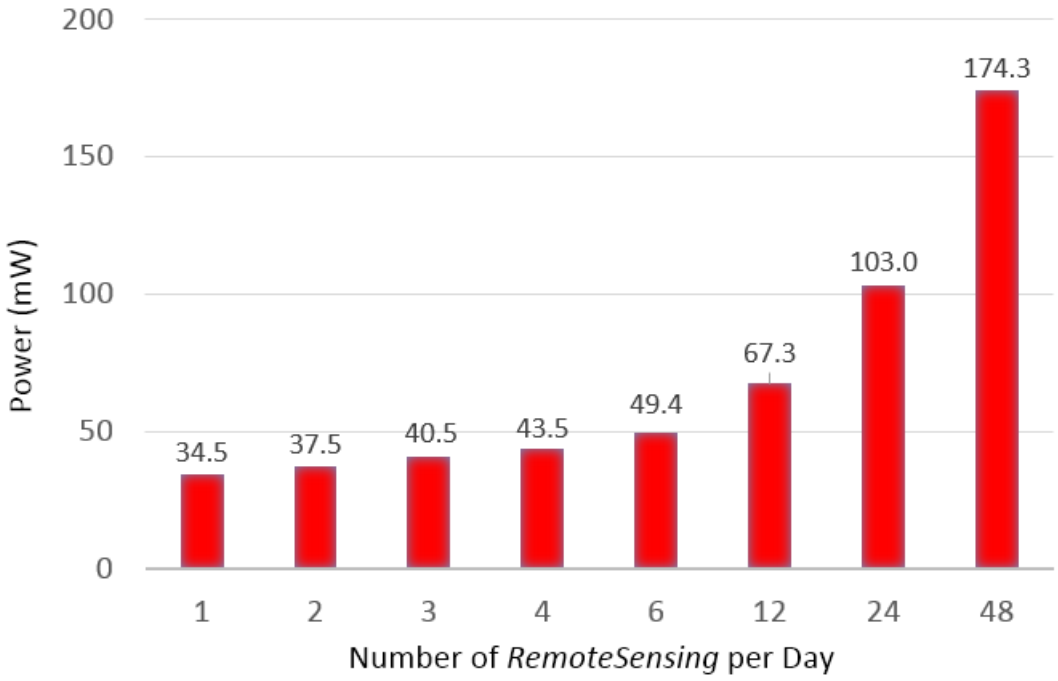

Figure 3.5 Average power consumption of Imote2 with different number of *RemoteSensing* per day

3.3 Design of a Piezoelectric Energy Harvesting System

3.3.1 Mathematical model

A typical piezoelectric cantilever beam is in the form of unimorph (one piezoceramic layer) or bimorph structure (two piezoceramic layers). The piezoelectric cantilever beam is mounted on a vibrating structure and the dynamic strain induced in the piezoceramic layers result in an alternating voltage output across their electrodes. A proof mass added at the end of free end can enhance tip displacement of the cantilever beam under base excitation, further increases the voltage output. For a bimorph piezoelectric cantilever beam, the two piezoceramic layers can be connected in series or parallel. A schematic of a bimorph

piezoelectric cantilever beam with proof mass can be found in Figure 3.6, t_p and t_b represents the thickness of the piezoceramic and substrate beam.

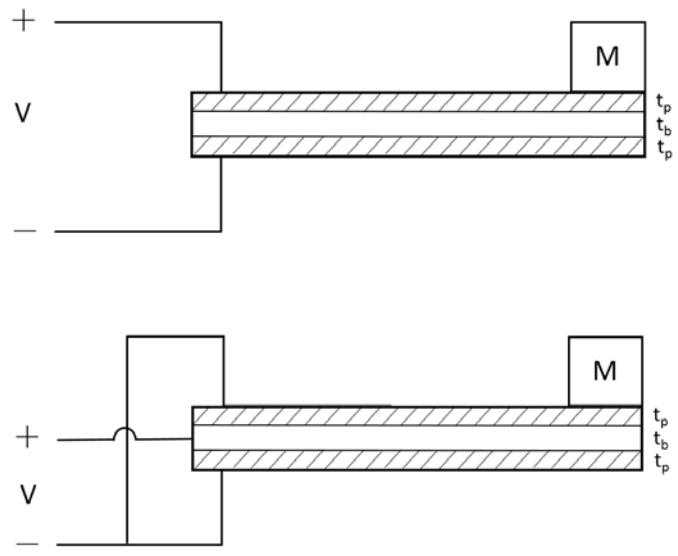

Figure. 3.6 Schematic of bimorph piezoelectric beam with serial (top) and parallel (bottom) connection

The mathematical model presented in this research for piezoelectric power harvester is an equivalent SDOF model. The coupled actuator and senor equations for electro-mechanical systems were derived by Hagood et al. (1999):

$$M\ddot{w}(t)+C\dot{w}(t)+Kw(t)-\theta v(t)=F_{ext}(t) \tag{3.2a}$$

$$\theta w(t)+C_p v(t)=q(t) \tag{3.2b}$$

where w is the displacement, v is the voltage, q is the charge across the electrode. M is the effective mass includes substrate beam mass, two piezoceramic layers and proof mass. K is the effective stiffness, C is the effective damping, θ is the effective electromechanical coupling, and C_p is the effective capacitance. The effective parameters can be defined as:

$$M_b=\int_{V_b}\varphi(x)\rho_b\varphi(x)\,dV_b,\ M_p=\int_{V_p}\varphi(x)\rho_p\varphi(x)\,dV_p,\ M_t=\varphi(L)m_t\varphi(L) \tag{3.3a}$$

$$M = M_b + M_p + M_t \tag{3.3b}$$

$$K_b = \int_{V_b} y^2 \varphi''(x) c_b \varphi''(x) dV_b,\ K_p = \int_{V_p} y^2 \varphi''(x) c_p \varphi''(x) dV_p \tag{3.3c}$$

$$K = K_b + K_p \tag{3.3d}$$

$$\theta = -\int_{V_p} y \varphi''(x) e^T \psi(y) dV_p \tag{3.3e}$$

$$C_p = \int_{V_p} \psi^T(y) \varepsilon^S \psi(y) dV_p \tag{3.3f}$$

$$C = \alpha M + \beta K \tag{3.3g}$$

where ρ is the density, c is the modulus of elesticity, ε is the dielectric constant, and e is the piezoeletric coupling coefficient. The subscripts b, p and t represents the substrate beam, piezoceramic, and tip mass, respectively. One thing needs to note that, when there is no tip mass at the free end, then the M_t will be zero in above equations. The superscript S, T, E denodes the parameter is measured at constant strain, stress, and electric field. $\varphi(x)$ is the model shape of the vibration beam. ψ(y) is the electrical field over the thickness of the piezoeletric, which is usually assumed to be constant. Proportional meterial damping C is added into the system through the constant α and β. If the excitation to the piezoeletric canliver beam is applied in the form of harmonic excitation, then effective external force to the system can be presented as:

$$F_{ext} = Aa(t) \tag{3.4}$$

where $a(t)$ is excitation accleration of the clamped end, and A is the effective input mass shown as:

$$A = \int_{V_b} \rho_s \varphi(x) dV_b + \int_{V_p} \rho_p \varphi(x) dV_p + M_t \varphi(L) \tag{3.5a}$$

$$a(t) = B\omega^2 \sin(\omega t) \tag{3.5b}$$

where B is the amplitude of the harmonic excitation, ω is the excitation frequency.

The mode shape of the cantilever beam can be defined as following:

$$\psi_r\left(\frac{x}{L}\right)=\left[\sinh\lambda_r-\sin\lambda_r+\frac{\lambda_r M_t}{M_b+M_p}\left(\cos\lambda_r-\cosh\lambda_r\right)\right]\left[\sinh(\frac{\lambda_r}{L}x)-\sin(\frac{\lambda_r}{L}x)\right]$$

$$+\left[\cosh\lambda_r+\cos\lambda_r-\frac{\lambda_r M_t}{M_b+M_p}\left(\sin\lambda_r-\sinh\lambda_r\right)\right]\left[\cosh(\frac{\lambda_r}{L}x)-\cos(\frac{\lambda_r}{L}x)\right] \quad (3.6)$$

where ψ_r is the mass normalized eigenfunction of the rth mode, λ_r is rth eigenvalue of mode which can be obtained from:

$$1+\cos\lambda\cosh\lambda+\lambda\frac{M_t}{M_b+M_p}(\cos\lambda\sinh\lambda-\sin\lambda\cosh\lambda)=0 \quad (3.7)$$

Since most of the vibration energy of the cantilever beam in transverse bending is located in the low frequency range around the first resonant frequency, and piezoelectric material generate both positive and negative voltages dependent on the strain direction, havesting energy from higher order modes is difficult wihout a segmented electrode due to charge cancelation, then the first mode shape is utilized in this research and can be normalized as:

$$\varphi(x)=\frac{1}{\sqrt{DL}}\psi_1\left(\frac{x}{L}\right) \quad (3.8)$$

where D is constant

$$\int_0^L\psi_1\left(\frac{x}{L}\right)\psi_1\left(\frac{x}{L}\right)dx=D \quad (3.9a)$$

$$\int_0^L\varphi(x)\varphi(x)dx=1 \quad (3.9b)$$

The first resonant frequency is given:

$$\omega_1=\sqrt{K/M} \quad \text{(rad/s)} \quad (3.10a)$$

$$f_1=\frac{1}{2\pi}\omega_1 \quad \text{(Hz)} \quad (3.10b)$$

Consider a bimorph piezoeletric cantilever beam shown in Figure 3.14, let the subscripts 1 and 2 represent the properties of the top and bottom piezoceramic, respectively, and subscript 0 rerepsent the substrate beam property. Then the coupled electromechanical equations for the piezoeletric beam are:

$$M_1\ddot{w}(t)+C_1\dot{w}(t)+K_1w(t)-\theta_1v_1(t)=F_{ext1}(t) \tag{3.11a}$$

$$\theta_1w(t)+C_{p1}v_1(t)=q_1(t) \tag{3.11b}$$

$$M_2\ddot{w}(t)+C_2\dot{w}(t)+K_2w(t)-\theta_2v_2(t)=F_{ext2}(t) \tag{3.12a}$$

$$\theta_2w(t)+C_{p2}v_2(t)=q_2(t) \tag{3.12b}$$

$$M_0\ddot{w}(t)+C_0\dot{w}(t)+K_0w(t)=F_{ext0}(t) \tag{3.13}$$

The effective actuator equation for the piezoelectric beam as a whole can be obtained by adding Equations (3.11a), (3.12a), and (3.13):

$$M\ddot{w}(t)+C\dot{w}(t)+Kw(t)-\left[\theta_1v_1(t)+\theta_2v_2(t)\right]=F_{ext}(t) \tag{3.14}$$

where M is total effective mass, C is the total effective damping coefficient, K is the total effective stiffness, and F_{ext} is the total effective external excitation force applied on the beam, the voltage and charge are related by:

$$v(t)=-R\dot{q}(t) \tag{3.15}$$

For a system with piezoceramic connected in series as shown in top Figure 3.14, the voltage and charges are:

$$v(t)=v_1(t)+v_2(t) \tag{3.16a}$$

$$q(t)=q_1(t)=q_2(t) \tag{3.16b}$$

where v and q represent the voltage drop and charge across the load resistor, respectively, and subscript 1 and 2 presents piezoceramic 1 and 2, respectively. Manipulation Equations (3.11a), (3.12a), (3.15) and (3.16), then apply the transfer function between the charge and acceleration in Laplace domain, then the

power dissipated by the resistor with serial connection system can be determined in the frequency domain as:

$$P^S = \frac{A^2 B^2 \omega^2 R}{\left(h_0^S - h_2^S \omega^2\right)^2 + \left(h_1^S - h_3^S \omega^3\right)^2} \tag{3.17}$$

where:

$$h_0^S = \frac{K\left(C_{p1} + C_{p2}\right) + \left(\theta_1 - \theta_2\right)^2}{\theta_1 C_{p2} + \theta_2 C_{p1}} \tag{3.18a}$$

$$h_1^S = \frac{C\left(C_{p1} + C_{p2}\right) + KC_{p1}C_{p2}R + \left(\theta_1^2 C_{p2} + \theta_2^2 C_{p2}\right)R}{\theta_1 C_{p2} + \theta_2 C_{p1}} \tag{3.18b}$$

$$h_2^S = \frac{M\left(C_{p1} + C_{p2}\right) + CC_{p1}C_{p2}R}{\theta_1 C_{p2} + \theta_2 C_{p1}} \tag{3.18c}$$

$$h_3^S = \frac{MC_{p1}C_{p2}R}{\theta_1 C_{p2} + \theta_2 C_{p1}} \tag{3.18d}$$

where the superscript $()^S$ is used to represent the seria. Connection, R is load resistor connected in the system. By letting the first derivative of the above equation to R be zero, the optimal resistance for maximum power can be determined:

$$R_{opt}^S = \frac{C_{p1} + C_{p2}}{\omega C_{p1} C_{p2}} \sqrt{\frac{\left(C\omega\right)^2 + \left[K - M\omega^2 + \dfrac{\left(\theta_1 - \theta_2\right)^2}{C_{p1} + C_{p2}}\right]^2}{\left(C\omega\right)^2 + \left[K - M\omega^2 + \dfrac{\theta_1^2 C_{p2} + \theta_2^2 C_{p1}}{C_{p1} C_{p2}}\right]^2}} \tag{3.19}$$

Similar to piezoeletric beam with serial connection, for a system with piezoceramic connected in parallel as shown in bottom Figure 3.14, the voltage and charges in the system can be found:

$$v(t) = v_1(t) = v_2(t) \tag{3.20a}$$

$$q(t) = q_1(t) + q_2(t) \tag{3.20b}$$

By manipulating Equations (3.11a), (3.12a), (3.15) and (3.20), then applying the transfer function between the charge and acceleration in Laplace domain, then the power dissipated by the resistor can be determined in the frequency domain as:

$$P^P = \frac{A^2 B^2 \omega^2 R}{\left(h_0^S - h_2^S \omega^2\right)^2 + \left(h_1^S - h_3^S \omega^3\right)^2} \tag{3.21}$$

where

$$h_0^P = \frac{K}{\theta_1 + \theta_2} \tag{3.22a}$$

$$h_1^P = \frac{C + K\left(C_{p1} + C_{p2}\right)R}{\theta_1 + \theta_2} + \left(\theta_1 + \theta_2\right)R \tag{3.22b}$$

$$h_2^P = \frac{M + C\left(C_{p1} + C_{p2}\right)R}{\theta_1 + \theta_2} \tag{3.22c}$$

$$h_3^S = \frac{M\left(C_{p1} + C_{p2}\right)R}{\theta_1 + \theta_2} \tag{3.22d}$$

where the superscript $()^P$ is used to represent the parellel connection. By letting the first derivative of the above equation to R be zero, the optimal resistance for maximum power can be determined to be:

$$R_{opt}^P = \frac{1}{\omega\left(C_{p1} + C_{p2}\right)} \sqrt{\frac{\left(C\omega\right)^2 + \left(K - M\omega^2\right)^2}{\left(C\omega\right)^2 + \left[K - M\omega^2 + \left(\theta_1 + \theta_2\right)^2 / \left(C_{p1} + C_{p2}\right)\right]^2}} \tag{3.23}$$

Comparing Equation (3.19) and (3.23), and manipulating Equation (3.17), (3.21) shows that the optimal resistances, power, voltage and current for the serial and parallel connection are related:

$$4R_{opt}^P\left(\omega\right) = R_{opt}^S\left(\omega\right) \tag{3.24a}$$

$$P^P\left(R, \omega\right) = P^S\left(4R, \omega\right) \tag{3.24b}$$

$$2V^P\left(R, \omega\right) = V^S\left(4R, \omega\right) \tag{3.24c}$$

$$I^P(R,\omega) = 2I^S(4R,\omega) \tag{3.24d}$$

From Equation (3.24), it can be found that for a given excitation frequency, the optimal resistance for generating maximum power in serial system is four time of that in parallel system. In addition, for an arbitrary resistance connected in the harvester system, the same amount of power can be generated by the serial system by using a resistance four times of that in parallel system; while the serial voltage is twice the parallel voltage, and serial current is half the parallel current.

3.3.2 Experiment test and model validation

The experiments have been conducted in laboratory to validate the feasibility of the mathematical model for predicting the energy output of the bimorph piezoelectric energy harvester. A bimorph piezoelectric material from Piezo System, Inc. (T226-A4-503X) was used in this study. The same type of material was studied by duToit et al (2005) and Erturk and Inman (2009). It consisted of two equal-size PZT-5H piezoelectric elements bracketing a brass substructure layer, and the piezoelectric elements were connected in parallel. The geometry and material properties of the piezoelectric energy harvester are presented in Table 3.2.

Table 3.2 Geometry and material properties of the piezoelectric energy harvester

Geometry	Symbol	Values	Material Property	Symbol	Values
Length (mm)	L	51.8	Brass modulus (GPa)	E_b	100
Width (mm)	b	31.8	Piezo modulus (GPa)	E_p	66
Brass thickness (mm)	t_b	0.14	Tip mass (kg)	M_t	0.002(each)
Piezo thickness (mm)	t_p	0.26(each)	Piezo dielectric constant (F/m)	$\bar{\varepsilon}_{33}^S$	$1550\varepsilon_0$
Brass density (kg/m3)	ρ_b	7630	Piezo strain constant (pm/V)	d_{31}	-190
Piezo density (kg/m3)	ρ_p	7800			

Two prototypes were developed which can be found in Figure 3.7. Design 1 only has the bimorph piezoelectric beam, while design 2 has two tip mass at the free end of the piezoelectric beam. Each of the tip mass is 2 gram.

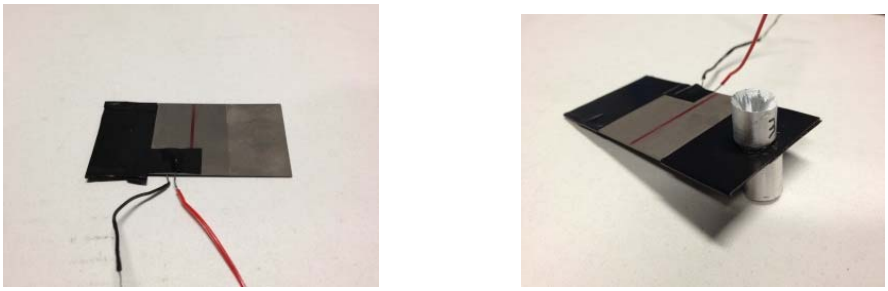

Figure 3.7 Piezoelectric energy harvester prototype design 1 without tip mass (left), design 2 with tip mass (right)

In the lab setup, one end of the bimorph cantilever beam was free, while the other end was excited from the base by a shaker connected to a function generator via a power amplifier, and the voltage generated was measured by connecting it to a data acquisition system. In addition, an accelerometer was placed on the clamped end of the piezoelectric energy harvester to measure the base acceleration. The load resistor was shunted between the piezoelectric elements. Figure 3.8 presents the experimental setup. In the figure, the data acquisition system hardware is from VibPilot and Smart Office Analyzer (SO Analyzer) is the software to control the VibPilot and is used to generate the excitation signal. An excitation signal is generated from the SO Analyzer and sent to the amplifier which is used to supply power to the shaker and also amplify the signal. The type of the amplifier is LDS PA1000L. A LDS permanent magnet shake V456 is also used in this study with the capacity of maximum force to be 110lbf peak sine thrust with a dynamic performance ranging from 5Hz to 7500Hz.

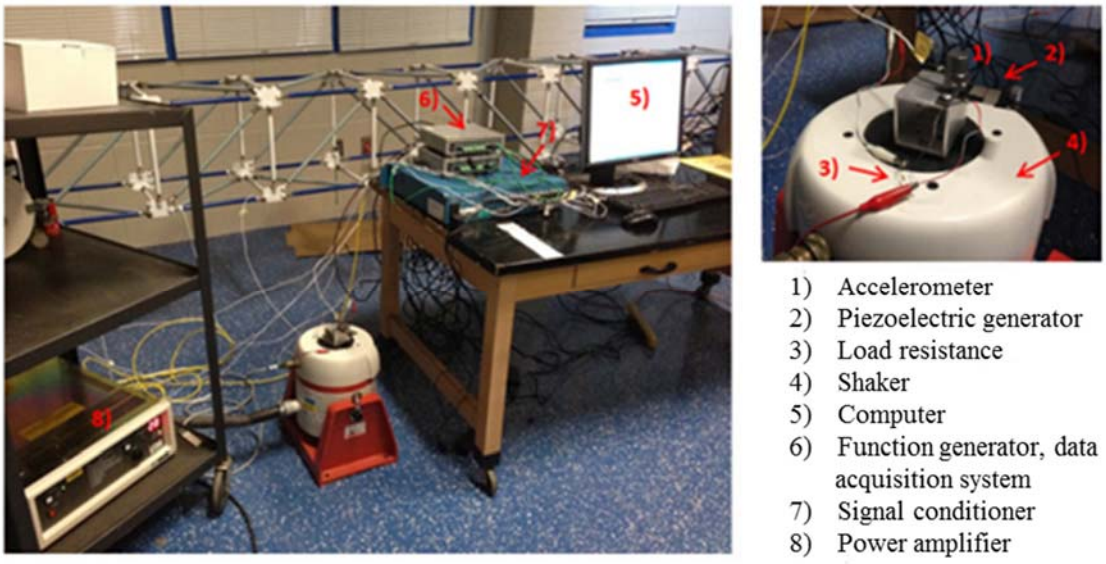

Figure 3.8 Experiment setup for model validation

Using the experimental setup described above, each of the piezoelectric beam was first tested under random excitation with frequency content 5Hz to 2048Hz to find out the resonant frequency. From the test, the measured first natural frequency of the two piezoelectric bimorph energy harvesters, design 1 and design 2, were 117.1Hz, and 65.2Hz, respectively, while those were predicted by the mathematical model to be 116.1Hz, and 67.8Hz, respectively. The power spectra density of the two piezoelectric designs from test results is shown in Figure 3.9.

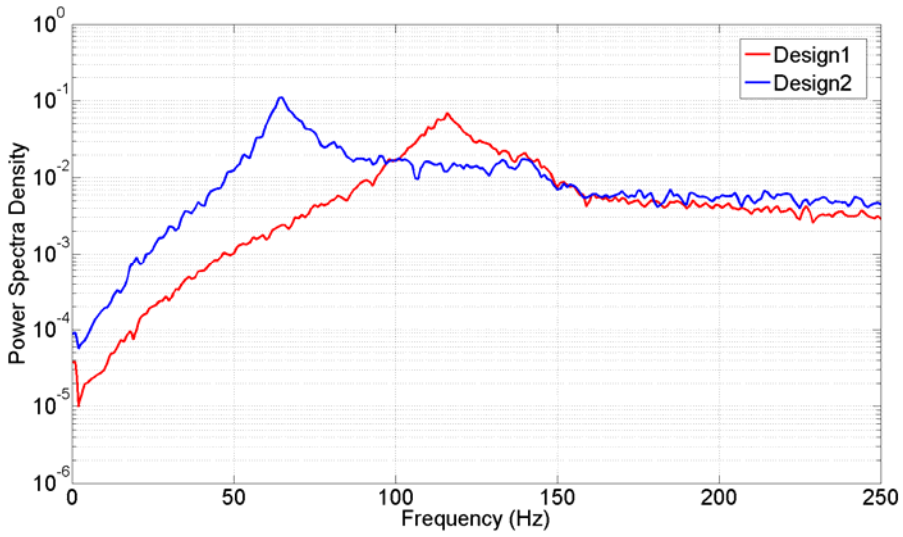

Figure 3.9 Power spectra density of two piezoelectric energy harvesters

In test 2, thirteen different resistances, 1, 3.3, 4.8, 6.7, 9.9, 11.8, 14.9, 19.4, 26.5, 50.5, 67.9, 98.6, and 118 kΩ, were used to measure the voltage generated by the piezoelectric beam. A harmonic sine wave was applied to the system at the resonant frequency determined from test 1, and the amplitude of base excitation was measured to be 0.21g (2.06 m/s2) and was held constant during the tests by monitoring the base acceleration from the accelerometer. The damping ratio of the two prototypes was measured to be 0.018. The power responses of the two piezoelectric energy harvesters at different load resistances are shown in Figure 3.10. From Figure 3.10a, the maximum power generated by design 1 and design 2 were measured to be 0.197 and 0.657mW, while the predicted results were 0.209 and 0.587mW, respectively, resulting in 6.09% and 10.65% error. The optimal resistances predicted by the model were 9.8 and 15.1kΩ for design 1 and design 2, respectively, while from the plot, the optimal resistance for design 1 is around 11.8kΩ, and 14.9kΩ for design 2 from the measured data. In both predicted and test results, with excitation at resonant frequency, the power generated from piezoelectric beam increases firstly, and then decreases after reaching the optimal resistance. The measured and predicted voltage data for the two designs are shown in Figure 10b. Generally, good agreements have been found between the predicted and measured data.

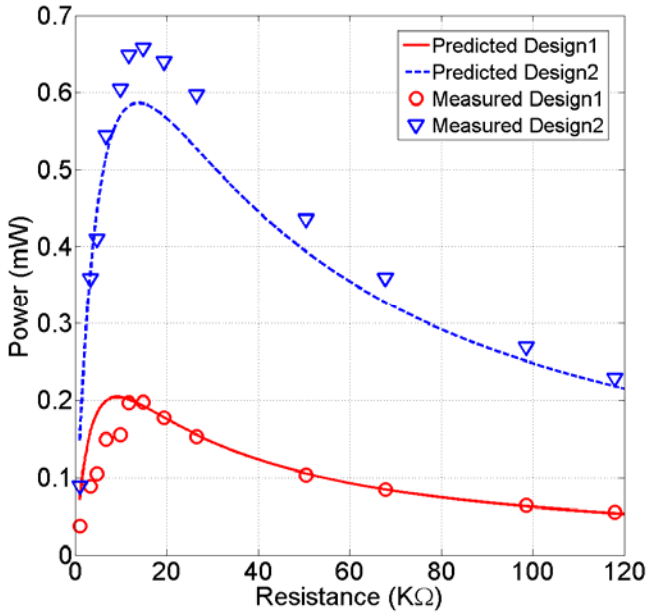

a) Power

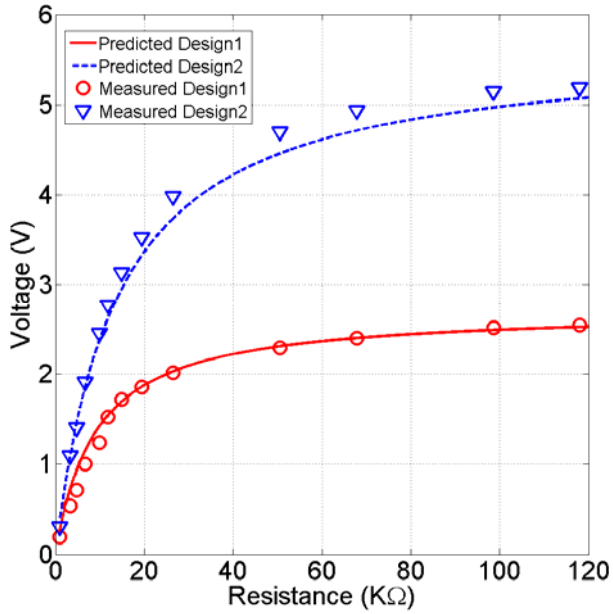

b) Voltage

Figure 3.10 a) Power, b) Voltage comparison of predicted and measured output versus resistance under 0.21g base excitation at resonance frequency

The relationship of maximum power, current, voltage and optimal load resistance between parallel and serial connection are given in Equation 3.24. For a given excitation frequency, if some amount of power is generated by a parallel system with a specific resistance, the same amount of power can be harvested by a serial system by using a resistance four times than that in the parallel system, while the parallel voltage is half the serial voltage and the parallel current is twice the serial current. The power envelope, optimal resistance, current and voltage as a function of frequency of these two designs when they are in parallel and serial connected from mathematical model can be found in Figure 3.11.

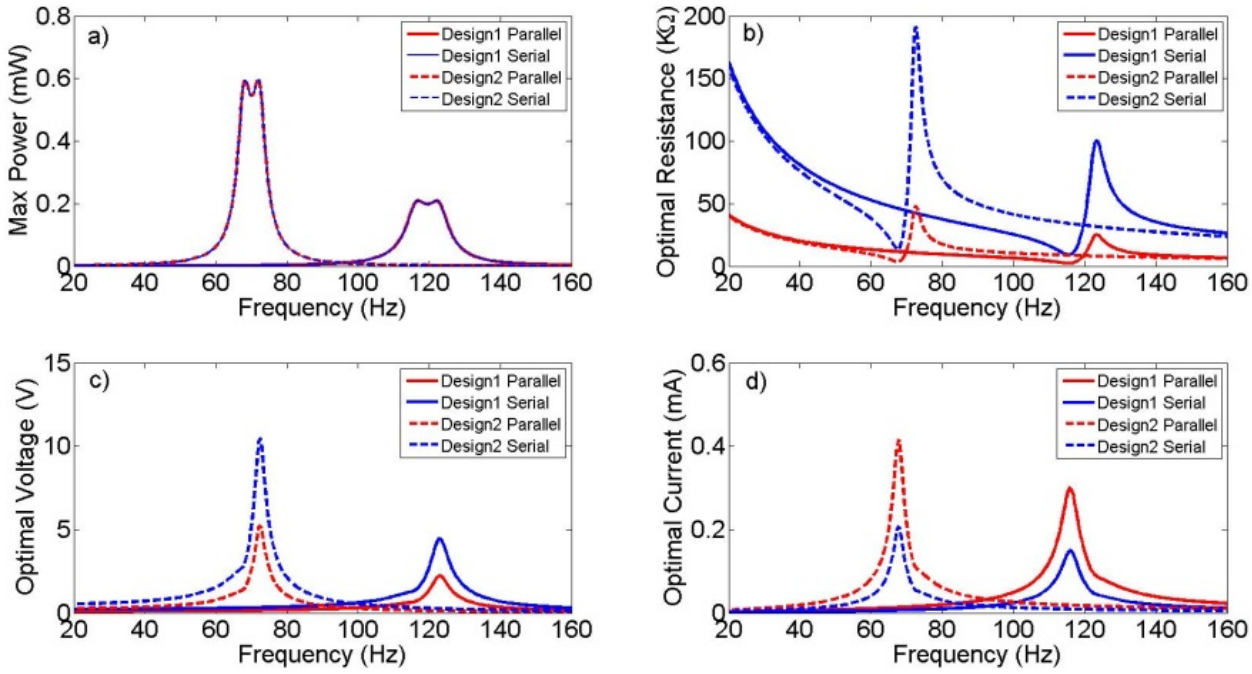

Figure 3.11 a) Power envelop, b) optimal resistance, c) optimal voltage, d) optimal current, of the parallel system and serial system

Figure 3.11a shows that the parallel and serial system have the identical power envelopes, which is a plot of output power versus excitation frequency with optimal resistance connected in the system. Two power peaks in the plot for each design represents the short-circuit resonance and open-circuit resonance, which are 116.5Hz, 122Hz for design1 and 68.2Hz, 71.8Hz for design2 from the simulation. In addition,

by adding the tip mass to the free end, not only decreases the resonant frequency of the system, but only increases the maximum power generation. Though the maximum power generated by the two systems are identical, the voltage (Figure 3.11c) and current (Figure 3.11d) are different due to different optimal resistances. For a particular excitation frequency, the optimal current in parallel system is twice of the optimal current in serial system, while the optimal voltage in parallel system is half of the optimal voltage in serial system. This is an important result for different applications. For example, if a device is intended for rechargeable battery purpose, a parallel system would be more suitable for that case because higher current can be generated. On the other hand, if high voltage is more desirable, then a parallel system would be preferred.

3.3.3 Design of a wide-band piezoelectric array

The mathematical model for predicting power generation of the piezoelectric energy harvester has been validated in section 3.3.2. Generally, good results have been obtained between the predicted and test results for both piezoelectric harvesters with and without tip mass. Adding tip mass can increase the power generation of a system, but most importantly, it can be used to tune the system's resonant frequency. However, one drawback of the single piece piezoelectric cantilever beam is that the power generation will decrease significantly outside the resonant frequency. This makes it unrealistic to be applied in real structure when no dominant vibration frequency is excited.

To this end, a wide-band vibration-based energy harvester needs to be designed for converting vibration energy from wide-band excitation frequency range. Compared to the single resonant piezoelectric harvester, wide-band harvester system will be much more robust at particular design frequency range. By connecting multiple pieces of piezoelectric cantilever beams with different resonant frequencies in series, the operating frequency band of the piezoelectric harvester can be widened and shifted to the excitation frequency from ambient environment for more effective energy harvesting. A schematic of the piezoelectric array is presented in Figure 3.12.

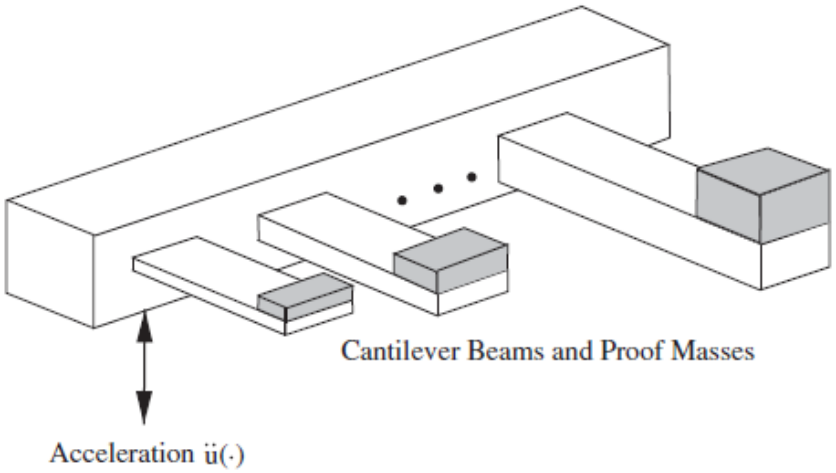

Figure 3.12 Schematic of multiple piezoelectric harvesters with proof mass

Since each bimorph piezoelectric harvester work individually from the same basic excitation, the model shown in previous section for predicting the power, current, and optimal resistor of each piezoelectric harvester is still appropriate. By connect all the pieces of harvesters in series, the total voltage and power of the system can be determined as:

$$V = \sum_{i=1}^{n} V_i \tag{3.25a}$$

$$P = V^2 / \sum_{i=1}^{n} R_i \tag{3.25b}$$

where i represents the number of piezoelectric harvester, n is the total number.

The bimorph piezoelectric energy harvesters with parallel connection in this study are from Steiner&Martin, Inc. The dimension of each piezoelectric beam is 40 × 10 × 0.5 mm (measured), with 0.1mm thickness for each piezoceramic, and 0.3mm for substructure brass. The Young's modulus for the brass and piezoelectric ceramics are 100GPa and 72GPa, respectively. The density of the brass and piezoceramic is 8400 kg/m^3 and 7800 kg/m^3, respectively. The other parameters are strain constant d31 = -270e^{-12} C/N, and dielectric constant ε33 = 3500 ε0, where ε0 = 8.85e^{-12} farads/m.

A single piezoelectric energy harvester labeled PZT0 was served as baseline, while a wide-band piezoelectric array was assembled from six different piezoelectric beams PZT1 to PZT6 with different resonant frequencies. A plot of the single piezoelectric harvester and the piezoelectric array can be found in Figure 3.13, and the geometry of each piezoelectric is shown in Table 3.3. In Table 3.3, M_b is the mass of piezoelectric beam, M_t is the mass of proof mass, and α is the ratio of M_t/M_b. By clamping different location of the piezoelectric beam, the length of each cantilever beam can be tuned.

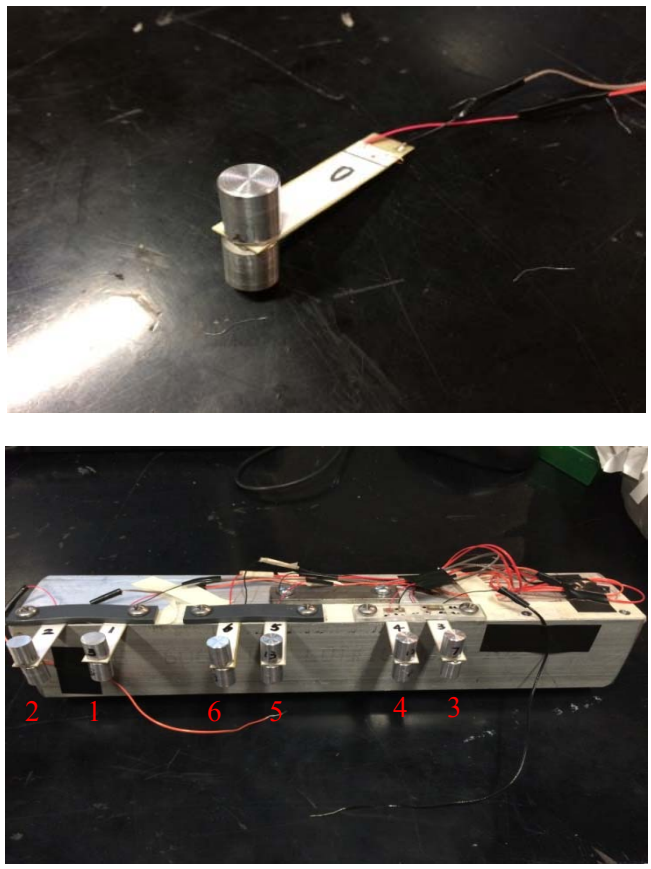

Figure 3.13 Piezoelectric beams: single beam (top), array (bottom)

Table 3.3 Geometry of each piezoelectric beam

PZT No.	t (mm)	w (mm)	l (mm)	M_b (g)	M_t (g)	α
0	0.5	10	33	1.35	3.81	2.82
1	0.5	10	30	1.23	3.48	2.83
2	0.5	10	31	1.27	3.59	2.83
3	0.5	10	32	1.31	3.72	2.84
4	0.5	10	33	1.35	3.82	2.83
5	0.5	10	34	1.39	3.96	2.85
6	0.5	10	35	1.43	4.08	2.85

Firstly, in order to find out the resonant frequency of each piezoelectric beam, they were tested at random excitation separately. Figure 3.14 shows the power spectral density of PZT0 and PZT1 to PZT6 from experimental test. The natural frequencies of PZT0 to PZT6 determined from the experimental test are 63.25, 76.63, 71.50, 66.25, 63.13, 58.88, and 55.38Hz, respectively, while 64.85, 78.73, 73.13, 68.51, 64.53, 60.59, and 57.18Hz from the mathematical model. Generally, good agreement has been found between the experimental test and mathematical model. The errors from mathematical model for determining the natural frequencies of PZT0 to PZT6 are 2.53%, 2.74%, 2.28%, 3.41%, 2.22%, 2.90%, and 3.25%, respectively, showing close agreement below 4%.

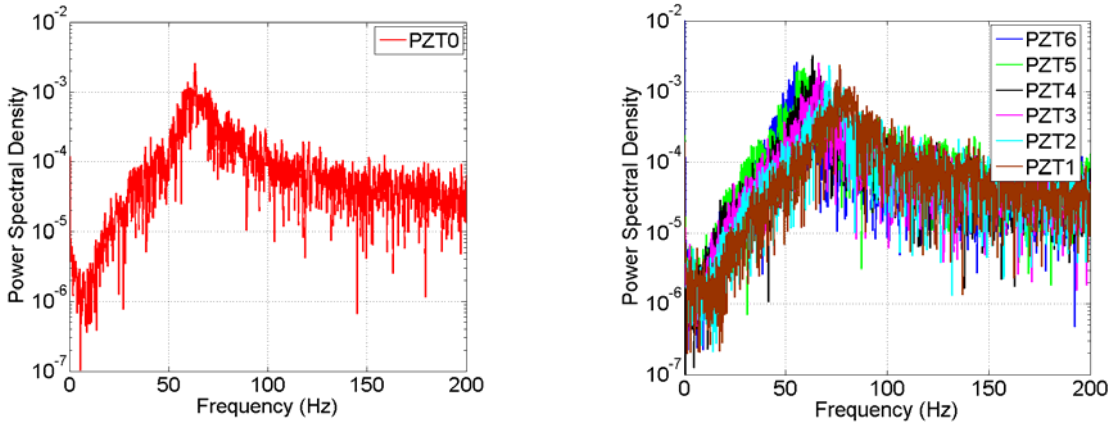

Figure 3.14 Power spectral density from experimental test for PZT0 (left) and PZT 1 to 6 (right)

Secondly, after the resonant frequency of each piezoelectric beam was determined, the piezoelectric beam was then excited at the resonant frequency with different resistors in order to found out the optimal

resistor and maximum power generation of each piezoelectric beam. The resistors used in this study were 1.0, 3.3, 6.7, 9.9, 14.9, 26.5, 67.9, and 118 KΩ. In the lab test, the excitation amplitude for each test was kept consistent as 0.2g. Figure 3.15 shows the voltage and power generation of each piezoelectric beam excited at the resonant frequency with different resistors connected in the system. The left two plots show the results from mathematical model, while the right two are from test results. From the figure, two observations can be found. Firstly, the optimal resistors for the piezoelectric beam PZT0 to PZT6 are determined to be 7.3, 6.6, 6.8, 7.1, 7.3, 7.5, and 7.8 KΩ from the mathematical model, respectively, while the maximum power of all the 7 piezoelectric beams are reached when the resistor is 9.9 KΩ from the experimental test. Secondly, the maximum power generated from piezoelectric beam PZT0 to PZT6 with the optimal resistor are 0.26, 0.20, 0.22, 0.24, 0.26, 0.29 and 0.32 mW from the mathematical model, and 0.31, 0.24, 0.26, 0.28, 0.31, 0.33, and 0.36 mW from the experimental test. Note that since the geometries of piezoelectric beam 4 and 0 are almost the same, they nearly have the same performance in terms of power generation. In general, good agreement has been found between the mathematical model and experimental test.

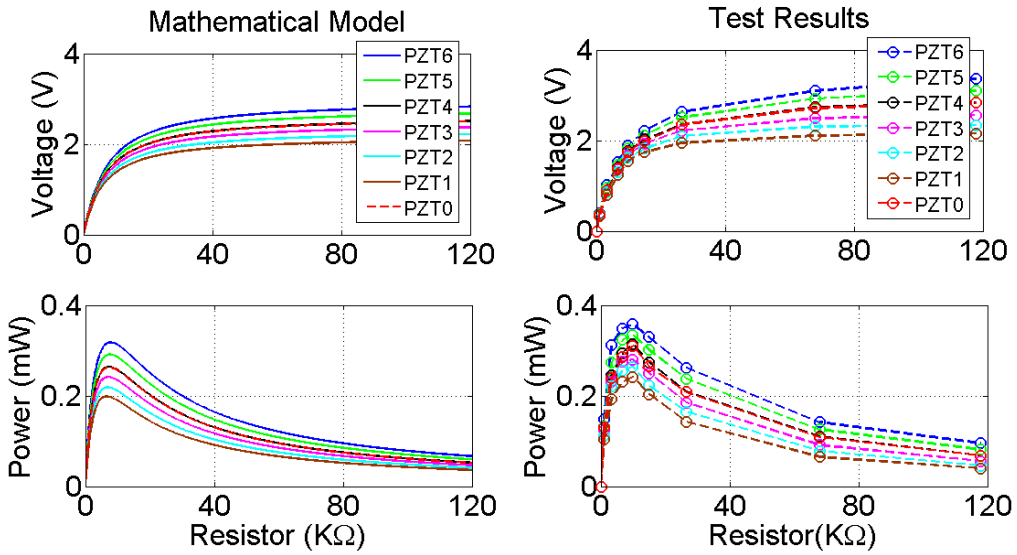

Figure 3.15 Power generation for each piezoelectric beam

Thirdly, with optimal resistor connected, each piezoelectric beam was tested at different frequencies from harmonic excitation to find out the relationship between power generation and excitation frequency. The excitation frequencies for each beam included the resonant frequency, several frequencies below resonant frequency and several frequencies over resonant frequency. Then the performance of the piezoelectric array with six piezoelectric beams (PZT1 to PZT6) connected in series was also tested under different frequencies with harmonic excitation. The excitation amplitude for all the tests was kept 0.2g consistently. The excitation frequencies for the piezoelectric array from low to high were 40, 45, 48, 53, 55.4, 57.2 58.9, 61, 63.1, 64.7, 66.3, 68.9, 71.5, 74.1, 76.6, 78.3, 80, 85, and 90Hz. They included the resonant frequency for each piezoelectric beam in the array, and several frequencies below the lowest resonant frequency, and several frequencies over the highest frequency.

The power generation of each piezoelectric beam and the piezoelectric array with optimal resistor under different excitation frequencies is shown in Figure 3.16. The left one shows the results from the mathematical model, and the right one shows the results from the experimental test. Several results can be found the figure. First, compare to single piezoelectric beam whose power generation decreases significantly out of resonance, the piezoelectric array shows wider operating frequency range in both mathematical model and test results. Second, similar trend in terms of power generation from different excitation frequencies can be presented between the mathematical model and test results. Third, the maximum power generation of the piezoelectric array is 0.27mW from the test results and 0.28mW from the mathematical model. Four, from the mathematical model, the average power generation between 57Hz and 78Hz is 0.22mW.

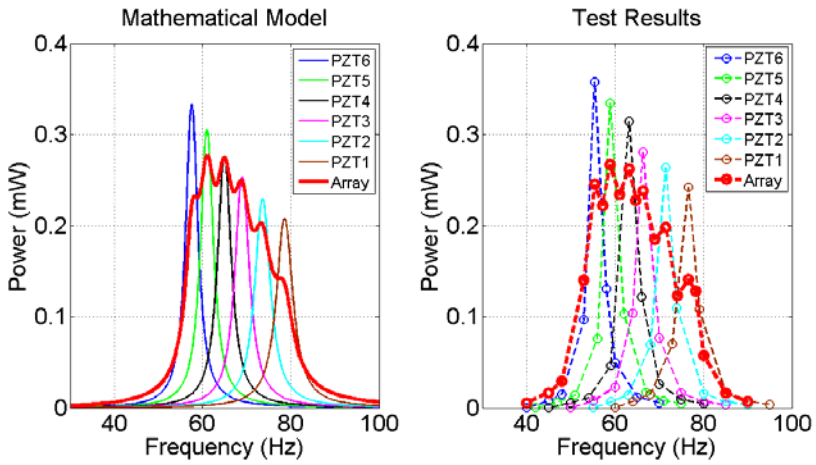

Figure 3.16 Power generation of the piezoelectric beam and array at different frequencies

From the test results and well matched from the mathematical model, a wide-band piezoelectric array with operating frequency range between 57Hz and 78Hz has been developed. The power generation of the piezoelectric array is much more robust than a single piezoelectric beam. However, the average power generation of the piezoelectric array in the operating frequency range (57Hz to 78Hz) is still small (0.22mW) to supply power to the Imote2 node. This is caused by the small size of each piezoelectric beam connected in the system. In order to supply enough power for the Imote2 sensor node, larger size of piezoelectric beams are desired.

If each of the piezoelectric beam PZT1 to PZT6 increases four times, and keep the mass ratio the same, which is shown in Table 3.4. The power generation of each piezoelectric beam and the piezoelectric array from different excitation frequencies predicted by the mathematical model can be found in Figure 3.17.

Table 3.4 Geometry of each new piezoelectric beam in the piezoelectric array

PZT No.	t (mm)	w (mm)	l (mm)	α
1	2.5	50	150	2.83
2	2.5	50	155	2.83
3	2.5	50	160	2.84
4	2.5	50	165	2.83
5	2.5	50	170	2.85
6	2.5	50	175	2.85

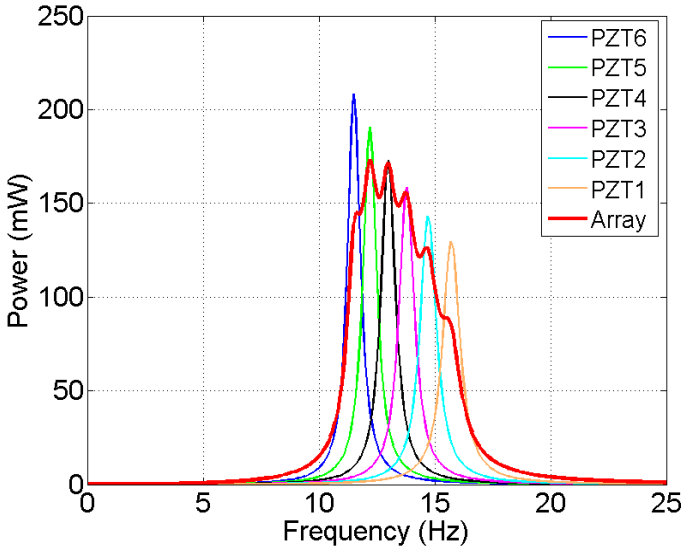

Figure 3.17 Power generation of new piezoelectric beams and piezoelectric array

From Figure 3.17, the resonant frequency of PZT1 to PZT6 is 15.6, 14.6, 13.7, 12.9, 12.1, and 11.4Hz, respectively, predicted by the mathematical model. The maximum power generated from the piezoelectric array is 173mW at excitation frequency 12.1Hz, while the average power of the piezoelectric array between 11Hz and 16Hz is 129mW. It is greater than the target power consumption 103mW by the Imote2 sensor node identified in section 3.2.2. Note that, since the large size of piezoelectric beams are costly, due to limited resources, the power generation of the new piezoelectric beam were not tested. However, since the mathematical model was well validated by the single piezoelectric beam and piezoelectric array in small size, the new piezoelectric array based on the design in Table 3.4 shows potential to supply enough power to Imote2 wireless sensor node with wide-band excitation.

From the experimental test and mathematical model, several conclusions for vibration-based piezoelectric energy harvesting can be drawn:

1) By adding tip mass at the free end of a single piezoelectric beam, the maximum power generation will increase, and the resonant frequency of the system will decrease. It can tune the resonant frequency of the system to match external excitation;
2) By assembling multiple pieces of piezoelectric beams with different resonant frequencies, operating frequency of the piezoelectric array could be widen;
3) By increasing the size of piezoelectric beam connected in an array, the maximum power generated from the array could be increased. In addition, by keeping other parameters the same, the longer the piezoelectric beam, the lower its natural frequency. It will also be helpful for tuning the resonant frequency of the piezoelectric energy harvester to external excitation frequency.

3.4 Summary

In this chapter, the wireless sensor platform Imote2 and SHM-A sensor board were first introduced. Different applications based on the ISHMP Services Toolsuite for the Imote2 sensor node was were then discussed. In the second part, power consumption of the Imote2 sensor node was evaluated. There were five power states in Imote2 node, power consumption of each power state was identified from an experimental test. Based on the results, power consumption of the Imote2 with different *RemoteSensing* events per day was calculated. With one *RemoteSensing* event per day, the average power consumption of the Imote2 node was around 103mW and this value was served as a target for power energy harvesting devices. In the third part, a wide-band piezoelectric energy harvester was designed to supply enough power for Imote2 node. A mathematical model for predicting single piezoelectric beam was validated through an experimental test. The test results showed good agreement with the mathematical model in terms of natural frequency, optimal resistor, and maximum power generation. Second, since the power generation of a single piezoelectric beam decreased significantly out of resonance, a wide-band piezoelectric array with six piezoelectric beams with different resonant frequencies in serial connection was developed. Average power of 0.22mW was generated in the frequency range between 57Hz and

78Hz from the piezoelectric array. Results from the mathematical model also matched very well with the test results. Finally, based on the mathematical model, a piezoelectric array with larger size of piezoelectric beams was designed. An average power of 129mW could be generated from the frequency range 11Hz to 16Hz by the piezoelectric array. That was greater than the target value for Imote2 sensor node. Thus a potential solution for supplying enough power for Imote2 sensor node from a vibration-based wide-band piezoelectric energy harvester has been developed in this dissertation.

CHAPTER 4 FULL-SCALE BRIDGE HEALTH MONITORING

4.1 Introduction

An example of a full-scale bridge health monitoring system is presented in this chapter. A single-span in-service highway bridge located in Meriden, Connecticut is used as a test bed. Firstly, the location and geometry of the highway bridge are discussed. Secondly, an algorithm-of frequency domain decomposition for output-only system to identify structural vibrations is introduced.. Lastly, system identification of modal properties of the highway bridge is performed based on monitoring data from a WSSN and a long-term wired monitoring system installed on the highway bridge. This includes the equipment setup and data acquisition procedure. . In addition, a finite element (FE) model of the highway bridge is also developed using SAP2000 software. The Chapter is concluded with comparison of the results from the WSSN, the wired monitoring system, and the FE model.

4.2 The Meriden Bridge

The in-service Meriden Bridge was used as test bed in this study. It was built in 1964 and located on I-91 Northbound in Meriden, Connecticut. The bridge is a simple-support single-span eight-girder steel composite bridge with 85 feet long and 55 feet wide. It has less than a 12% skew and 3% longitudinal slope. According to the Connecticut Department of Transpiration (ConnDOT), the bridge carries three lanes with an annual average daily traffic of 57,000 vehicles with 9% trucks. The location of the Meriden Bridge can be found in Figure 4.1 and 4.2. Figure 4.3 shows a photograph of the Meriden Bridge.

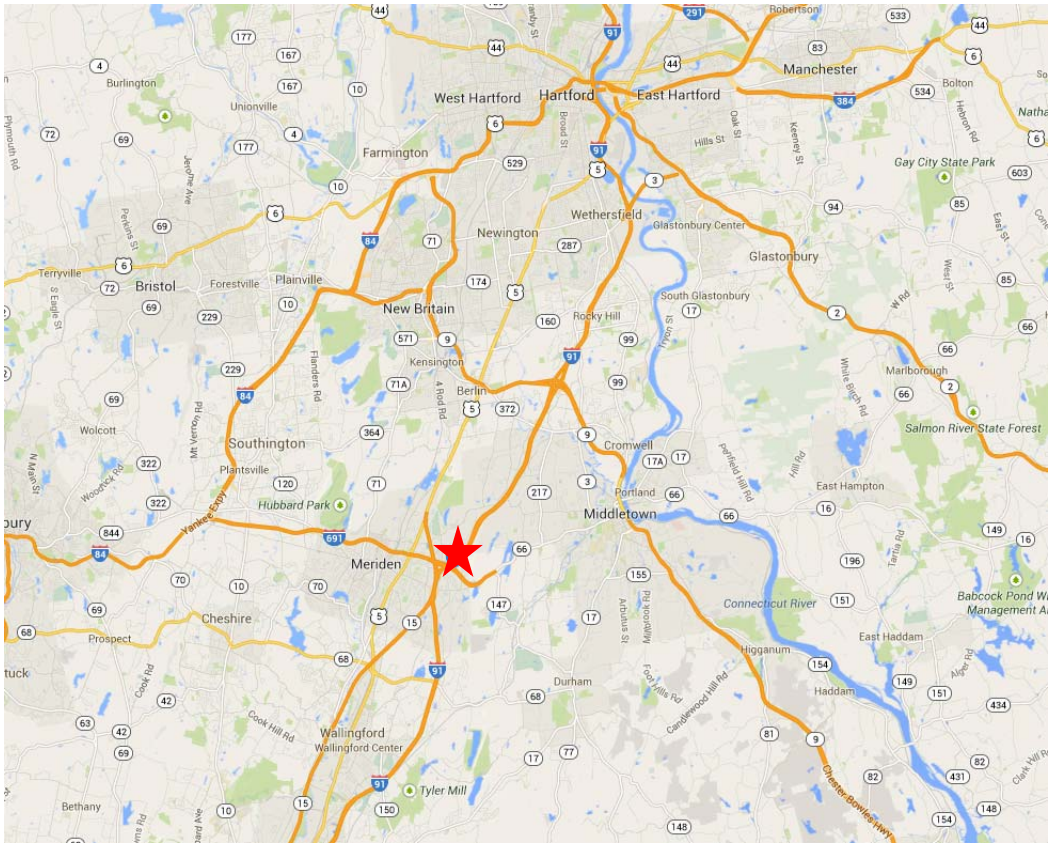

Figure 4.1 Location of the Meriden Bridge from Google map

Figure 4.2 Earth view of the Northbound Meriden Bridge from Google map

Figure 4.3 Side view of the Meriden Bridge

4.3 Output-Only System Identification using Frequency Domain Decomposition Technology

System identification of ambient vibration structures using output-only system identification technology is critical in SHM of civil infrastructure, because in most of the time, input excitation to the structures is not easy to measure, only output response data can be measured by the monitoring system. System identification usually consists of determining structure natural frequencies, modal damping ratios, and mode shape.

So far, a number of mathematical models on the output-only system identification technology have been developed and can be classified into two characters: parametric methods in time domain and nonparametric methods in frequency domain. Each identification technology in either the time domain methods or frequency domain methods has its own advantages and limitations. In general, parametric methods such as Polyreference technology (Vold et al. 1982), Ibrahim time domain technology (Ibrahim and Milkulcik 1976), Eigensystem realization algorithm (ERA) (Juang and Pappa 1985), or random decrement technique (RDT) (Ibrahim 1997) are preferable for identifying modal damping but difficulty in

natural frequencies and mode shapes. Stochastic subspace identification algorithm (Van et al. 1996) is often used by some researchers, but it is time consuming, especially when the monitoring data set is large and system order parameter is high. On the other hand, classical frequency domain method such as basic frequency domain technique, or pick peaking method is based on simple signal processing using the discrete Fourier Transform, which make it difficult to detect the close modes, and even when close modes are identified, estimates becomes heavily biased. However, the classical method can reasonably identify the natural frequencies and mode shapes if the modes are well separated. In addition, compares to the time domain methods, it is faster and easy to implement, and most importantly, by looking at the spectral density functions, it provides valuable basis of the structures to the users.

The frequency domain decomposition (FDD) technology was introduced first by Brincker et al. (2001). It overcomes the disadvantages of the classical frequency domain methods in terms of accuracy, but keeps the important features such as user-friendliness and easy to implement. It has been widely used for modal identification of output-only systems due to its reliability, straightforward and effectiveness. Therefore, this algorithm is employed throughout this research for bridge system identification.

4.4 Implementation of Wireless Smart Sensors on Full-Scale Bridge Monitoring

4.4.1 Equipment setup

A wireless monitoring system with six Imote2 wireless sensors were deployed on the Meriden bridges. The wireless system included five Imote2 wireless leaf nodes for acceleration measurement, and an Imote2 gateway node for collecting monitoring data from the leaf nodes. All the sensors were prepared in the lab before the deployment. Each of the Imote2 node was place inside a plastic box and attached to the base of the plastic box with epoxy adhesive. Three D-cell battery were also included in the box for supplying power to the nodes. Two magnets were attached to the bottom of each box for mounting the box to the web of girder in the bridge. A figure of the Imote2 nodes is presented in Figure 4.4.

Figure 4.4 Preparation of Imote2 nodes in the lab

All Imote2 nodes were tested for the performance in the field before actual deployment on the bridge. The Imote2 leaf nodes were mounted on the middle girder of the bridge (along x axis) with magnets on the bottom of the box to monitor the bridge ambient vibration due to traffic. The direction from girder 1 to girder 8 is y axis, and the vertical vibration direction of the bridge is z axis. The gateway node was installed near the base station in one abutment with a powerful antenna facing the leaf nodes. It was manufactured by Hawking Technologies. Figure 4.5 shows the overall layout of the wireless sensors. Figure 4.6 shows the actual installation location for the leaf node. Installation of gateway node and powerful antenna can be found in Figure 4.7.

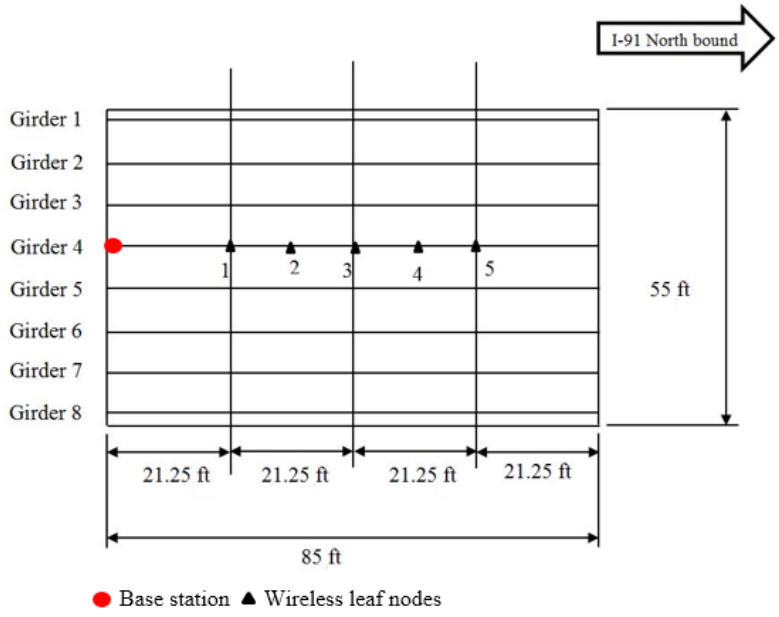

Figure 4.5 Layout of the Imote2 nodes on the Meriden Bridge (Dahal 2013)

Figure 4.6 Actual deployment of the Imote2 leaf nodes on the Meriden Bridge (Dahal 2013)

Figure 4.7 Actual deployment of the gateway node and antenna (Dahal 2013)

4.4.2 System identification

A laptop was connected to the base station and the data was collected with *RemoteSensing* application in the ISHMP Toolsuite discussed in Chapter 3. All the leaf nodes measured 3-axis acceleration (x, y, and z) and sent data back to base station. In each test, 20,000 data points with 280Hz sampling rate was used for measuring the bridge vibration. Several tests were repeated with the same sampling points and frequency. All the field test was performed on October 24th, 2011.

In order to convert the outputs from the Imote2 wireless nodes into measured units of acceleration, the data has to be detrend and divided by a sensitivity factor (the calibration constants in the unit of LBS/g). The normal offset and sensitivity factors are quoted in the ISHMP documentation, but these values vary from one sensor to another (ISHMP 2009). The vibration data collected by the five leaf nodes on one of the girder were analyzed to get modal properties such natural frequencies, damping ratio and mode shapes of the Meriden Bridge. A sample time history of the vertical vibration data under ambient traffic is presented in Figure 4.8.

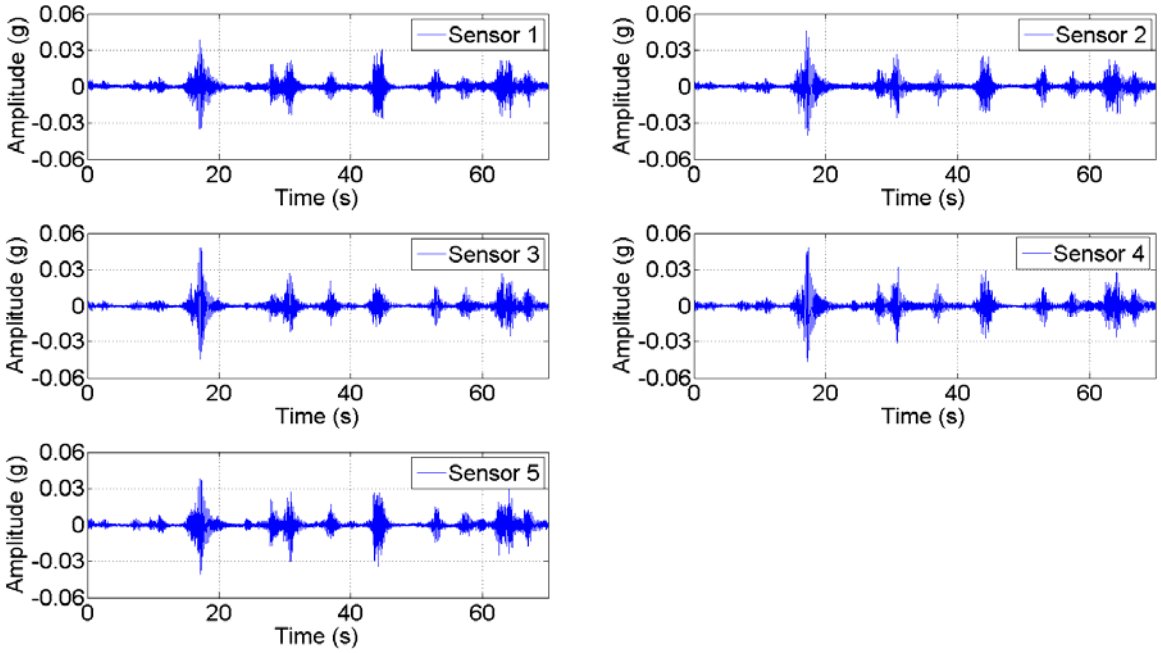

Figure 4.8 Time history of the bridge vertical vibration from field test data

From Figure 4.8, the maximum vertical acceleration recorded by the Imote2 nodes is about 0.048g from sensor 3. Each peak in the plot would be mostly caused by passing cars or trucks. FDD technology is employed to determine the modal properties of the Meriden Bridge, where sampling frequency is 280Hz, Nfft is 4480. Figure 4.9, 4.10 shows power spectral density (PSD) plot for each wireless sensor. The singular value plot is presented in Figure 4.11.

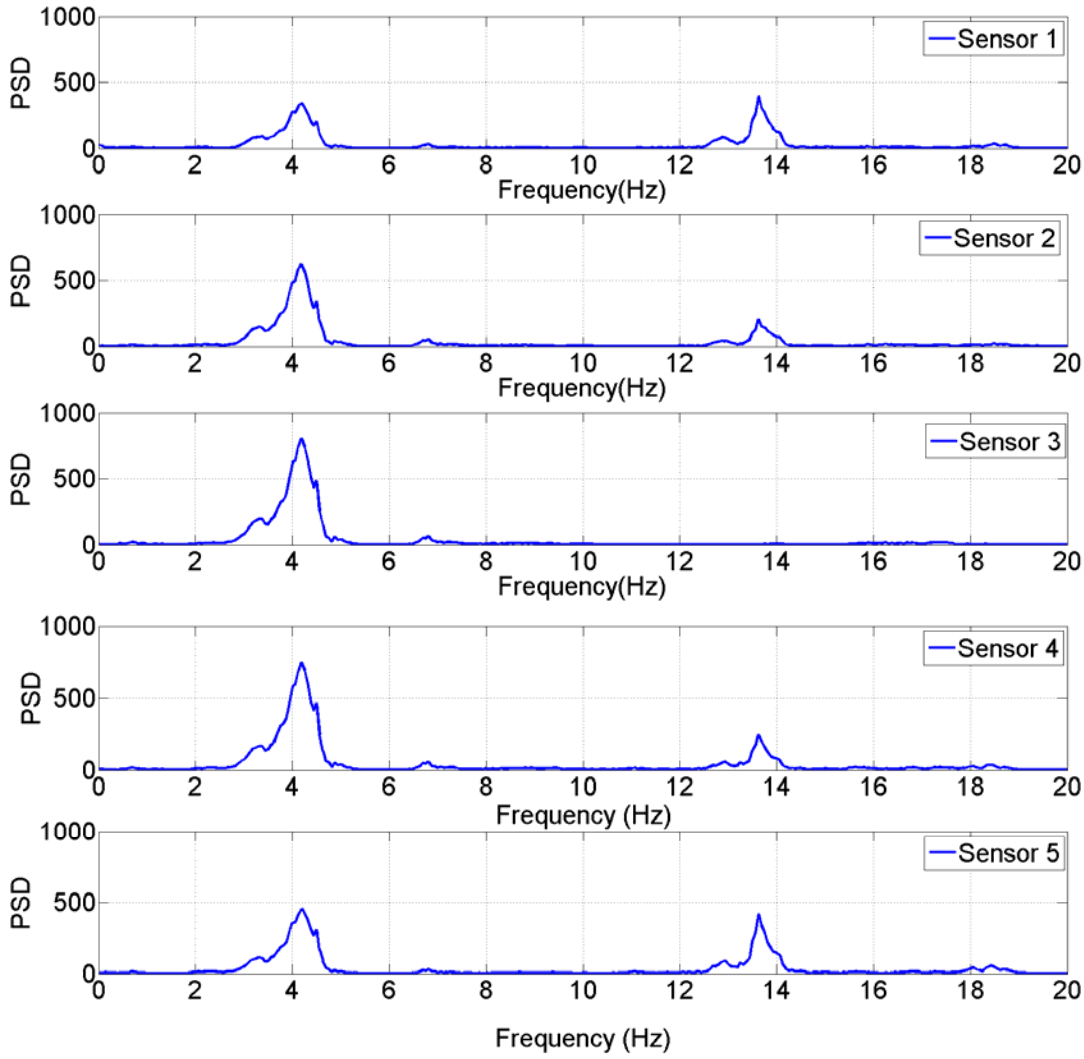

Figure 4.9 PSD plot for each sensor from field test data

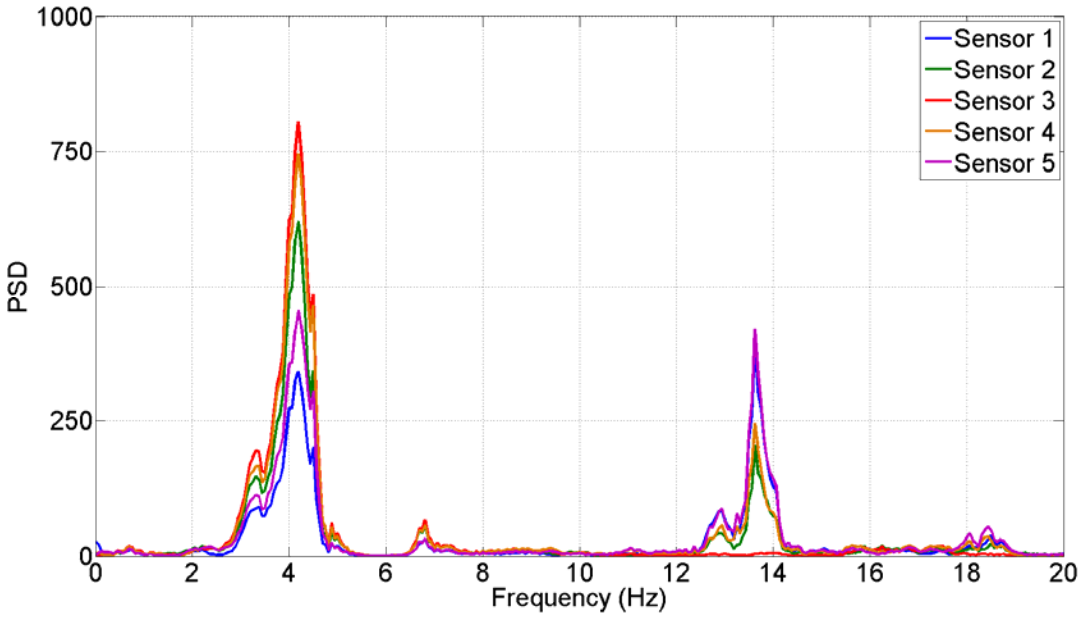

Figure 4.10 PSD plot for all the sensors from field test data

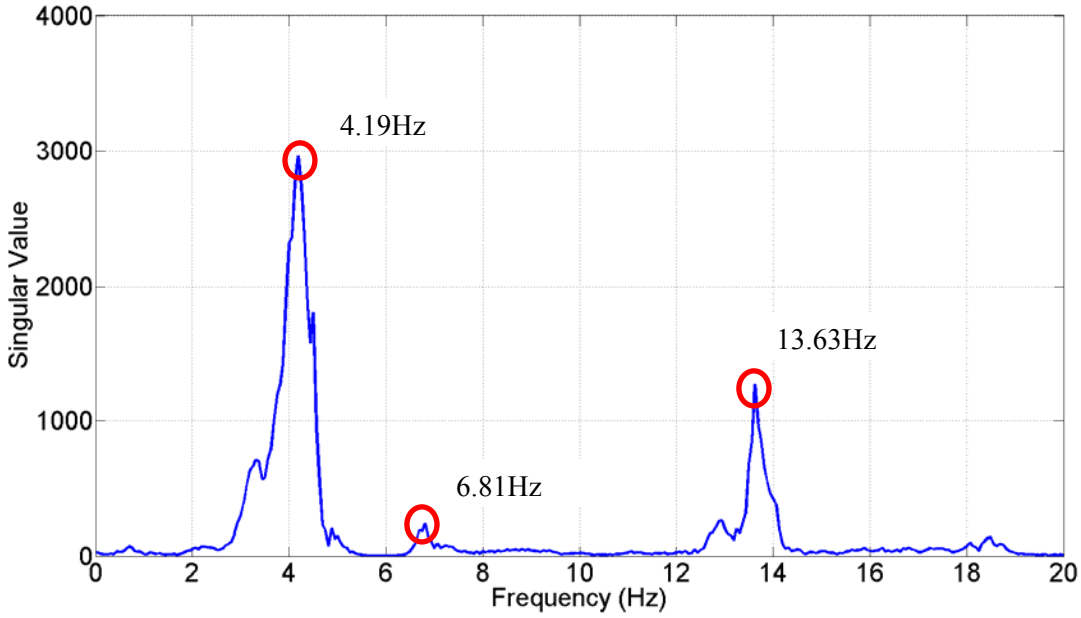

Figure 4.11 Singular value plot from the wireless sensors from field test data

From Figure 4.11, the first three natural frequencies has been identified to be 4.19Hz, 6.81Hz, and 13.63Hz. Since all the five wireless sensor nodes were deployed on the middle girder of the bridge, by analyzing the amplitude and phase angle at these three peaks, the mode 1 (4.19Hz) and mode 3 (13.63 Hz) represents the first and second bending mode of the Meriden Bridge (bending around x axis), respectively, while mode 2 (6.81Hz) is the first plate bending of the bridge (bending around y axis). The normalized bending modes can be found in Figure 4.12. Meanwhile, the effective damping ratio of the bridge can be determined by the half band method, which are 4.47%, 1.92%, and 1.15% for the first three modes, respectively.

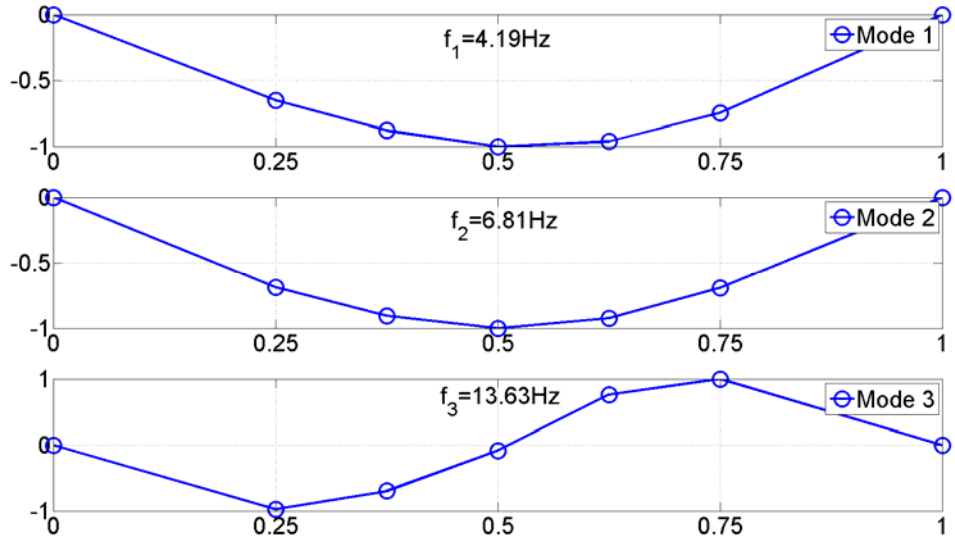

Figure 4.12 First three modes of the Meriden Bridge

4.5 Implementation of Wired Monitoring System on Full-Scale Bridge Monitoring

4.5.1 Sensor layout and data acquisition system

A wired long-term SHM system with a total number of 38 sensors was installed on the Meriden Bridge for both bridge health monitoring (BHM) and bridge weight in motion (BWIM) purposes. The sensors include 18 foil strain gages, 4 piezoelectric strain sensors, 8 piezoelectric accelerometers, 4 capacitance

accelerometers (with additional temperature sensing capability), and 4 resistance temperature detectors. A detail of the gage plan on the Meriden Bridge is presented in Figure 4.13.

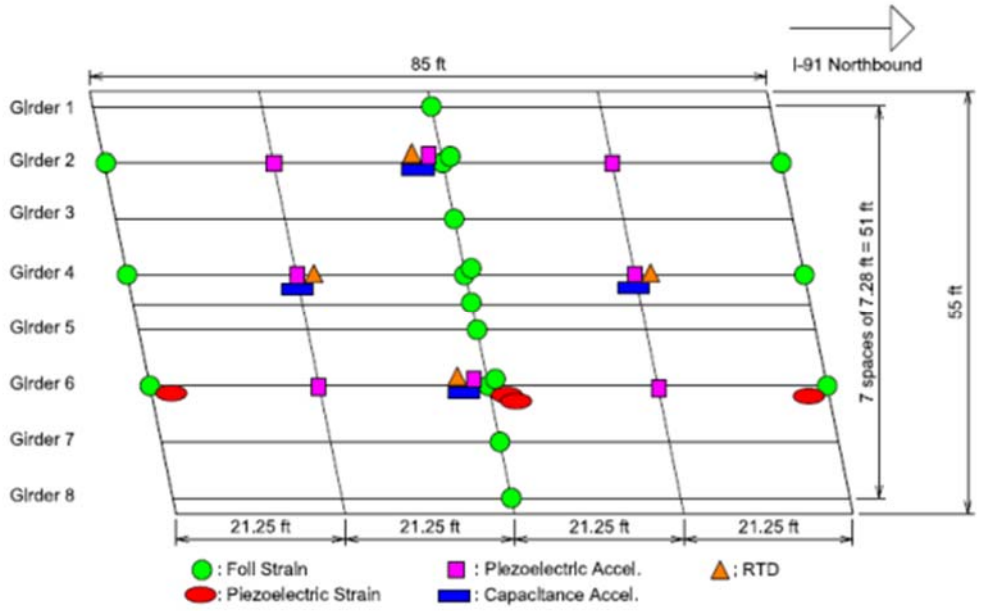

Figure 4.13 Sensor types and sensor layout for the Meriden Bridge

The eight piezoelectric accelerometers are manufactured from PCB piezoelectric, Inc. with part number 393B31. The accelerometers have a 0.5 g peak acceleration level and a frequency range from 0.1 to 200 Hz. According to specifications, the sensitivity is nominally 10.0 V/g and the resonant frequency is a minimum of 700Hz. Six PCB accelerometers are located at the quarter spans, under girders 2, 4, and 6. Two extra piezoelectric accelerometers are also installed at mid-span of girders 2 and 6, respectively. The layout of the piezoelectric accelerometers is presented in Figure 4.13 as pink squares. One thing needs to notice that, one PCB accelerometer at the right top on gird 2 failed due to the cable connecting this accelerometer to the data acquisition system was not appropriate installed, only seven acceleration data are used in this research.

The four RTDs are from Pyromation, Inc. with a part number of Z-006-18-13-T3(600 or 1200)-2(Z459). They are installed on two quarter spans of girder 4 and mid-span of girder 2 and 6. This diamond configuration shows if there are temperature changes in the west-east and north-south direction

along the bridge. A plot of the RTD is presented in Figure 4.16. Lay out of RTDs on the Meriden Bridge can be found in Figure 4.13 as orange triangles.

The data acquisition hardware is a National Instruments (NI) NI cDAQ-9178 CompactDAQ chassis with four different types of modules for different types of sensors. The chassis is connected to a Dell Ultra Small Factor-Optiplex 780 desktop using a USD 2.0 High-Speed cable. MATLAB with an add-on data acquisition toolbox is installed on the desktop which enables data collection from all the sensors and data analysis. All the data acquisition system components are housed in a converted traffic signal cabinet which is installed on the southern abutment underneath the bridge. It is shown in Figure 4.14.

Figure 4.14 Cabinet housing system component underneath the Meriden Bridge

Two types of data are collected from the monitoring system. The first type of data includes some piezoelectric strain gages and piezoelectric accelerometers at critical locations for BWIM purpose which is not considered in this research. They are collected every five minutes, and about ten sets of data each hour. The second type of data includes all sensors data in the system, they are collected at the last five minutes every hour after the first type of data. A total of eleven sets of data (ten sets for the first type, and

one set for the second) can be collected each hour (between two sets of data, the system needs to stop and restart for couple of seconds). Each data is five minutes long. All the data are collected at sampling rate of 2048Hz.

4.5.2 System identification

The FDD algorithm is employed in this section for identifying the modal properties of the Meriden Bridge in terms natural frequencies, mode shapes, and damping ratio. A data set with 30 minutes long between 6 PM and 7 PM on Sep 12th, 2013 is used. The time history data for each piezoelectric accelerometer at its location can be found in Figure 4.15.

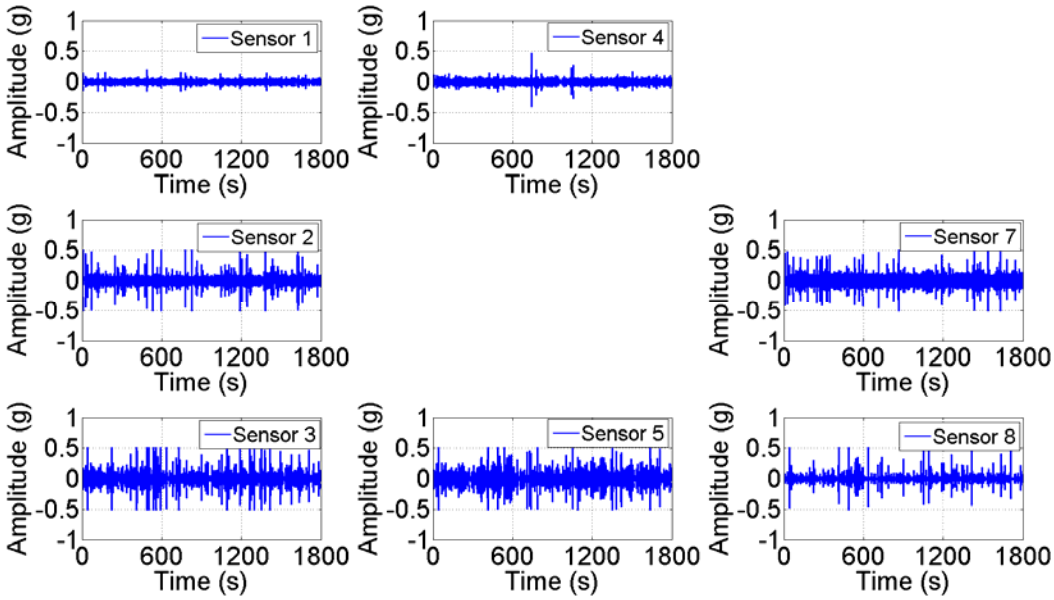

Figure 4.15 Time history of each piezoelectric accelerometer at its location

The maximum acceleration around 0.5g is found from the time history plot which is higher than that from wireless monitoring system shown in previous section. It could be explained by the fact that longer period data was collected by the piezoelectric accelerometers. In addition, during the monitoring period of wireless monitoring system, there were not heavy truck passing the bridge. Sampling rate 2048Hz, and Nfft 65536 were used in FDD algorithm for system identification. The PSD of each piezoelectric

accelerometer at its location is presented in Figure 4.16. A combine plot of all the PSD from accelerometers is shown in Figure 4.17. Figure 4.18 presents the singular value plot.

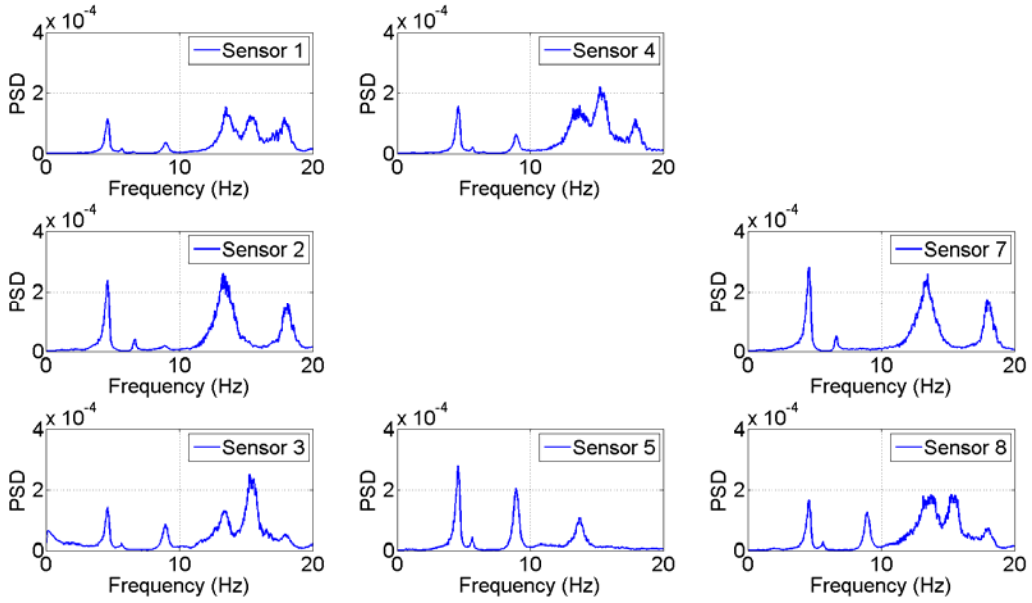

Figure 4.16 PSD of each piezoelectric accelerometer at its location

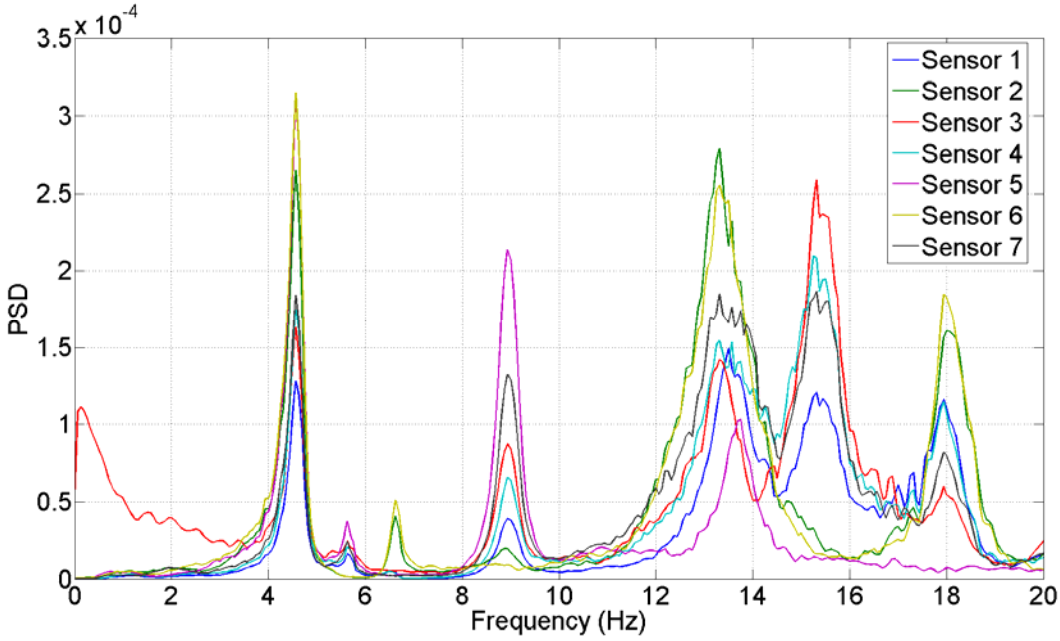

Figure 4.17 PSD for all the piezoelectric sensors

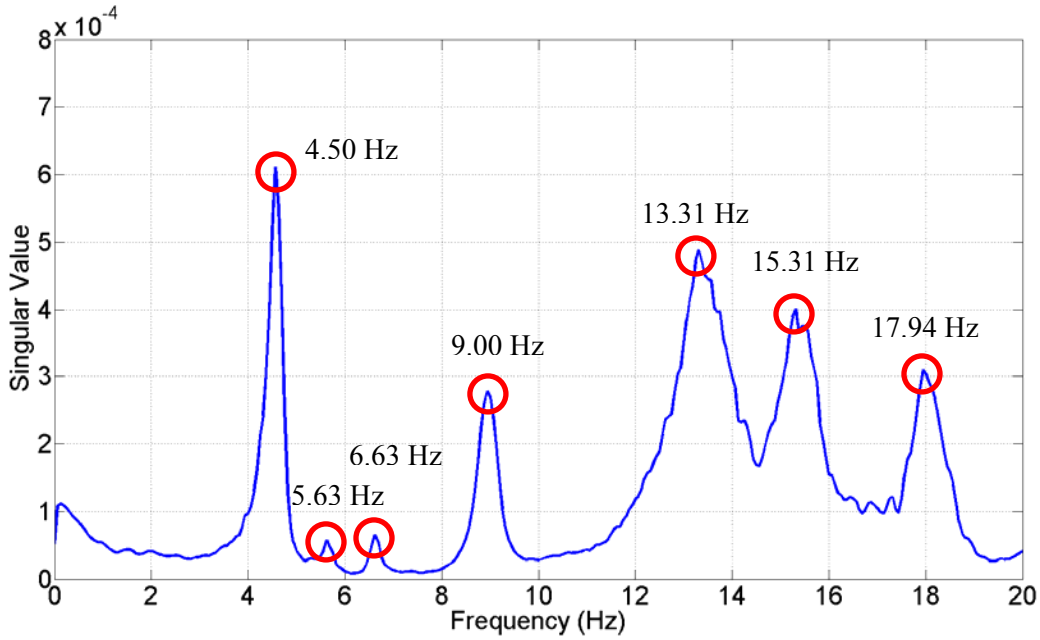

Figure 4.18 Singular value plot from all the piezoelectric accelerometers

This first seven eigenvalues from the singular value plot can be determined to be 4.50, 5.63, 6.63, 9.00, 13.31, 15.31, and 17.94Hz, which present the first seven natural frequencies of the Meriden Bridge. By applying the half-power bandwidth method, the damping ratio for the first seven modes are 2.74%, 2.22%, 1.89%, 1.75%, 3.05%, 2.45%, and 1.57%, respectively. The mode shapes can be found in Figure 4.19.

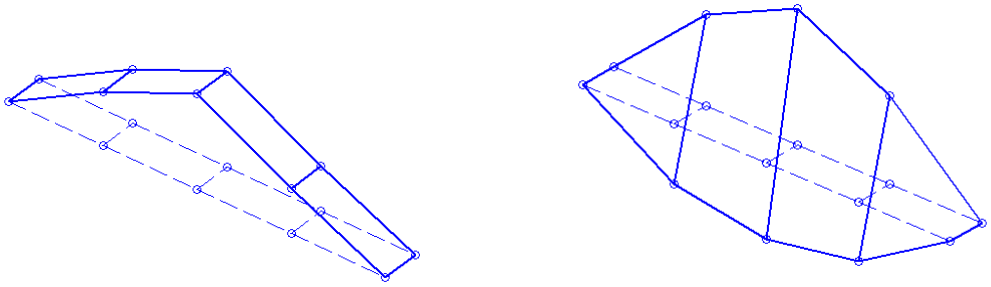

a) 1st bending = 4.50 Hz

b) 1st torsion = 5.63 Hz

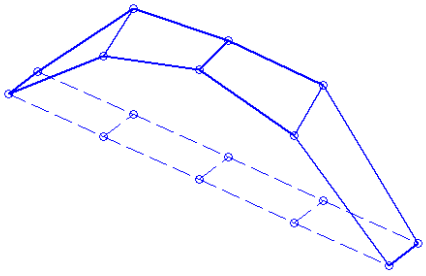

c) 1st plate bending = 6.63 Hz

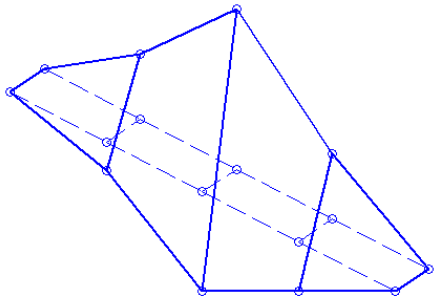

d) local mode= 9.00Hz

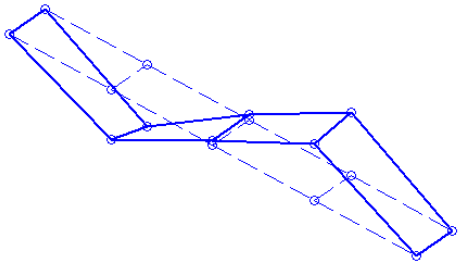

e) 2nd bending= 13.31 Hz

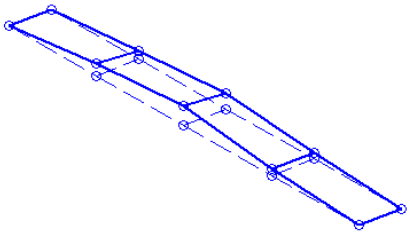

f) 2nd plate bending = 15.31 Hz

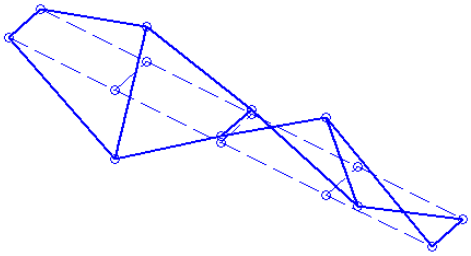

g) 2nd torsion= 17.94 Hz

Figure 4.19 Mode shapes of the Meriden from field monitoring data

4.6 Finite Element Model of the Meriden Bridge in SAP2000

A 3-D finite element (FE) model of the Meriden Bridge is developed in SAP2000 software for modal analysis in this section. A detail drawing of the Meriden Bridge from Connecticut State Highway

Department is presented in Figure 4.20. The drawing shows the dimension of the bridge, material and geometry of the steel girder and lateral bracing, and boundary condition. Based on the information from the drawings, a 3-D FE model of the Meriden Bridge can be found in Figure 4.21.

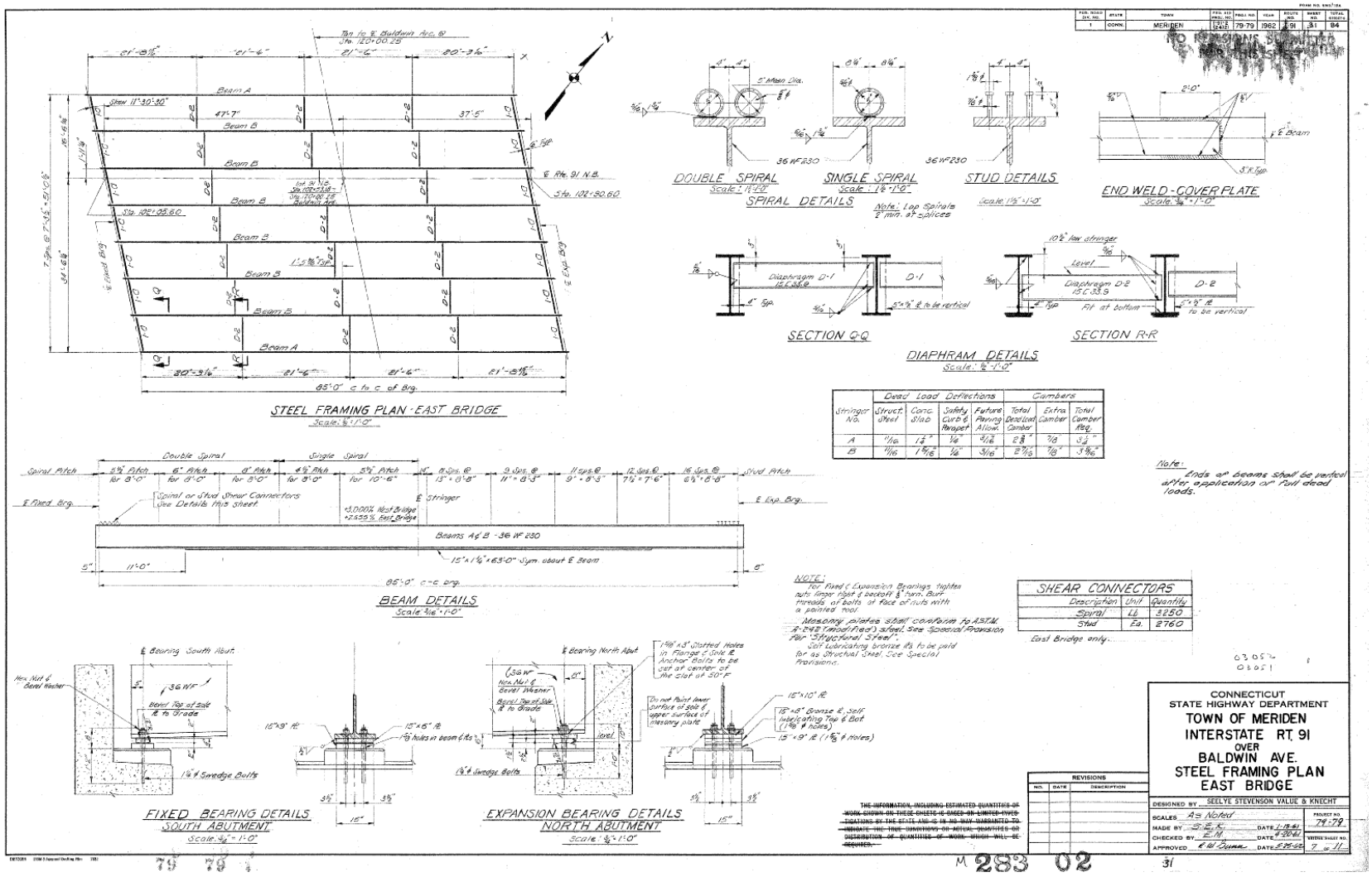

Figure 4.20 A drawing of the Meriden Bridge from Connecticut State Highway Department

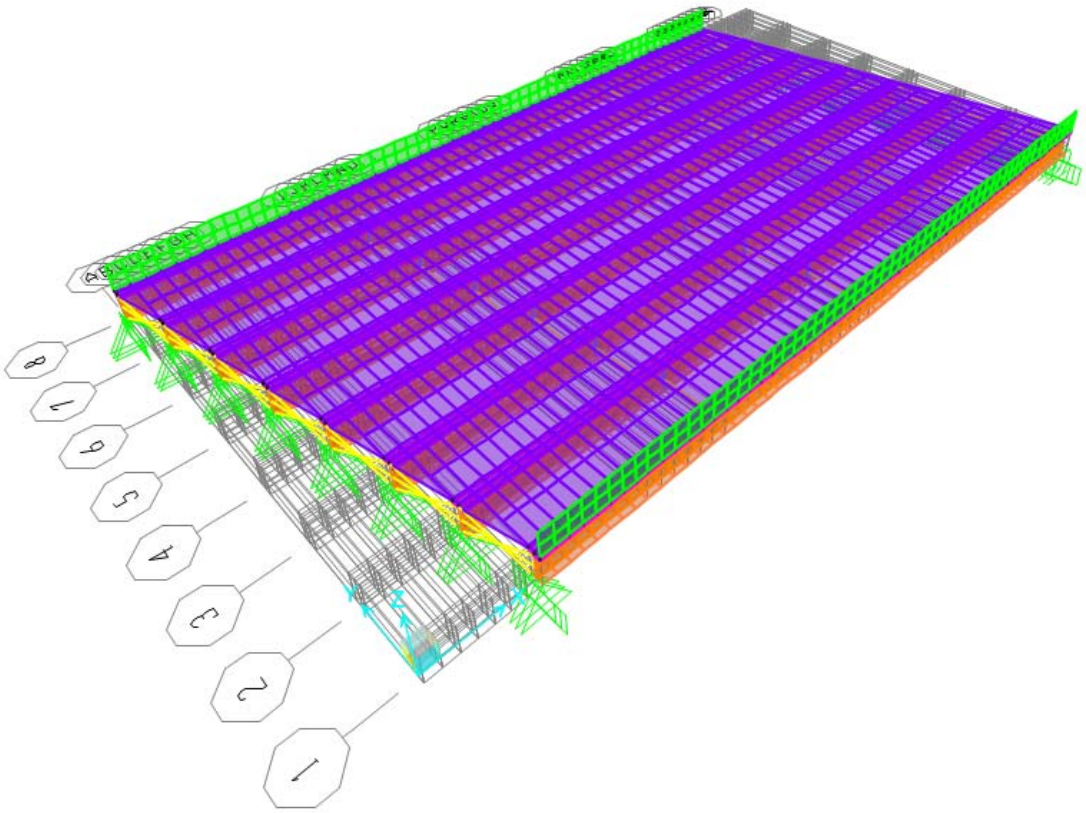

Figure 4.21 The 3-D FEM of the Meriden Bridge in SAP2000

From the drawing, the steel girder is a wide flange beam W36 X 230, and the lateral bracing is a C-shape beam C15 X 33.9 on the bridge. The cross section of the wide flange beam and C-shape lateral bracing is presented in Figure 4.22 a) and 4.22 b).

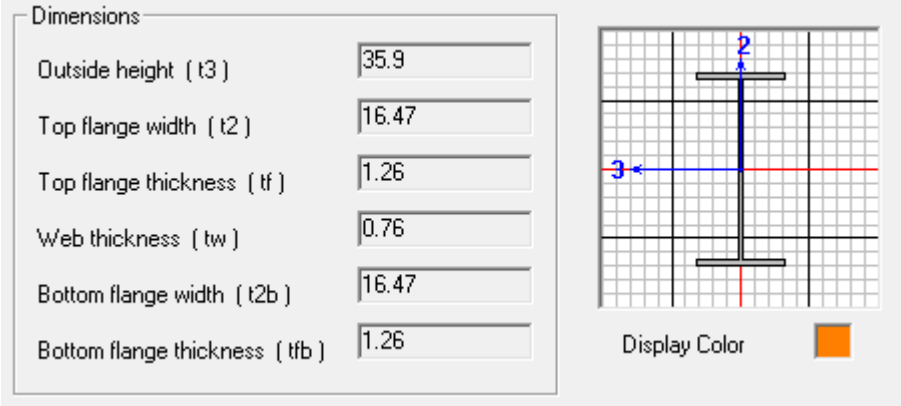

a) Cross section of the W36 X 230 wide flange beam

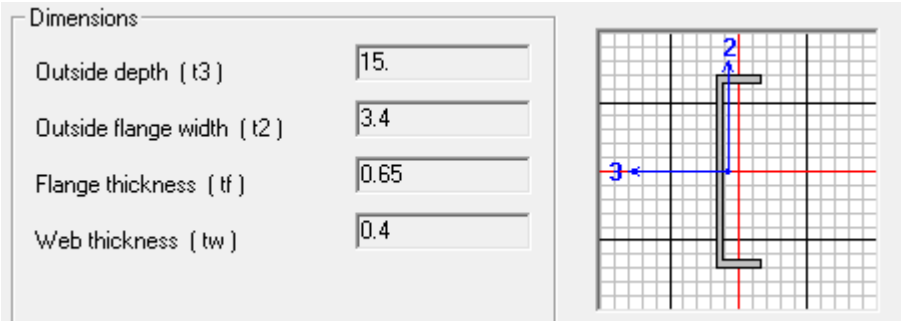

b) Cross section of the C15 X 33.9 lateral bracing

Figure 4.22 Cross section of the beams in Meriden Bridge

In the FE model, the web and flange of the steel girder was modeled as thin shell element with thickness equaled to that in the flange cross section. One thing needs to notice that a steel plate was attached to the bottom flange of each steel girder, an equivalent thickness of the bottom flange and steel plate was calculated and modeled as shell element in the FE model. The concrete slab and safety curb were also modeled as shell element with thickness the same as that shown in the drawing. Dummy rigid links were introduced between the concrete slab and top flange in the FE model as shear connect. The shear connector between the concrete slab and top flange can be found in the cross section drawing of the Meriden Bridge shown in Figure 4.23. The rigid links in the FE model is presented in Figure 4.24.

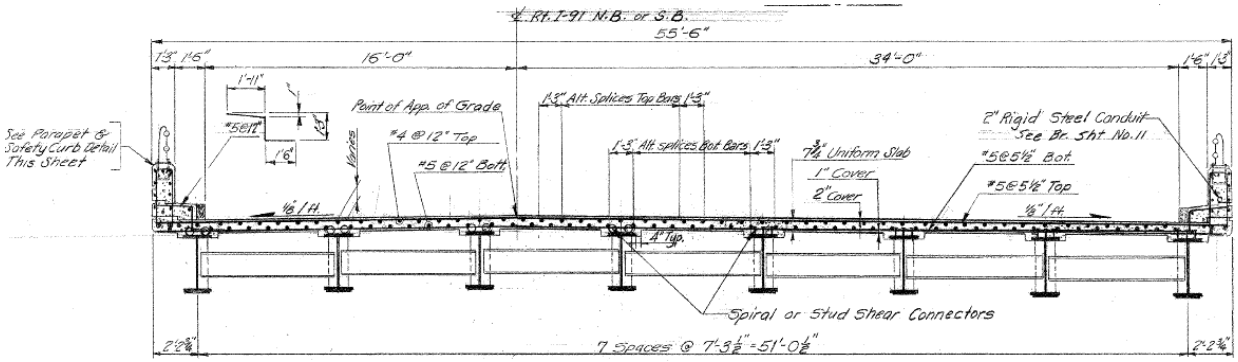

Figure 4.23 Cross section of the Meriden Bridge in the drawing

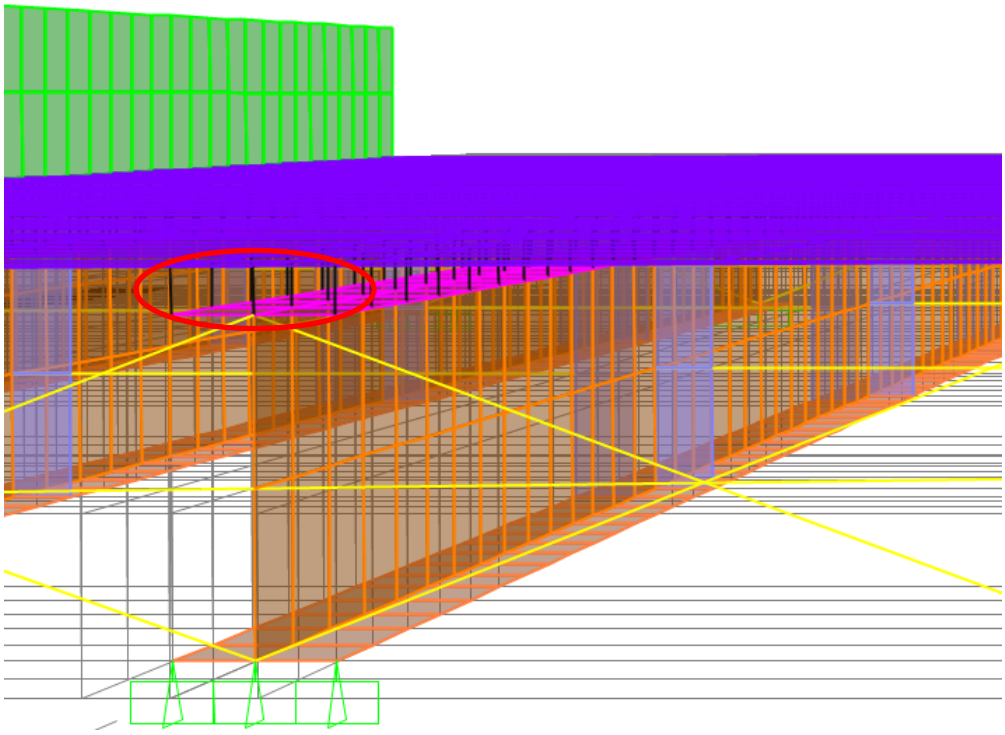

Figure 4.24 Rigid links in the FE model

The C-shape lateral bracing was modeled as beam element with the same cross section shown in the drawing. The beam element was connect to the middle point of the web of the wide flange. Since the beam element cannot directly transfer moment to the web in the FE model, steel plates modeled as shell

elements were built to connect the beam to the web in middle section, while in the two boundaries, cross bracings were introduced between steel girders to increase the lateral stiffness of the bridge. The light pink elements shown in Figure 4.24 presents the steel plates. Cross lateral bracing in the boundaries can also be found in the figure.

The boundary condition of the bridge was modeled as pin semi-roller connection. In the pin boundary side, except r2, other restraints u1, u2, u3, r1, and r3 were fixed. In the semi-roller side, except u1 and r2, other restraints u2, u3, r1, and r3 were fixed. Strings were introduced in the semi-roller side to add stiffness in u1 direction. By trial and error to matching the natural frequencies from the FE model to those from field data, the stiffness of the string was set to be 1400kips/in. The boundary condition of the Meriden Bridge in the FE mode can be found in Figure 4.25.

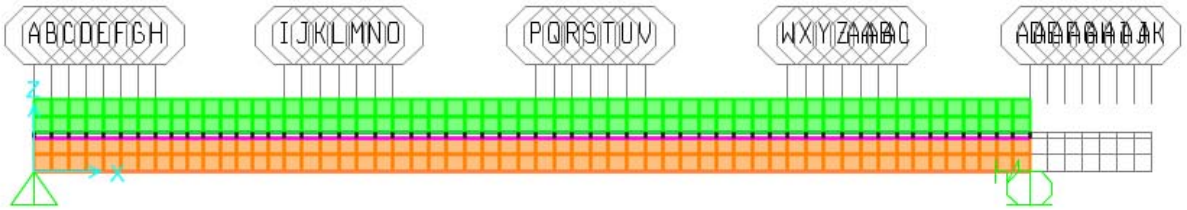

Figure 4.25 Boundary condition of the Meriden Bridge in the FEM

The FE model has a total number of 31,662 degree-of-freedoms, 4758 shell elements and 1464 beam elements. By running the modal analysis in the SAP2000, the natural frequency and mode shapes can be determined. The natural frequencies of the first seven modes from the FE model were 4.44, 5.57, 6.78, 9.77, 14.17, 14.89, and 18.15Hz, respectively. Figure 4.26 shows the mode shapes from the FE model.

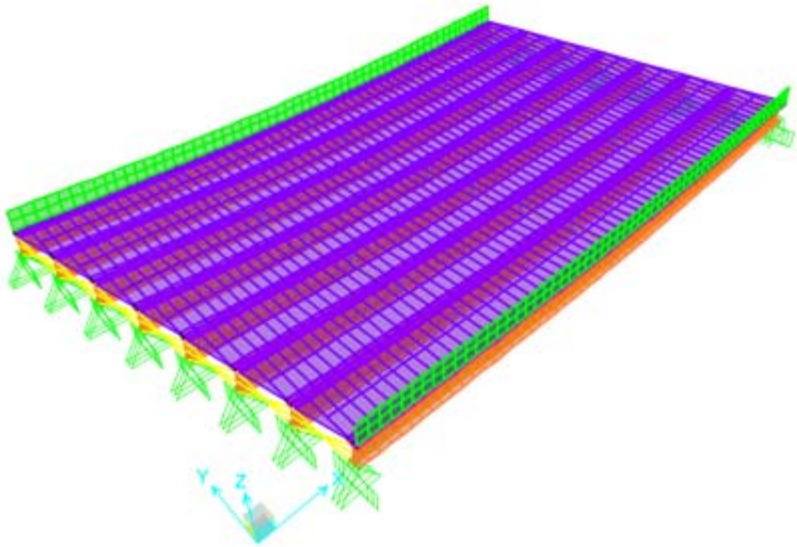

a) Mode 1 (1st bending mode = 4.44 Hz)

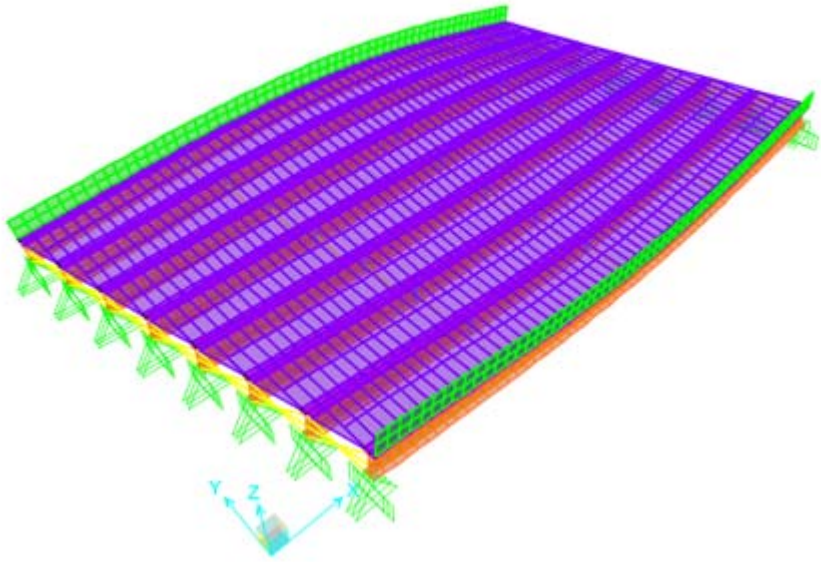

b) Mode 2 (1st torsional mode = 5.57 Hz)

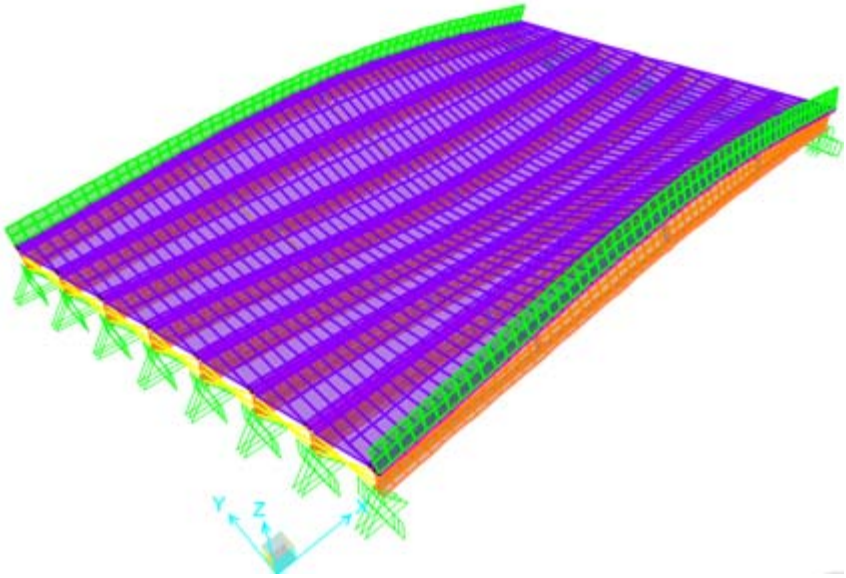

c) Mode 3 (1st plate bending mode = 6.78 Hz)

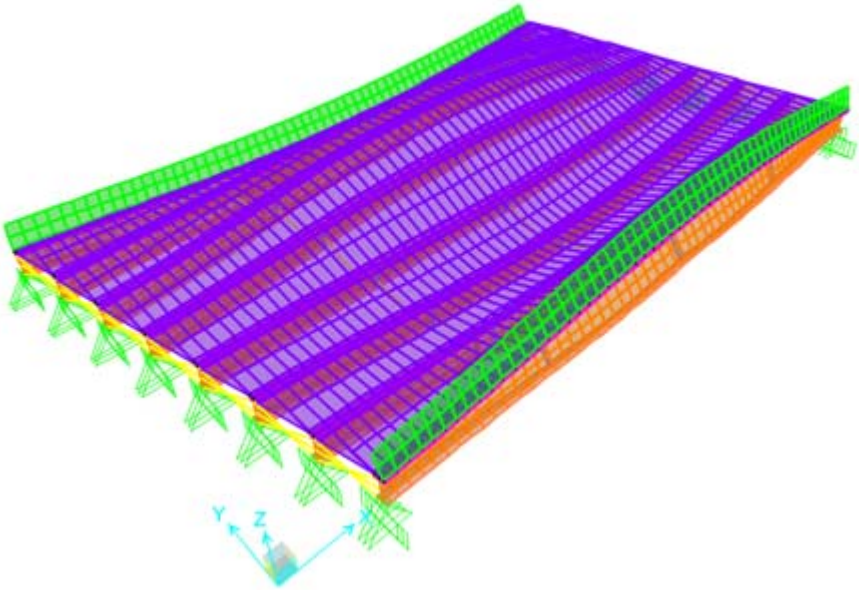

d) Mode 4 (Local mode = 9.77 Hz)

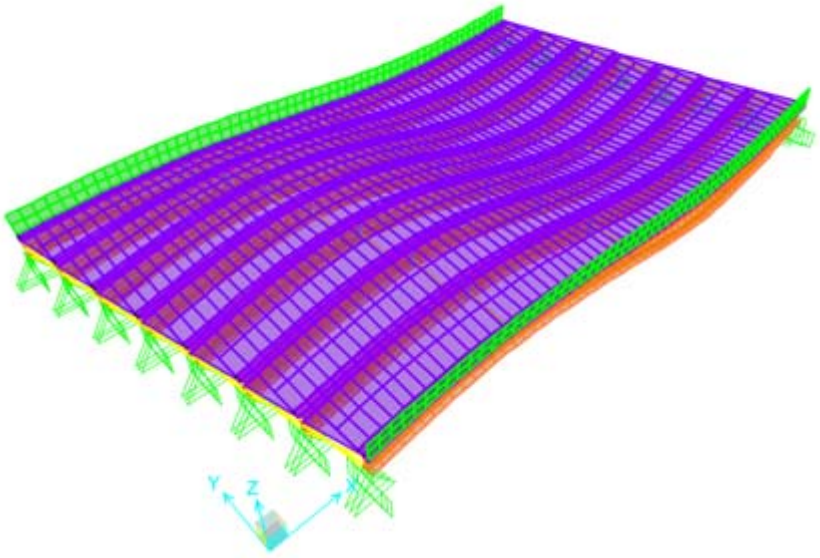

e) Mode 5 (2nd bending mode = 14.17 Hz)

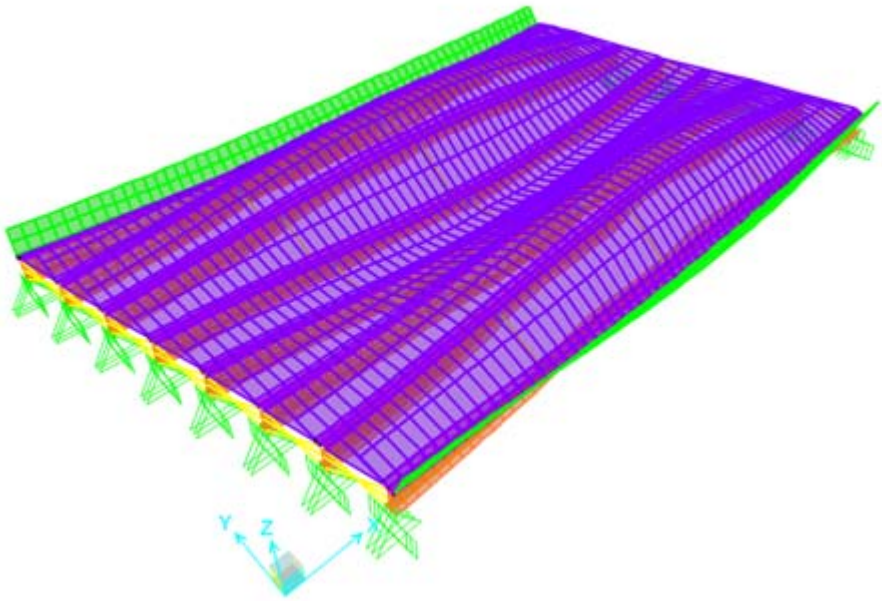

f) Mode 6 (2nd plate bending mode = 14.89 Hz)

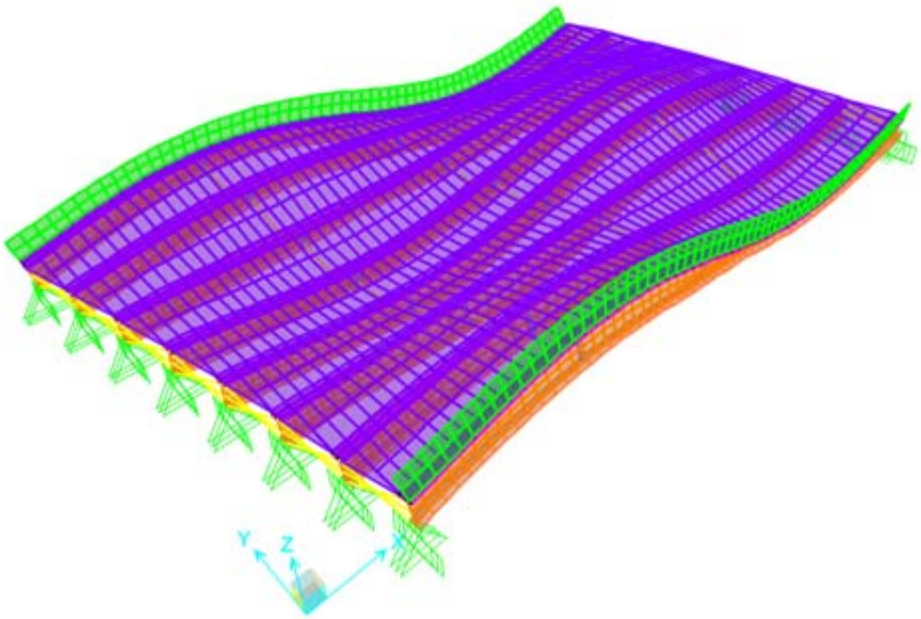

g) Mode 7 (2nd torsional mode = 18.15 Hz)

Figure 4.26 Mode shapes of the Meriden Bridge in FE model

4.7 Comparison of the System Identification Results

System identification of the Meriden Bridge from WSSs, wired monitoring system, and FE model are presented from section 4.4 to 4.6, respectively. A comparison of the identified natural frequencies of the Meriden Bridge can be found in Table 4.1.

Table 4.1 Comparison of the identified natural frequencies of the Meriden Bridge

Mode No.	Wired system (Hz)	FE model (Hz)	WSSs (Hz)	FE model Diff (%)	WSSs Diff (%)
1	4.50	4.44	4.19	1.33	6.89
2	5.63	5.57	N/A	1.07	N/A
3	6.63	6.78	6.81	2.26	2.71
4	9.00	9.77	N/A	8.56	N/A
5	13.31	14.17	13.63	6.46	2.40
6	15.31	14.89	N/A	2.74	N/A
7	17.94	17.94	N/A	1.17	N/A

Assume the identified natural frequencies from the wired system are baseline data, generally, good identification results can be observed from the FE model and WSSs. Since the monitoring data from the wired system and WSSs were obtained from different time, the identified natural frequencies from the two systems were reasonably matched. However, since all the WSSs were deployed along one of the middle girders on the Meriden Bridge, some torsional and plate bending modes could not be identified from the WSSs. In addition, some modes were not identified from the WSSs could also be explained by the fact that external excitation were not strong enough. Given the deployment of wireless and wired monitoring system, and development of a FE model, and system identification of the Meriden Bridge, full-scale monitoring of an in-service highway bridge has been fulfilled in the chapter.

4.8 Summary

This Chapter has covered a full-scale implementation of WSSs for bridge health monitoring. A WSSN with five Imote2 wireless sensors as leaf nodes and one Imote2 as gateway node were deployed on the Meriden Bridge in Connecticut. *RemoteSensing* application was used for the leaf nodes to collect bridge vibration data due to external traffic. Natural frequency, damping ratio and mode shape of the Meriden Bridge were then identified using the FDD algorithm. In addition, a wired SHM system was also installed on the Meriden Bridge. System identification of the Meriden Bridge was also performed by using monitoring data from the wired system. Furthermore, a FE model of the Meriden Bridge was developed using SAP2000 software. By comparing the identification results from the WSSN, wired monitoring system and FE model, the feasibility of bridge health monitoring by using WSSN has been validated.

CHAPTER 5 TEMPERATURE EFFECTS ON THE IDENTIFIED NATURAL FREQUENCIES OF THE MERIDEN BRIDGE

5.1 Introduction

Most of the published research has indicated that change in temperature has a great impact on material properties and boundary conditions, which consequently affect the stiffness and natural frequencies of the bridges. Since the natural frequencies are proportional to the square root of Young's modulus, decreasing Young's moduli of concrete and steel by increasing temperature can cause the natural frequencies of the bridge decrease. On the other hand, when the temperature is below 0^{o}C, the boundary conditions of the bridge may change, which can also change the natural frequencies. Normal changes in natural frequencies of the bridge due to temperature variation should not be alarmed, however, changes in natural frequencies due to damage can be masked by the normal changes with temperature variation, which makes the damage detection algorithms difficult in the real world.

In order to provide useful information to bridge owner for decision making regarding to the stability of the bridge, it is critical to study the correlation between temperature and natural frequencies change. Clearly, such study about the pattern of changes in natural frequencies due to temperature is valuable in finding a solution to differentiate the changes in natural frequencies due to damage from those due to normal temperature variation. In this research, a study of the temperature effects on the bridge natural frequencies is presented based on one-year monitoring data from the wired long-term monitoring system installed on the Meriden Bridge.

5.2 Evaluation of Temperature Effects on Identified Natural Frequencies

A long-term wired monitoring system was installed on the Meriden Bridge. The gauge plan and data acquisition were discussed in Chapter 4. In this section, one-year monitoring data from the piezoelectric accelerometers and RTDs were investigated. The monitoring period was from March 2013 to March 2014. Each data set consisted of 300 seconds with sampling rate of 2048Hz. The measurements were selected every hour during this period. The recording system was down occasionally due to power outage, so the

data were not recorded continuously every day. A total number of 4177 data sets were analyzed which consists 47.7% of the total 8760 data sets in one year. However, as four seasons were represented in the data sets, the data were sufficient with a large range of temperature to be useful for statistical analysis. In addition, the FDD algorithm was employed to identify the natural frequencies of the Meriden Bridge due to its advantages of fast speed and accuracy.

Figure 5.1 shows time history of the temperature from March 2013 to March 2014. The temperature data was obtained from one RTD sensor on girder 2. A clear fluctuation of the temperature on girder 2 can be observed during this period. Note that the temperature data from different RTDs were compared, no significant difference was observed.

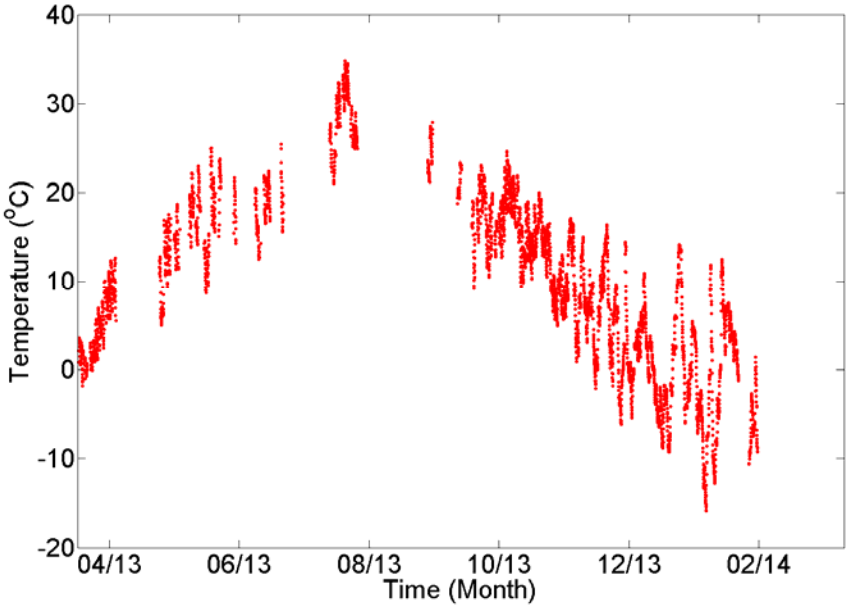

Figure 5.1 Temperature variations on girder 2 from March 2013 to March 2014

Figure 5.2 plots the first seven modes of the Meriden Bridge identified from FDD algorithm below 20Hz. Similar trend of the identified frequency vs temperature can be found for all the modes.

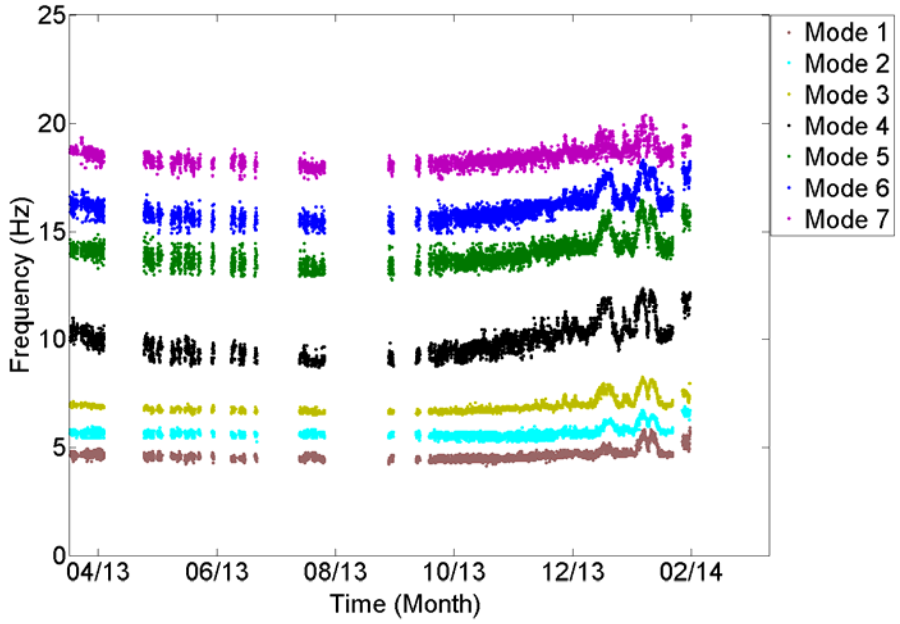

Figure 5.2 Identified natural frequencies of the first seven modes from March 2013 to March 2014

Correlation between the temperatures and identified natural frequencies can be observed from Figure 5.3. This figure plots time history of the normalized natural frequencies and temperature. For each type of data (temperature and natural frequencies for different modes), the normalized data was calculated by subtracting the mean value of one-year data set and then over the absolute maximum value in the new data set (original data minus mean value of one-year data). By doing this, the normalized data will fluctuate with zero mean and between –1 and 1. From the figure, it is observed that the natural frequencies decrease as the temperature increases, while the natural frequencies increase as the temperature decreases. High natural frequencies generally occur at low temperature. In addition, greater fluctuation of the natural frequencies can be found below freezing point which starts around December 2013 in the plot.

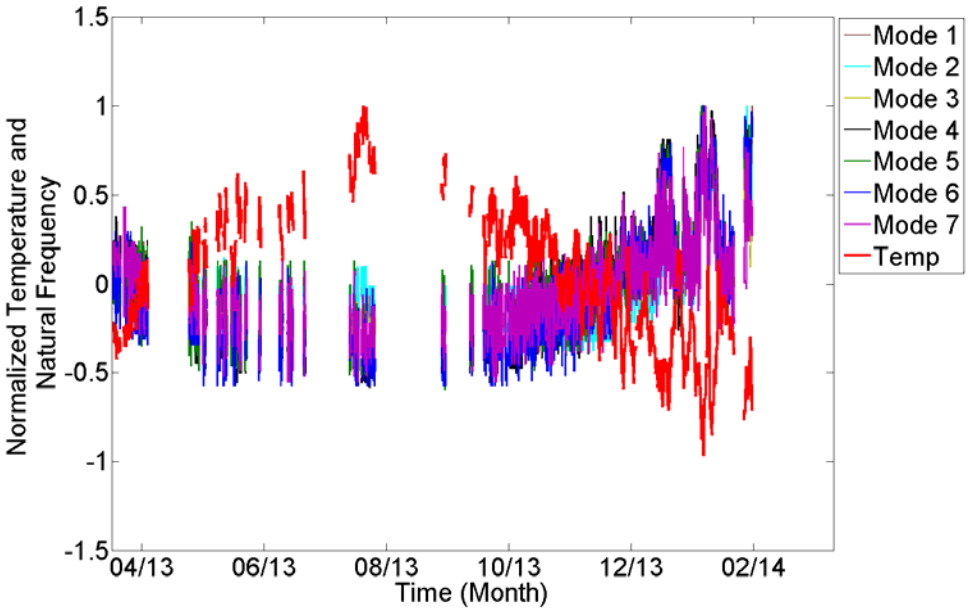

Figure 5.3 Normalized temperature and natural frequencies from March 2013 to March 2014

Table 5.1 lists the basic statistics of the temperature and identified natural frequencies of the first seven modes from March 2013 to March 2014. During this period, the temperature range was from -15.82 ^{o}C to 34.76 ^{o}C while the natural frequencies of the seven identified modes varied by 16.9% to 42.5% which are higher than those (14% to 18%) presented in Peeters and Roeck (2001). It can be explained that larger temperature range has been observed in this research than that shown in Peeters and Roeck's work. It may cause greater fluctuation in natural frequencies. On the other hand, since the observed lowest temperature was -15.82^{o}C which is much lower than -8^{o}C in their work, it may also affect natural frequencies. In order to find the relationship between temperature and identified frequencies, regression analysis is performed in next section.

Table 5.1 Basic statistics of the temperature and the identified natural frequencies

	Mean	Standard Deviation	Minimum	Median	Maximum	Maximum Difference
Temp (^{o}C)	9.08	9.74	-15.82	8.94	34.76	—
Mode 1 (Hz)	4.84	0.25	4.13	4.63	5.75	39.2%
Mode 2 (Hz)	5.70	0.27	5.25	5.63	6.88	31.1%
Mode 3 (Hz)	6.94	0.35	6.50	6.81	8.25	26.9%
Mode 4 (Hz)	10.05	0.79	8.69	9.94	12.38	42.5%
Mode 5 (Hz)	14.13	0.67	12.75	14.06	16.44	28.9%
Mode 6 (Hz)	16.17	0.67	14.93	16.06	18.42	23.4%
Mode 7 (Hz)	18.48	0.43	17.44	18.44	20.38	16.9%

5.3 Regression Analysis between the Modal Frequencies and Temperatures

In order to correlate the natural frequencies and the corresponding temperature for the one-year monitoring data, both linear and nonlinear models are used. The equation of the linear model can be presented in slope-intercept form as shown below:

$$y = a + bx \tag{5.1}$$

where y is a vector of dependet variable, which represents natural frequency, and x is a vector of independent variable, which represents temperature in this study, b is the slope and a is the y-intercept.

The linear model is used to fit identified natural frequencies of each mode with temperature seperately. The fitted parameters of the linear model in terms of slope and intercept for all the data sets are listed in Table 5.2, in which another parameter is also shown. Adjusted R^2 is a modification of R^2 which measures the goodness-of-fit of the linear model. It is usually a value between 0 and 1. The higher of the value, the better of the fit. Figure 5.4 shows the linear fit for all the identified natural frequencies vs temperature.

Table 5.2 Parameters for the linear regression model for all the modes

Mode	Parameter	Value
Mode 1	Adjusted R^2	0.409
	a	4.793
	b	-0.017
Mode 2	Adjusted R^2	0.303
	a	5.832
	b	-0.015
Mode 3	Adjusted R^2	0.652
	a	7.200
	b	-0.029
Mode 4	Adjusted R^2	0.832
	a	10.720
	b	-0.740
Mode 5	Adjusted R^2	0.663
	a	14.636
	b	-0.0560
Mode 6	Adjusted R^2	0.713
	a	16.701
	b	-0.058
Mode 7	Adjusted R^2	0.605
	a	18.815
	b	-0.035

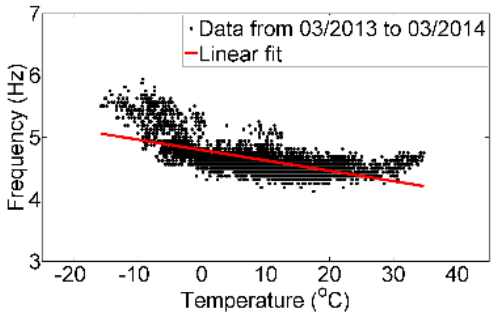

a) Mode 1

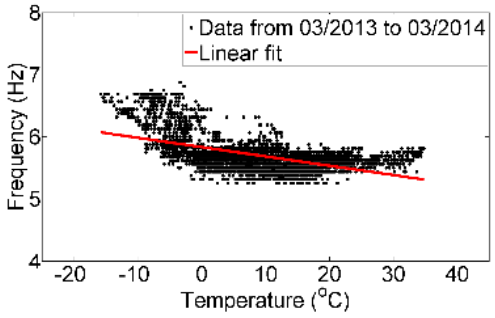

b) Mode 2

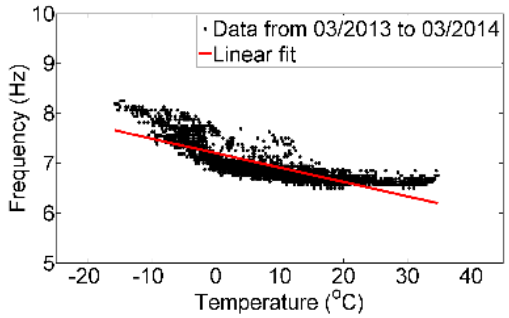

c) Mode 3

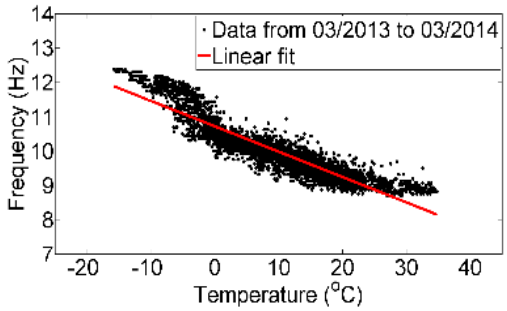

d) Mode 4

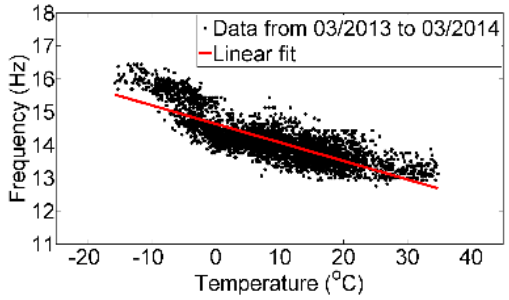

e) Mode 5

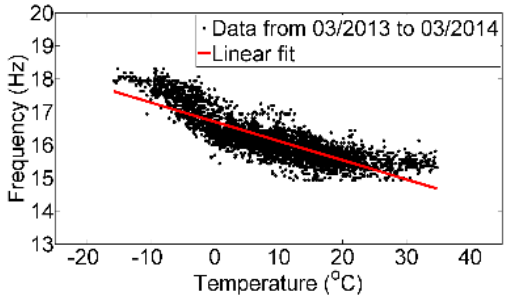

f) Mode 6

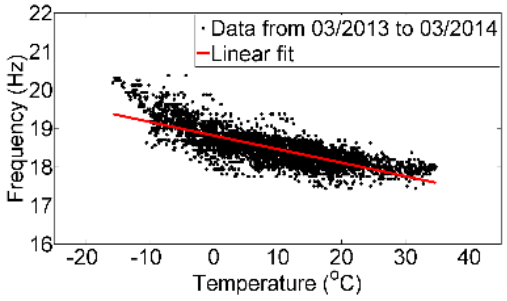

f) Mode 7

Figure 5.4 Linear fit for identified natural frequency vs temperature

The nonliear model used in this study is Gauss fit model. It is a nonlinear least-squares fit to a function with four unknown parameters. The equation of the Gauss model is:

$$y = a + be^{-\left(\frac{x-c}{d}\right)^2} \tag{5.2}$$

where y and x are the same in Equation 5.1, a the offset, b is the amplitude, c is the centroid, d is related to the peak width. The fitted parameters of the Gauss model are listed in Table 5.3. In addition, the modal frequency vs temperature for all the modes with Gauss nonlinear fit are presented in Figure 5.5.

Table 5.3 Parameters for the Gauss nonliear model for all the modes

Mode	Parameter	Value
Mode 1	Adjusted R^2	0.618
	a	4.507
	b	1.394
	c	-22.145
	d	16.663
Mode 2	Adjusted R^2	0.534
	a	3001.5
	b	-2995.9
	c	16.319
	d	-1656.8
Mode 3	Adjusted R^2	0.819
	a	6.578
	b	273.4
	c	-142.330
	d	57.334
Mode 4	Adjusted R^2	0.891
	a	8.575
	b	68.420
	c	-138.960
	d	74.482
Mode 5	Adjusted R^2	0.749
	a	13.264
	b	995.500
	c	-197.700
	d	76.763
Mode 6	Adjusted R^2	0.800
	a	15.443
	b	3.989
	c	-30.138
	d	-27.836

Mode 7	Adjusted R^2	0.663
	a	17.901
	b	632.910
	c	-217.590
	d	84.834

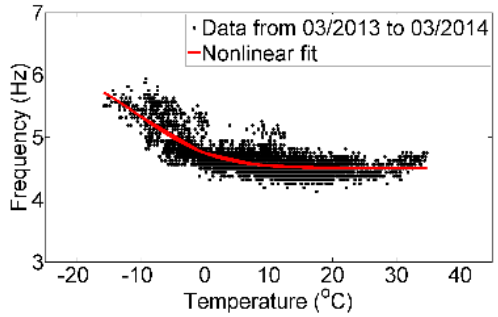

a) Mode 1

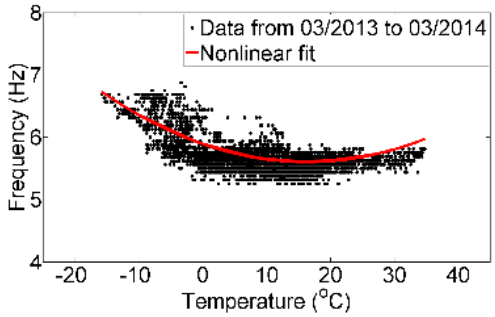

b) Mode 2

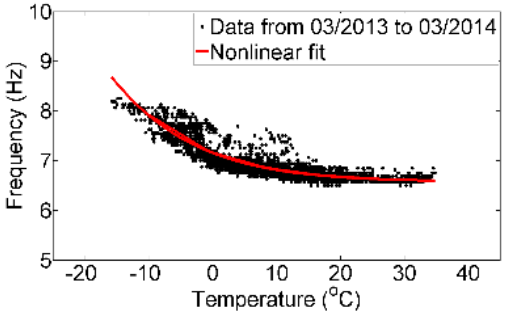

c) Mode 3

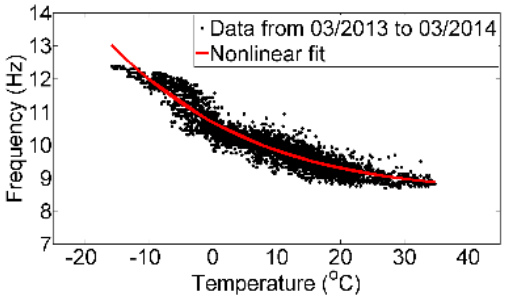

d) Mode 4

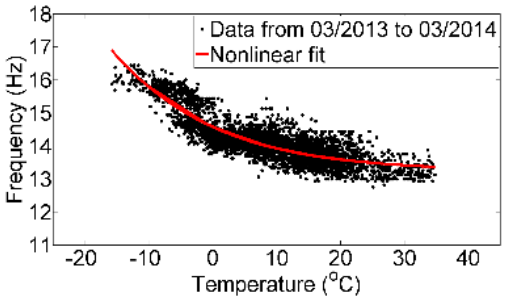

e) Mode 5

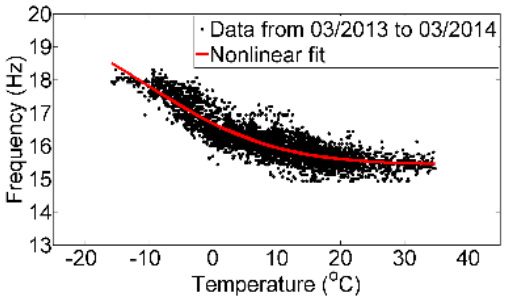

f) Mode 6

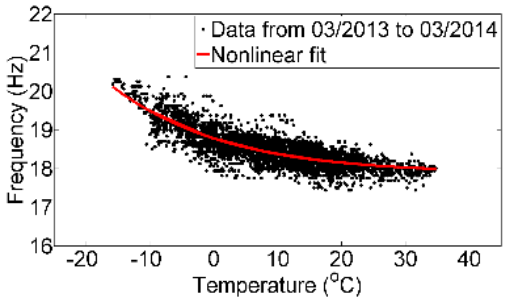

f) Mode 7

Figure 5.5 Nonlinear fit for identified natural frequency vs temperature

From Table 5.2 and Table 5.3, it can be observed that the adjusted R^2 value of the nonlinear regression is always higher than that of the linear regression for each mode, which indicates that the Gauss nonlinear fit is better than the linear fit for all the modes. Based on the linear and nonlinear fit from Figure 5.4 and Figure 5.5, some observations can be found:

1) For all the modes, the natural frequency exhibits a downward trend throughout the temperature range which is the same as expectation; this may be explained that the overall stiffness of the concrete and steel decreases as the temperature increases;
2) For mode 1, 2, and 6, generally, the natural frequency decreases as the temperature increases, however, a slight uptrend appears at the right tail when the temperature is high; this may be caused by the expansion of joints due to the increase of temperature which causes tighter boundary condition. For other modes, it shows flat trend at the right tail when the temperature is high; the reason could be all factors that affect natural frequency reach a balance leading to the unchanged frequencies;
3) For all the modes, the downward trend below freezing point is higher than that over freezing point. This can be explain by three reasons: first, the increased stiffness of the concrete and steel when temperature decreases; second, the freezing of accumulated dust and moisture can cause fixity at the girder support; third, the surface asphalt does not have any effect at high temperature,

but becomes very stiff at cold temperature, especially below freezing point. These reasons can significantly increase the total stiffness of the structure, and cause the natural frequency increases faster than when the temperature decreases below freezing point.

By analyzing the nonlinear fit curve, it can be deduced and replaced by bilinear fit with one below freezing point and one over. In addition, by fitting the data sets with bilinear regression model, the changing ratio of natural frequency with the temperature below and over freezing point can be quantified by comparing the slope of the two fitted lines. The parameters of the bilinear fit are listed in Table 5.4. The bilinear fit of the natural frequency vs temperature is shown in Figure 5.6.

Table 5.4 Parameters of the bilinear fit for all the modes

Mode	Temperature	Parameters	Value
Mode 1	Below 0 ^{o}C	Adjusted R^2	0.476
		a	4.697
		b	-0.0629
	Over 0 ^{o}C	Adjusted R^2	0.121
		a	4.641
		b	-0.007
Mode 2	Below 0 ^{o}C	Adjusted R^2	0.392
		a	5.758
		b	-0.063
	Over 0 ^{o}C	Adjusted R^2	0.303
		a	5.646
		b	-0.003
Mode 3	Below 0 ^{o}C	Adjusted R^2	0.594
		a	7.165
		b	-0.075
	Over 0 ^{o}C	Adjusted R^2	0.478
		a	6.983
		b	-0.015
Mode 4	Below 0 ^{o}C	Adjusted R^2	0.645
		a	10.670
		b	-0.136
	Over 0 ^{o}C	Adjusted R^2	0.776
		a	10.431
		b	-0.055

Mode 5	Below 0 °C	Adjusted R^2	0.597
		a	14.478
		b	-0.140
	Over 0 °C	Adjusted R^2	0.463
		a	14.342
		b	-0.037
Mode 6	Below 0 °C	Adjusted R^2	0.568
		a	16.675
		b	-0.117
	Over 0 °C	Adjusted R^2	0.525
		a	16.406
		b	-0.039
Mode 7	Below 0 °C	Adjusted R^2	0.495
		a	18.630
		b	-0.093
	Over 0 °C	Adjusted R^2	0.442
		a	18.691
		b	-0.027

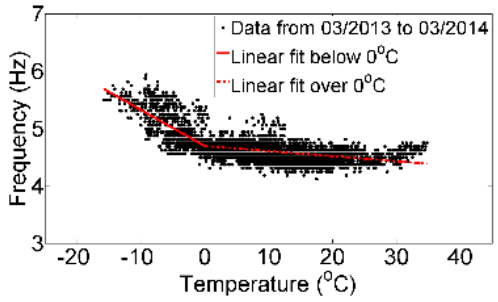

a) Mode 1

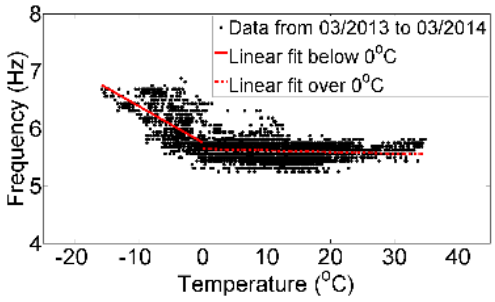

b) Mode 2

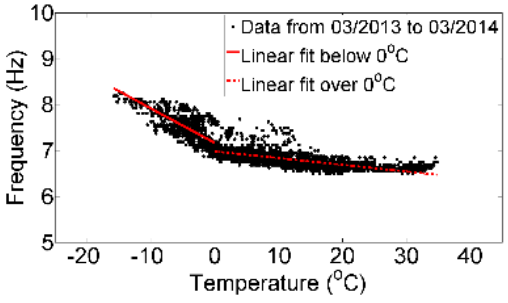

c) Mode 3

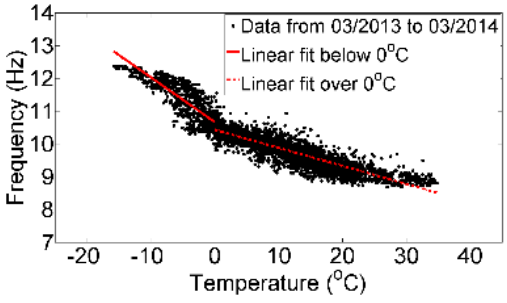

d) Mode 4

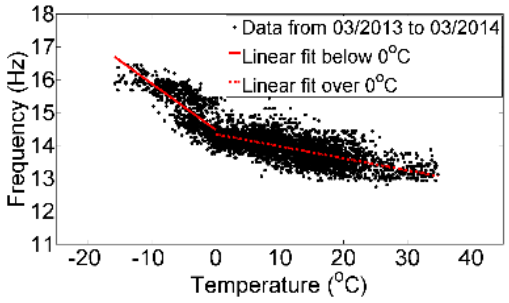

e) Mode 5

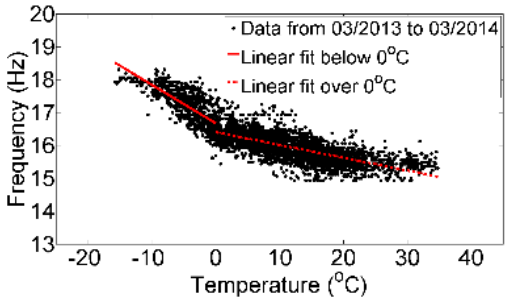

f) Mode 6

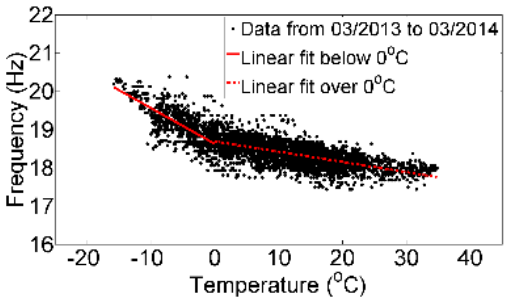

f) Mode 7

Figure 5.6 Bilinear fit for identified natural frequency vs temperature

By comparing the parameters in Table 5.4, the slope of the linear fit below freezing point over that over freezing point for mode 1 to 7 can be determined to be 8.99, 21, 5, 2.47, 3.78, 3, and 3.44 times, respectively. This indicate the rate of change for the natural frequencies below freezing point compared to that over freezing point. As seen from those values, no general pattern has been found. They show different value at different modes. However, it can be found that the natural frequencies increase much faster when the temperature decreases below freezing point than that over freezing point.

5.4 Summary

As described by this Chapter, one-year monitoring data of the Meriden Bridge from March 2013 to March 2014 were investigated to determine the temperature effects on the identified natural frequencies. During this period, the temperature range was from -15.82 °C to 34.76 °C while the natural frequencies of the seven identified modes varied by 16.9% to 42.5%. The relationship between modal frequencies and

temperatures were correlated by linear and Gauss nonlinear regression curve fitting. Generally, Gauss nonlinear fit showed better goodness-to-fit than linear fit. The regression analysis revealed downward, upward, and flat trends of the natural frequencies exhibited at specific temperature ranges for different modes. Bilinear fit with temperature below and over freezing point was performed for all the modes to quantify the rate of change in natural frequency with changing temperature. A greater impact of the temperature below freezing point was observed.

CHAPTER 6 DAMAGE DETECTION WITH UNCERTAINTIES USING MACHINE LEARNING ALGORITHMS

6.1 Introduction

While installing monitoring system on bridges is becoming more common nowadays, the applicability of SHM on bridge damage detection is still challenging by many sources of uncertainties. Those uncertainties include operational and environmental variability present in any measured structural response and could affect the robustness of most damage detection algorithms. In fact, those effects on structural response from uncertainties have been cited as one of the major challenges to the transit of SHM technology from lab research to real world implementation. This Chapter discuss how two machine learning algorithms, Mahalanobis squared distance (MSD), and auto-associative neural network (AANN), are employed for bridge damage detection in order to remove the effect from operational and environmental variability. Those machine learning algorithms are purely data-based methods and can learn the correlation of damage-sensitive features from the structural response data in presence of the operational and environmental variability. They overcome the drawback that changes of structural properties from real damage could be masked by the operational and environmental variations. Firstly, a 12-bay truss bridge is tested in laboratory with random excitation under different structural state conditions. Uncertainties from operational and environmental variability are simulated by varying mass conditions with different weight and locations, while the damage is simulated by a losing bolt in one of the truss elements. Next, the two machine learning algorithms are applied to analyze the one-year monitoring data from the Meriden Bridge.

6.2 Machine Learning Algorithms for Damage Detection

Machine learning is a branch of artificial intelligence and concerns the construction and study of systems that can learn relationship from data. In the context of SHM, it means that one can learn to detect damage based on given measurements from the structure of interest. The use of machine learning offers the

possibility of automating the SHM process, which is removing the need for intervention of human judgment (Farrar and Worden 2013).

Damage detection in a structure involves four levels of procedure from low to high: existence, location, type and extent of damage. Existence and possible location of the damage could be done by unsupervised machine learning which means the algorithms operate unlabeled examples, i.e., input where the desire output is unknown. In the context of SHM, it means detect novelty based on training data from normal operating condition of the structure or system. During the monitoring, a model of normal operating condition is firstly created, then newly acquired monitoring data are compared with the model. If there are any significant deviations from the model, the algorithms indicate that novelty has been found and that could be possible damage in the structure. The advantage of this approach is if the training data is generated from a model, only the undamaged condition is required which will simplify matter considerably. From a practical point of view, there is no need to damage the structure of interest. It is very critical for civil engineering infrastructure, since each structure is unique, and no structure owner wants to damage their structures especially for in-service highway bridges. However, the drawback is that, the efficiency of the algorithms heavily depends on the training data. If the training data can include as large as the distribution of normal operating condition, then the algorithm is more efficient to detect damage.

On the other hand, type and extend of damage needs supervised machine learning algorithms which means algorithms are trained on labeled examples, i.e., input where the desired output is known. In SHM, data from every conceivable damage situation should be available as training data. Two possible sources of such data are from physical based modeling (finite element analysis) and experiment. They both have limitations. Firstly, modeling is biased if the structure is materially or geometrically complex. In addition, the damage is difficult to model. Furthermore, it is difficult to model the future loading for the structure. Secondly, in order to accumulate enough training data, it is necessary to make copies of the structure and damage it all the different ways that might occur. This makes the experiment no better than modeling. And in reality, it is not easy or possible to damage civil engineering infrastructure such as highway bridges. Therefore, in most cases of damage detection in civil engineering infrastructure, where damage

data are not usually available, unsupervised machine learning algorithms are more suitable to detect the existence or possible location of damage. In this section, two machines learning algorithms are introduced which are Mahalanobis squared distance (MSD) and auto-associative neural network (AANN).

6.2.1 Mahalanobis Squared Distance (MSD)

In general, the Mahalanobis distance is a distance measure used for multivariate statistics which takes into account the correlation between the variables, but not depend on the scale of the observations. It is capable of learning linear relationship between damage-sensitive feature vectors and detect outliers based on a Gaussian-distributed normal condition (Noh et al. 2009, Figueiredo et al. 2010). This means that the Mahalanobis distance algorithm depends on the implicit assumption that the data can be characterized by its first two statistical moments – the mean and variance (or covariance for multidimensional feature vectors). The feature vectors could be autoregressive model coefficients by fitting time series monitoring data, or identified natural frequencies from the structure of interest. This limitation simplifies the problem to one where the probability density function of the Gaussian distributed is fixed by estimation of a small number of parameters. The advantage is that computational effort is reduced and computational speed is accelerated. The drawback is that the assumption of Gaussianity is by no means always merited.

Considering the training data matrix X, where each column contains a feature vector extracted from monitoring data obtained from healthy structure under normal operating condition, with multivariate mean vector $\bar{x}$ and covariance matrix Σ. The Mahalanobis distance is now used as in standard outlier detection to provide a damage index, *DI*, between feature vectors of the training matrix and testing matrix *y* (potential outlier or damage):

$$DI_i = \sqrt{(\mathrm{y}_i - \bar{\mathrm{x}})^T \Sigma^{-1} (\mathrm{y}_i - \bar{\mathrm{x}})} \tag{6.1}$$

Some authors (Figueiredo et al. 2010) used the Mahalanobis squared distance (MSD) with following equation:

$$DI_i = (\mathrm{y}_i - \bar{\mathrm{x}})^T \Sigma^{-1} (\mathrm{y}_i - \bar{\mathrm{x}}) \tag{6.2}$$

And the MSD is used in this study to amplify the *DI* amplitue. The assumption of the MSD algorithm is that if a feature vector is obtained from data collected on the damaged structure that might inlcude similar sources of opeational and environmental variability, the vector will be further from the mean feature vectors corresponding to the healthy condition as quintified by the *DI*. It means that both feature vectors obtained from healthy and unhealthy data share the same covariance matrix. On the other hand, if an observation is extracted from an healthy condition and it is multi-dimensional Gaussian distributed, then its *DI* in Equation 6.2 will be Chi-square distributed. Therefore, the outliers or damage can be detected if the *DIs* above a certain level of confidence.

6.2.2 Auto-Associative Neural Network (AANN)

The AANN algorithm is an approach that is able to deal with non-Gaussian distributed normal conditions. The application of this algorithm was first proposed by Pomerleau (1993) with a feedforward, multilayer perceptron neural network that maps an input on to some output through hidden layers. An architecture of the algorithm is shown in Figure 6.1. The AANN architecture consists of three hidden layers: the mapping layers, the bottleneck layer, and de-mapping layer. The nodes in each layer are known as neurons. The mapping and de-mapping layers consist of neurons with hyperbolic tangent sigmoid transfer function while the bottleneck and output layers are formed using linear neurons. Each neuron carries out a local calculation and passes the results from previous layer to the neurons in the next layer. The number of inputs and number of nodes in each layer is problem specific. This architecture forces the network to learn nonlinear correlations present among the input feature vectors. More details about AANN network and how to assign number of nodes in each layer can be found in the references (Kramer 1991, Sohn et al. 2002).

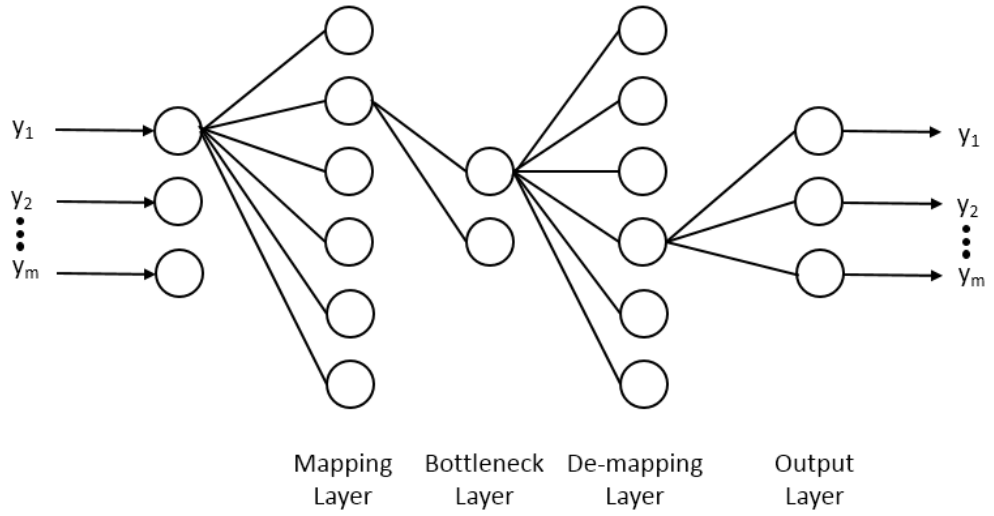

Figure 6.1 Network architecture of an AANN

In the SHM field, the AANN algorithm is trained to characterize the underlying dependency of the identified features on the unobserved operational and environmental factors by treating that unobserved dependency as hidden intrinsic variables in the network architecture. By learning the correlations between feature vectors, it can reveal the unobserved sources of variability that influence the structural properties. The correlation is represented through the bottleneck layer, where the number of neutrons depends on number of unobserved independent variables that affect the structural response. For example, as the natural frequency of bridge is related to stiffness and mass, then the number of neurons on the bottleneck layer could be assigned to two. In addition, once the network has been trained using features from the healthy condition, then the predicted error of the AANN will grow when the features that come from a potential damaged condition are fed to the network. In both training and testing process, the features are from the structure when it is subjected to operational and environmental conditions. For the test matrix Y, where each column contains a feature vector extracted from monitoring data, the residual errors E are given by:

$$E = Y - \hat{Y} \tag{6.3}$$

where $\hat{Y}$ is the estimated training feature vectors that are the ouput of the AANN algorithm. A quantitative measure of damage, *DI*, is defined to be the Euclidean distance between the test features and the output features of the neural network:

$$DI = \sqrt{\sum_{i=1}^{m} (y_i - \hat{y}_i)^2} \tag{6.4}$$

where y is the test features and $\hat{y}$ is the output from the neural network from training features, m is the number of features. If the features from test data are realted to an undamaged state, then $Y \approx \hat{Y}$ and $DI \approx 0$. Alternatively, if the features are from a damaged state, the neutral network is not able to map the inputs on to themselves, the residual errors will increase, resultsing in the DI deviates from zero, thereby indiating an abnormal condition in the structure that cannot be attributed to the operational and environmental variability reprensented in the training data. The advantage of the AANN algorithem is to learn nonlinear correlations among the feature vectors, while the drawback is once the size of training data is large, the computational efforts will increase significantly, and computational time will be very long.

6.3 Evaluation of Machine Learning Algorithms on a Lab-Scale Truss Bridge for Damage Detection

6.3.1 Testbed description

A 12-bay lab-scale three dimensional truss structure (Figure 6.2) is used in this section as a test bed for lab experimental test. Each bay is 1.5 ft, therefore, the truss bridge is 18 feet by 1.5 feet and 1.5 feet. The boundary condition for this truss bridge is pin-roller connection (Figure 6.3). The pinned end can rotate freely about z-axis only and other two rotational and three translation movements are restricted. The roller end can only move in the longitudinal direction and rotate about z-axis.

Figure 6.2 Three dimensional 18 feet long 12 bay truss bridge

Figure 6.3 Boundary condition of the truss bridge: pin (left) and roller (right) support

All the truss members are made up of 1045-steel tubes with external diameter of 0.752 in and internal diameter 0.617 in. Brass collars are provided at both ends of the tube so that it can be connected to a steel bracket at the joint. In addition, the bracket joints are designed to be flexible so that each tube can be easily removed or collected. More detailed description of this truss bridge can be found in Dahal (2013).

6.3.2 System identification of the truss bridge

The experimental test was performed in the SHM lab in the Department of Civil and Environmental Engineering at University of Connecticut. Figure 6.4 shows connection diagram for the equipment setup with WSSs. The shaker is connected to the truss bridge with a rod shown in Figure 6.5. Five Imote2 wireless sensor nodes are installed on the top of the front truss located in Figure 6.6. One gateway node is connected to the computer and receives data from the five leaf nodes. The shaker starts vibrating and causing the truss bridge to vibrate and the Imote2 wireless nodes placed on the truss bridge will measure the vibration. The experimental setup can be found in Figure 6.6.

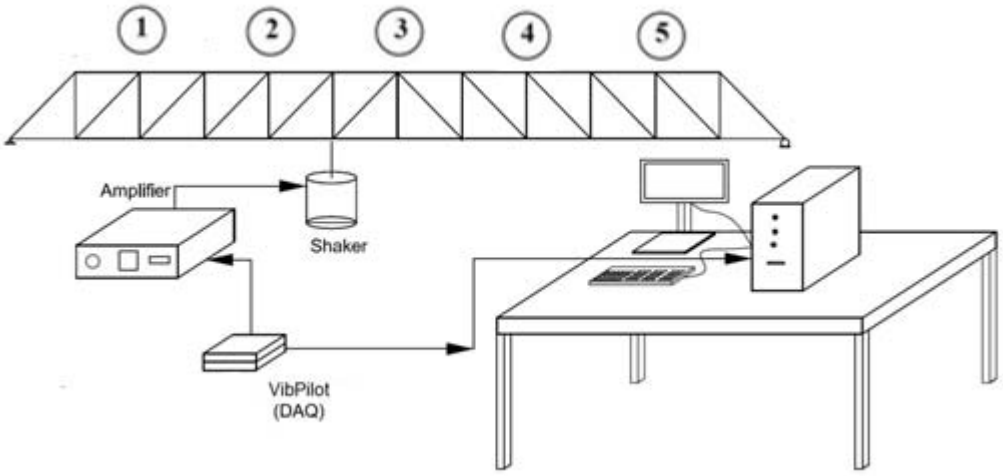

Figure 6.4 Connection block diagram for the lab test with WSSs

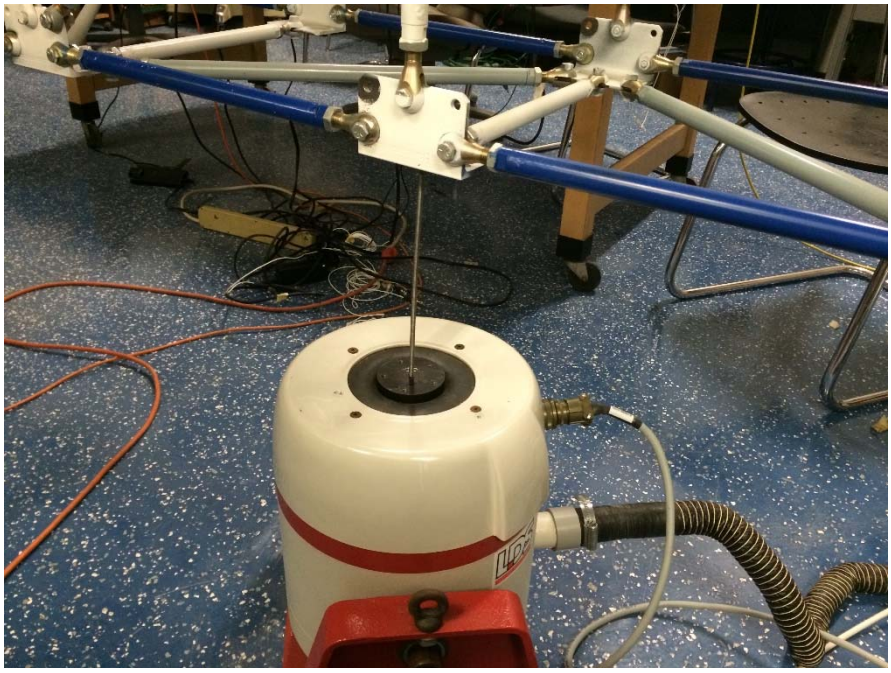

Figure 6.5 Connection of the shaker and truss bridge

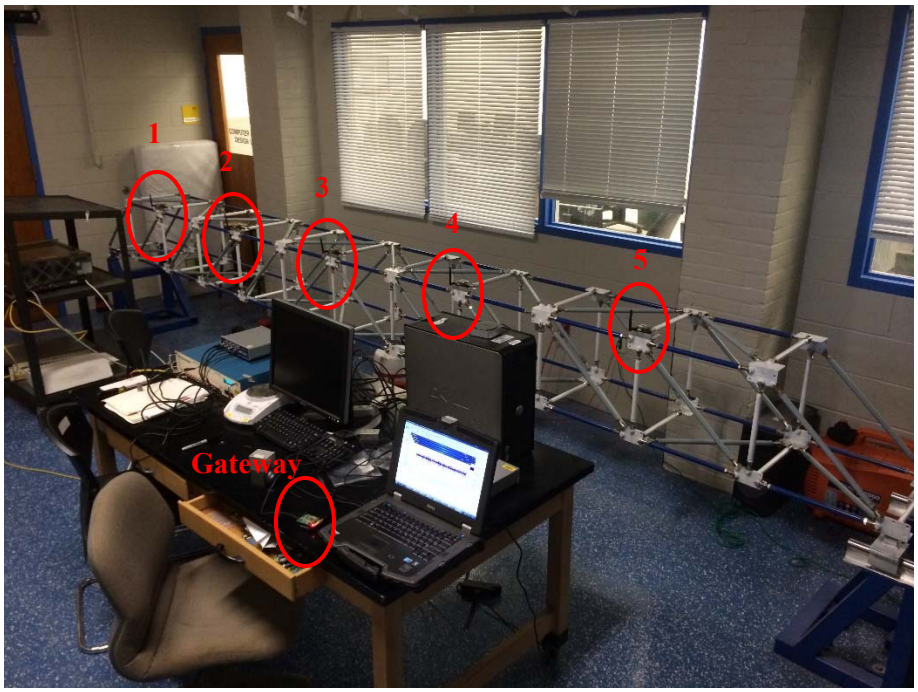

Figure 6.6 Equipment setup for the test with WSSs

Several tests have been performed in the lab to get robust results. For each test, a white noise vibration was introduced to the truss bridge through the magnet shaker. The vibration data was collected with *RemoteSensing* application in the ISHMP Toolsuite discussed in Chapter 3. All the five leaf nodes measured 3-axis acceleration (x, y, and z) and sent data back to the gateway node. In each test, 84,000 data points with 280Hz sampling rate (300 seconds data) were used for measuring the truss bridge vibration. A time history plot of the five Imote2 wireless nodes can be found in Figure 6.7.

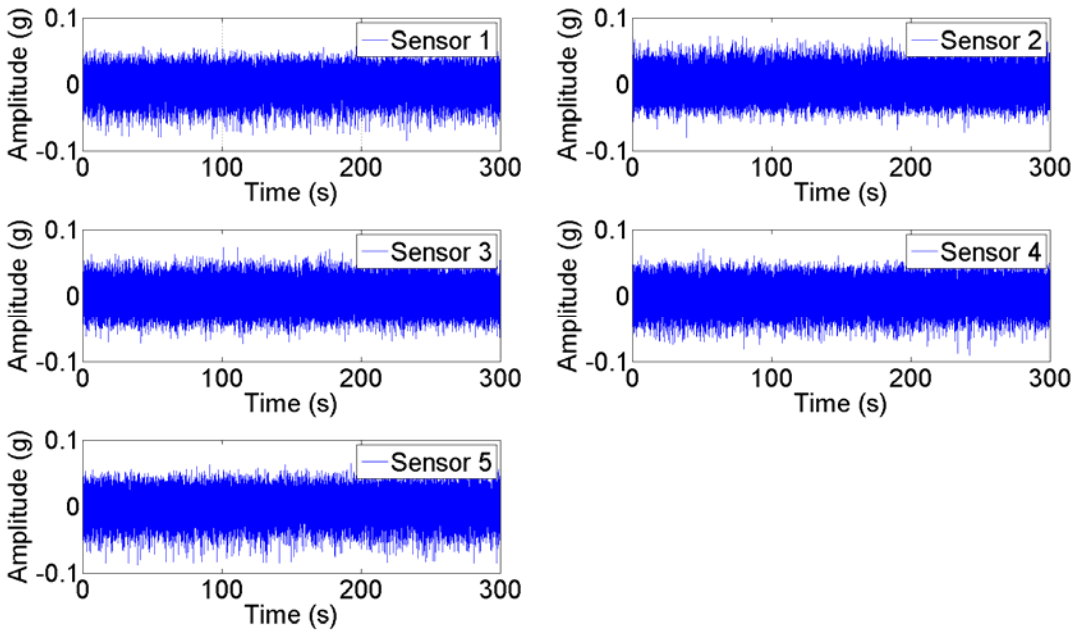

Figure 6.7 Time history of the five Imote2 wireless nodes

FDD technology was employed to determine the modal properties of the truss bridge, where sampling frequency was 280Hz, Nfft was 4480. Figure 6.8 shows PSD plot for each sensor. The singular value plot is presented in Figure 6.9.

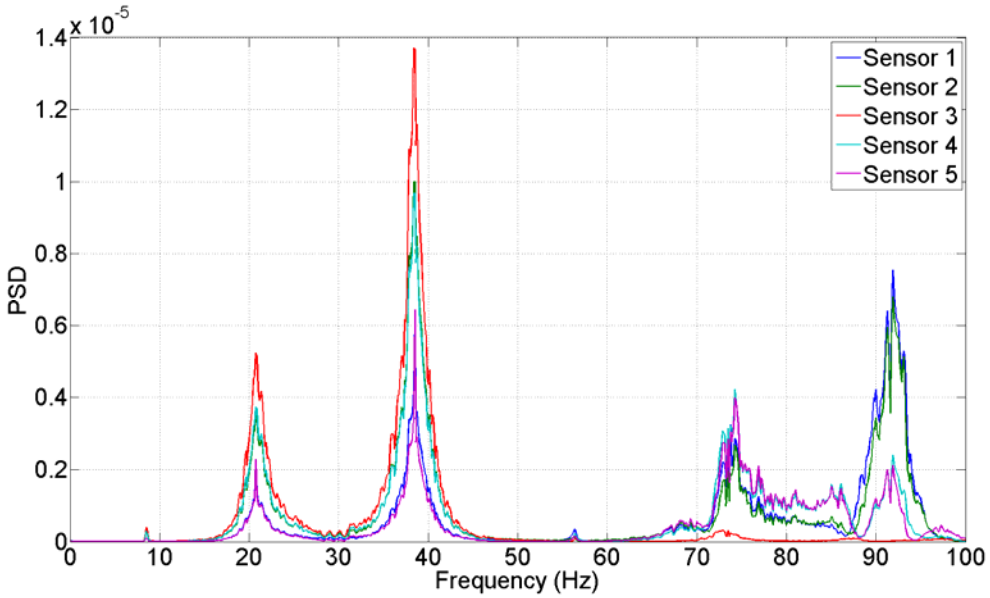

Figure 6.8 PSD for all the sensors from the WSSs

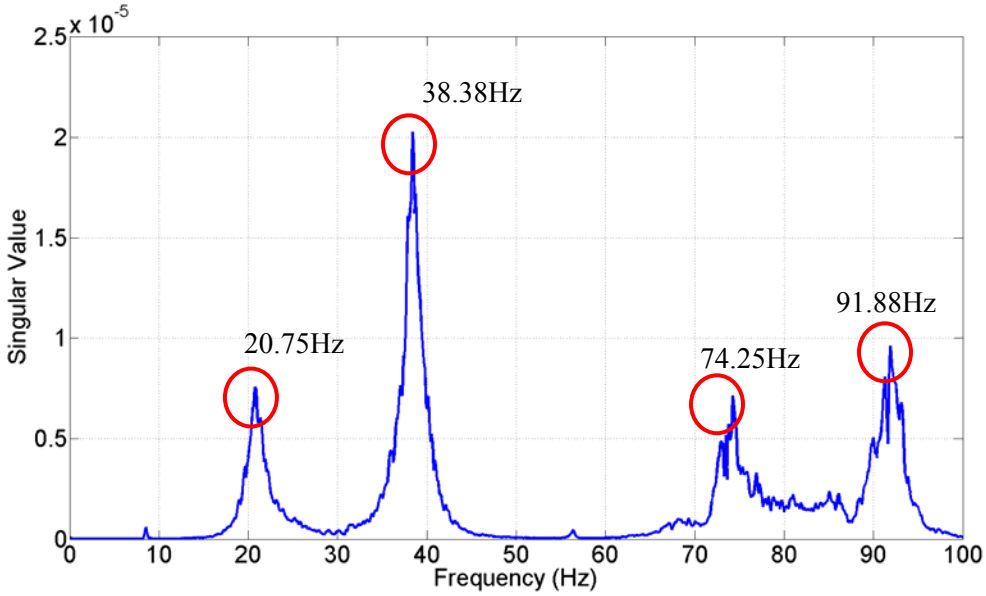

Figure 6.9 Singular value plot for the truss bridge from the WSSs

From the singular value plot, first four modes can be identified with 1st bending mode, 1st horizontal mode, 2nd bending mode, and 2nd horizontal mode. The natural frequencies are 20.75Hz, 38.38Hz, 74.25Hz, and 91.88Hz. The mode shape for each mode is shown in Figure 6.10.

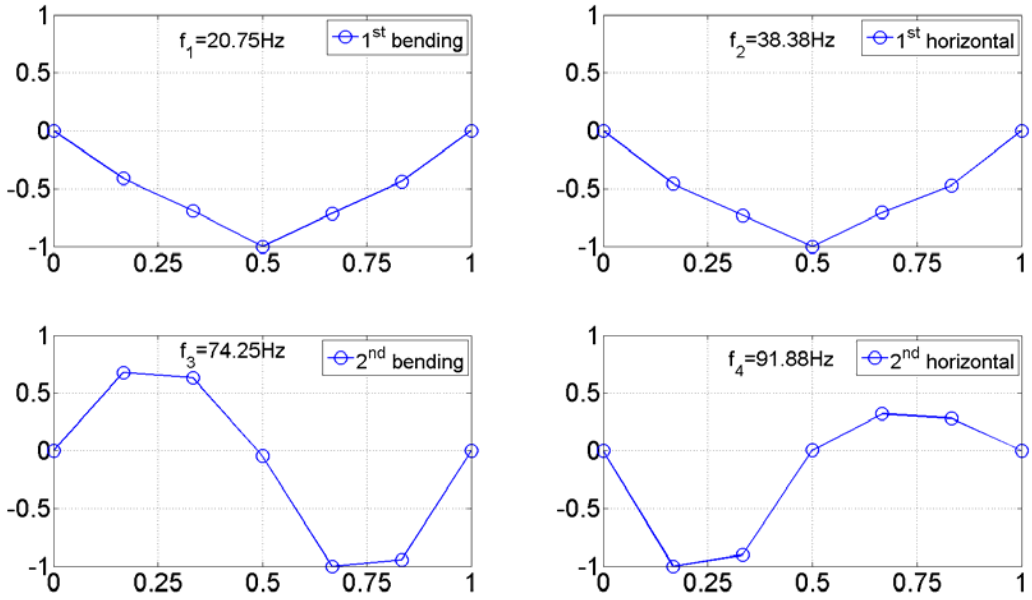

Figure 6.10 First four mode shape for the truss bridge from the WSSs

From Figure 6.8 to 6.10, the first four natural frequencies and mode shapes have been found for the lab-scale 12-bay truss bridge from a WSSN with five imote2 nodes. System identification using wired monitoring system and FE model has been done by Dahal (2013). A comparison between the three methods can be found in Table 6.1 below.

Table 6.1 Comparison of the identified natural frequencies of the truss bridge

Mode No.	Wired system (Hz)	FE model (Hz)	WSSs (Hz)	FE model Diff (%)	WSSs Diff (%)
1	20.88	19.31	20.75	7.52	0.62
2	39.00	41.84	38.38	7.28	1.59
3	74.25	72.49	74.25	2.37	0
4	91.75	90.22	91.88	1.67	0.14

6.3.3 Experimental setup

The 12-bay lab-scale truss bridge (Figure 6.2) was used as a test bed for damage detection. A wired monitoring system was installed on the truss bridge for collecting data from different state conditions.

Eleven PCB piezoelectric accelerometers (353B33) were mount on the top front face of truss bridge. They were labeled from 1 to 11 shown in Figure 6.11. The accelerometer has a sensitivity of 100mV/g, a frequency range from 1 to 4000Hz, and a measurement range of ± 50g. A signal conditioner was used to supply power to the accelerometers as well as collecting data from them. The power amplifier, permanent magnetic shake, VibPilot and SO Analyzer data acquisition system are the same in Chapter 3.

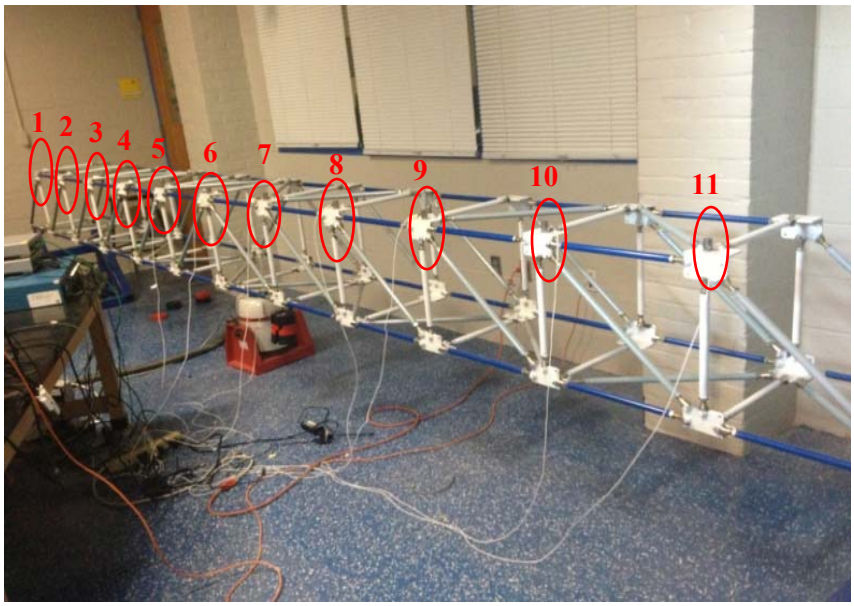

Figure 6.11 The 12-bay lab-scale truss bridge for damage detection with wired monitoring system

6.3.4 Test procedure for damage detection

Two tests were performed in the lab. One was to evaluate the machine learning algorithms on damage detection with simulated temperature variation, and the other one was to detect damage with traffic effect. The temperature variation was simulated by adding different lumped mass at the same location of the truss, while the traffic effect was simulated by adding same mass at different locations of the truss. In addition, the damage was introduced by losing one bolt between a truss element and the steel bracket as shown in Figure 6.12.

Figure 6.12 Damage introduced into the truss bridge

In Test 1, truss bridge at six different states were tested as shown in Table 6.2. For State 1, it is the baseline condition without any variability and damage. State 2 and 3 are also labeled as undamaged condition but with variability. The variability was introduced to the structure by adding different mass at the same location. The mass was added at the bottom front face of the truss below sensor 7, shown in Figure 6.13. State 4 is a damaged condition with a loose bolt between one truss element and steel bracket which located at the bottom back face of the truss below sensor 6. The location of the damage can also be found in Figure 6.13. State 5 and 6 are also damaged conditions but with variability effect. For each state, 300 seconds time series data were collected from a band-limited random excitation in the frequency range of 5 to 2014 Hz. The sampling rate was 256Hz. In addition, each 300 seconds was divided to 50 data sets with each of 6 seconds (1536 data points). Therefore, there were 300 data sets in Test 1.

Table 6.2 Data labels of the bridge state conditions in Test 1

Label	**State Condition**	**Description**
State 1	Undamaged	Baseline condition
State 2	Undamaged + variability	6kg mass added@6
State 3	Undamaged + variability	12kg mass added@6
State 4	Damaged	Loose bolt
State 5	Damaged + variability	Loose bolt + 6kg mass@6
State 6	Damaged + variability	Loose bolt + 12kg mass@6

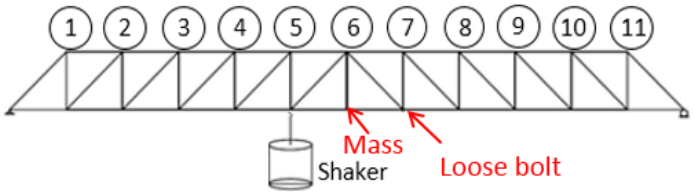

Figure 6.13 Loose bolt and adding mass location in Case 1

In Test 2, truss bridge at twelve different states were tested as shown in Table 6.3. For State 1, it is the baseline condition without any variability and damage. State 2 to 6 are labeled as undamaged condition but with variability. The variability was introduced to the structure by adding the same mass at different locations. The 3kg mass were added at both the bottom back and front face of the truss below sensor 2 to 10 in sequence, shown in Figure 6.14. State 7 is the damaged condition with a loose bolt the same as in Test 1. State 7 to 12 are damaged conditions with the same variability effect from state 2 to 6. Similar to Test 1, for each state, 300 seconds time series data were collected from a band-limited random excitation in the frequency range from 5 to 2014 Hz. The sampling rate was 256Hz. In addition, each 300 seconds data was divided to 50 data sets with 6 seconds (1536 data points) for each. Therefore, there were 600 data sets in Test 2.

Table 6.3 Data labels of the bridge state conditions in Test 2

Label	State Condition	Description
State 1	Undamaged	Baseline condition
State 2	Undamaged + variability	Two 3kg mass@2
State 3	Undamaged + variability	Two 3kg mass@4
State 4	Undamaged + variability	Two 3kg mass@6
State 5	Undamaged + variability	Two 3kg mass@8
State 6	Undamaged + variability	Two 3kg mass@10
State 7	Damaged	Loose bolt
State 8	Damaged + variability	Loose bolt + Two 3kg mass@2
State 9	Damaged + variability	Loose bolt + Two 3kg mass@4
State 10	Damaged + variability	Loose bolt + Two 3kg mass@6
State 11	Damaged + variability	Loose bolt + Two 3kg mass@8
State 12	Damaged + variability	Loose bolt + Two 3kg mass@10

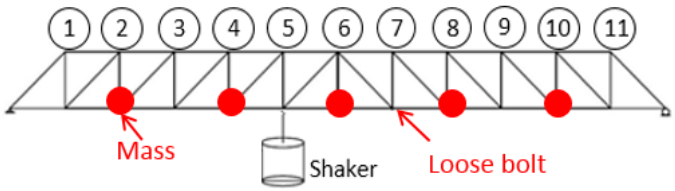

Figure 6.14 Loose bolt and adding mass location in Case 2

6.3.5 Data analysis

Two machines learning algorithms MSD and AANN were employed in this study to detect the damage in the two tests. Even these two algorithms have different mathematical equations, the procedure for implementing them are in a common steps which is presented in Figure 6.15. First, obtain time series data from the monitoring structure under operational and environmental condition (the structure is assumed to be at healthy condition); second, extracted damage-sensitive feature vectors from time series data collected from last step and train the machine learning algorithms with feature vectors. The feature vectors could be coefficients of autoregressive (AR) model by fitting the time series data, or identified natural frequencies of the structure. Which one to use depends on different scenarios; third, transform each input feature vector into global *DI* based on different algorithms. The *DIs* should be nearly invariant for the feature vectors from step three; four, setup threshold for certain level of significance; five and the last step, detect outlier of damage based on the training data in step 3 and threshold value in step 4. If robust data normalization has been achieved, the new *DIs* should be determined as outliers when feature vectors are extracted from the time series data from damaged condition even when operational and environmental variability are included.

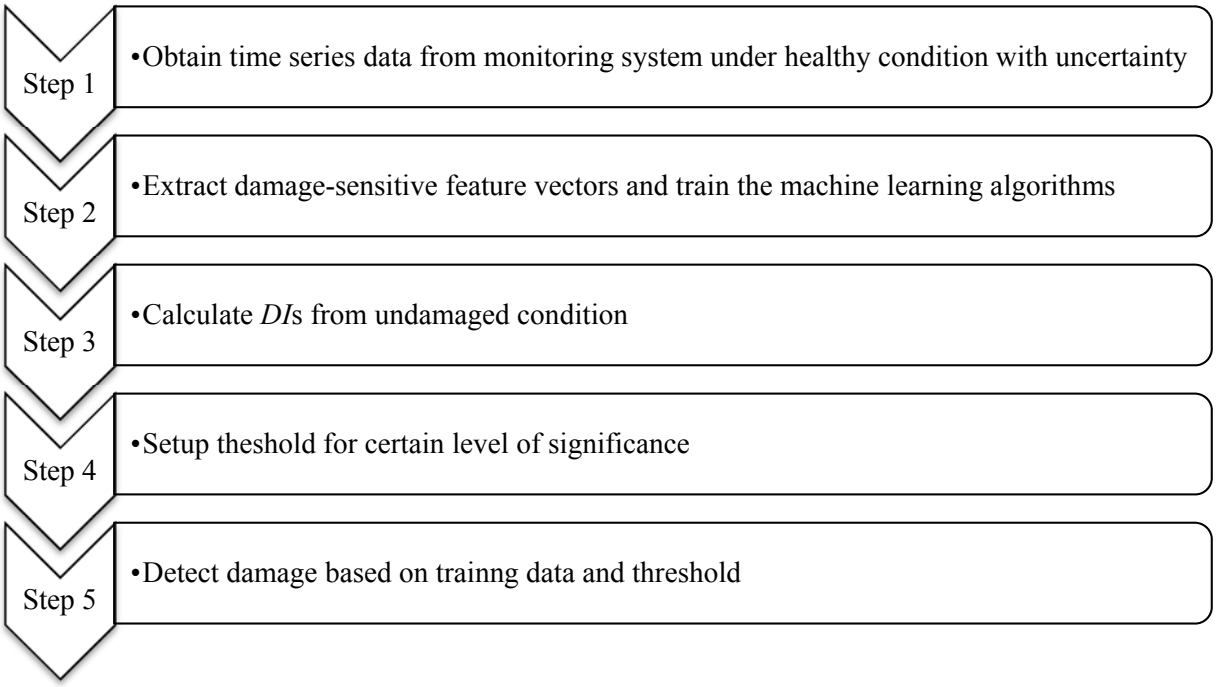

Figure 6.15 Procedure for implementing machining learning algorithms for damage detection

As mentioned before, the damage-sensitive feature vectors for machine learning algorithms could be identified natural frequencies of the structure, or AR coefficients. The natural frequencies could be identified by many time domain or frequency domain algorithms. For example, FDD technology is one of the most efficient frequency domain algorithms for identifying modal frequencies. On the other hand, many observed time series data exhibit serial autocorrelation that are linear association between lagged observations. This suggests that post observations could predict current observations. The AR process models the conditional mean of current observation as a function of several lagged observations. An AR process that depends on p past observations is called an AR model of degree p, denoted by AR(p). The model of AR(p) is:

$$y_t = c + \phi_1 y_{t-1} + \phi_2 y_{t-2} + \cdots + \phi_p y_{t-p} + \varepsilon_t \tag{6.5}$$

where y_t is the measure data at time t, c is constant, ε_t is an uncorrelated random error, ϕ_1 to ϕ_p are p unknown AR model coefficients which are used as damage-sensitive feature vectors. The unknown AR

coefficients can be determined by using least squares method. The order of the AR model p is an unknown integer. A high order model may better match one data but will not generalize to other data set. On the other hand, a low order model may not well fit the time series data. In order to find out optimum model order, some technique needs to be applied.

The Akaike information criterion (AIC) has been demenstrated as one of the most efficient methods for determining AR model order. It is employed in this study to find the optimum model order based on the times series data. The AIC is a measure of the goodness-of-fit of an statsitcal model which is based on the trade-off between fitting accuracy and number of model order. The AR model with lowest AIC value gives optimum model order. In the context of AR model, the AIC is (Figueiredo et al. 2010):

$$AIC = N_d \ln(\varepsilon) + 2N_p \tag{6.6}$$

where N_d is the nunber of predicted data points, N_p is the number of estmated parameters, and ε = SSR/ N_d is the average sum-of-square residual (SSR) errors.

6.3.5a Results: Test 1

AR coefficients by fitting time series data were used as damage-sensitive feature vectors in both Test 1 and Test 2. In order to extract feature vectors from all time series data, an appropriate AR model should be determined. Figure 6.16 shows the AIC values calculated from sensor 6 of baseline data in Test 1. Smaller AIC values indicates a better fit of the time series data. For the time series data from the baseline condition in Test 1, the AIC value converges after AR order 15, suggeting that an AR(15) model is a good start. Figure 6.17 plots the measured and predicted vibration time history data with AR(15) model from sensor 6 of state 1 in Test 1. From the figure it shows an overlap of the two time history data and AR(15) model appears to predict the data very well. Another indication that the AR(15) model predicts the time history data well is from a Gaussian distributed residual errors presented in Figure 6.18. It shows a histogram of the residual errors and imposed Gaussian distribution with mean nearly 0 and standard deviation equals to 2.61 mg.

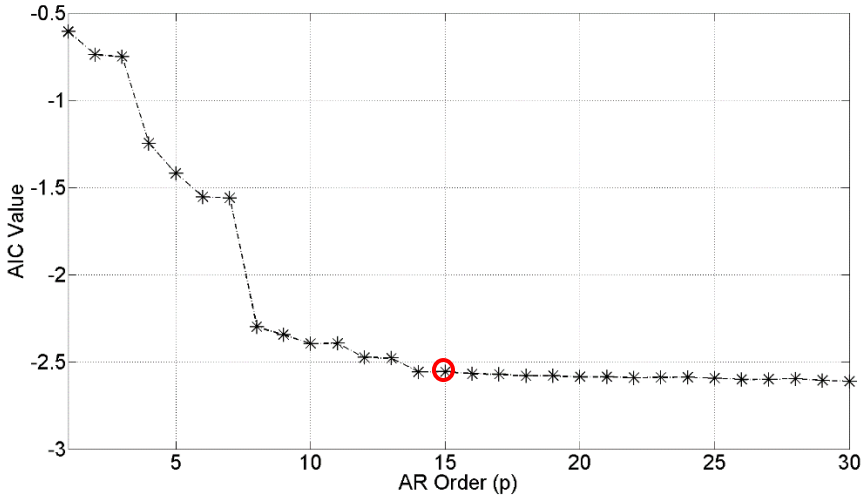

Figure 6.16 AIC values of AR model order in Case 1 (sensor 6 of State 1)

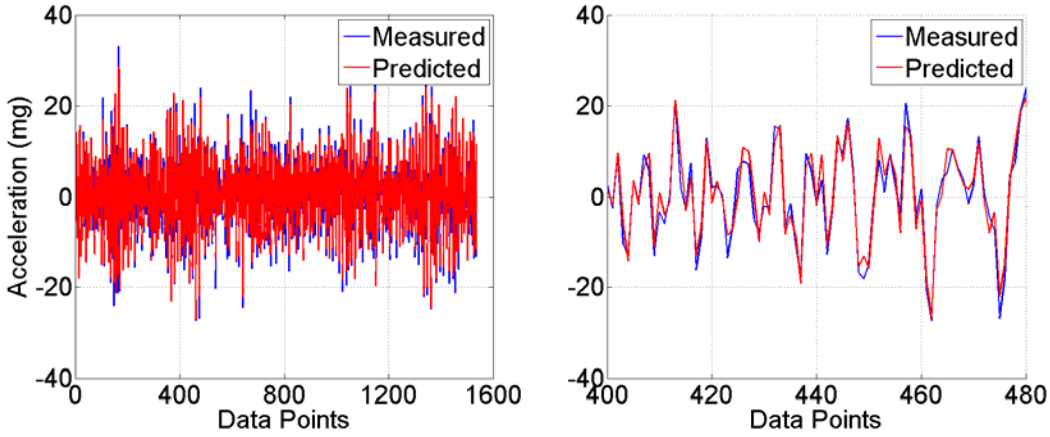

Figure 6.17 Comparison of the measured and predicted time history data using AR(15) model (sensor 6 of State 1 in Test 1)

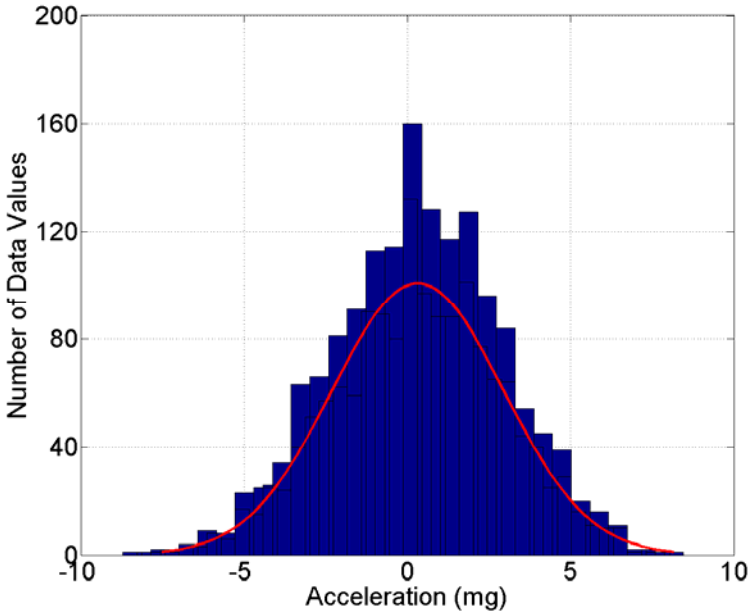

Figure 6.18 AR(15) residual errors histogram with Gaussian distribution (sensor 6 of State 1 in Test 1)

Once the AR model order were identified to be 15 in Test 1, the AR(15) model was used to extract the damage-sensitive feature vectors from all the time series data in Test 1. Note that the AR model order was constant throughout Test 1, but the AR coefficients were expected to change accordantly for different data sets. As mentioned before, the robustness of the machine learning algorithms based on the training data. The larger the distribution of the feature vectors included in the training data, the more efficient of the machine learning algorithms for detecting outliers.

In Test 1, three cases (Case 1, Case 2, and Case 3) were analyzed. Case 1 and Case 2 showed the efficiency of machine learning algorithms on damage detection with different training data. Case 3 showed real world damage detection situation by using machine learning algorithms. In all the cases, the threshold for both of the MSD and AANN algorithms were based on 95% confidence of interval. Assume the AR feature vectors were Gaussian distributed, the MSD *DI* would be chi-square distributed with degree of freedom equal to the AR model order (15) and confidence of interval (95%). While the threshold of the AANN *DI* was determined to be 95% cut off *DI* magnitude from training data. Note that 95% confidence of interval is the same as the partial safety factors during the structural design.

In Case 1 of Test 1, training data were made up of 49 data sets from State 1, while the test data were made up of one time series data set from each state condition from State 1 to 6. As a consequence, the feature vector matrix of training data in Case 1 was 15 × 49 (15 AR coefficients, and 49 data sets), the feature vector matrix of test data was 15 × 6. Figure 6.19 and Figure 6.20 present the damage detection results based on the MSD algorithm and the AANN algorithm, respectively. In the analysis, the AANN architecture was designed to be (2, 6) with two nodes in bottleneck layer, and six nodes in mapping and de-mapping layer. Two nodes in bottleneck layer represents the two underlying parameters (mass and stiffness) driving the changes in modal properties. Note that the performance of the AANN algorithms can be increased by increasing the number of nodes in mapping and de-mapping layer, several trials have been performed with the same data sets in this case, the performance didn't increase too much when the mapping layer nodes was greater than six. In the two figures, the green dash line is the control line based on the threshold value, *DI* value over the control line is classified as damage condition, while undamaged condition is below the control line. Both algorithms can classify State 4 to 6 as damaged condition, however, they also classify State 2 and State 3 as damaged condition which are supposed to be undamaged condition shown in Table 6.2. It means that by training the two machine learning algorithms with only data from State 1 (baseline condition), the machine learning algorithms were not able to separate temperature effect from real damage.

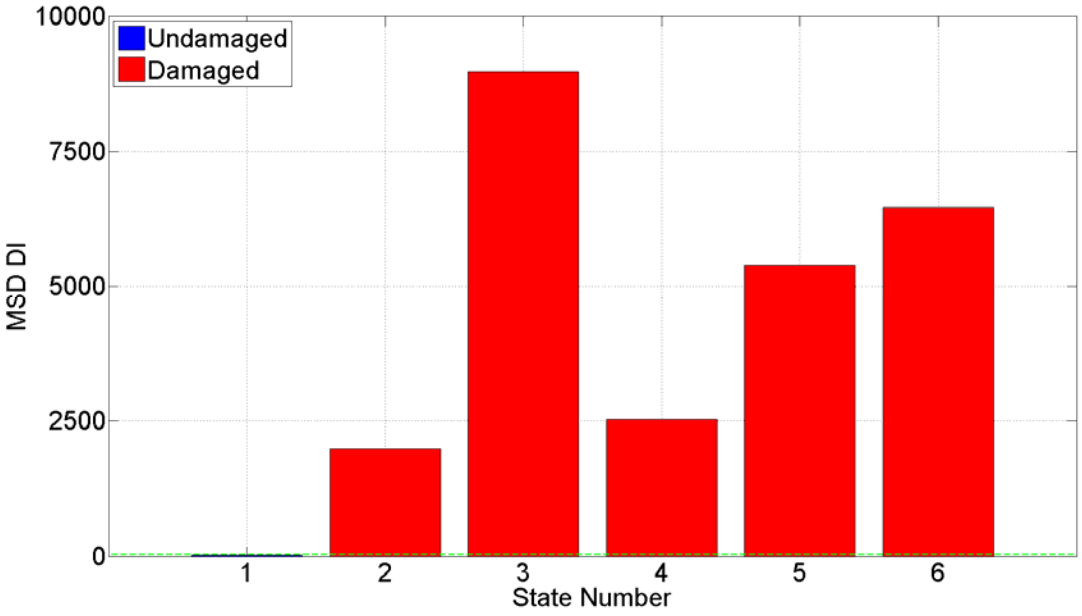

Figure 6.19 MSD using training data from State 1 in Case 1 of Test 1 (sensor 6)

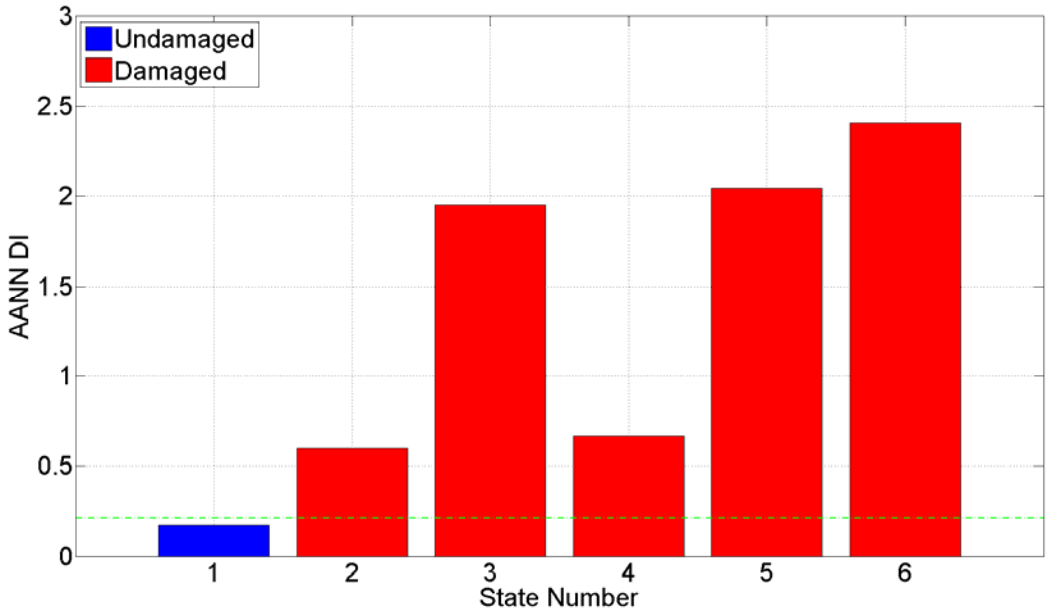

Figure 6.20 AANN using training data from State 1 in Case 1 of Test 1 (sensor 6)

In Case 2 of Test 1, training data were made up of 147 data sets with each 49 sets from State 1 to 3, while the test data were the same in Case 1 with one time series data set from each state condition from

State 1 to 6. As a consequence, the feature vector matrix of training data in Case 2 was 15 × 147 (15 AR coefficients, and 147 data sets), the feature vector matrix of test data was 15 × 6. Figure 6.21 and Figure 6.22 present the damage detection results based on the MSD algorithm and the AANN algorithm, respectively. In the two figures, both algorithms can classify State 4 to 6 as damaged condition, and they classify State 2 and State 3 as undamaged condition which matches the description in Table 6.2. It means that by training the two machine learning algorithms with all undamaged conditions in presence of assumed temperature effect from State 1 to 3, the machine learning algorithms were able to separate temperature effect from real damage.

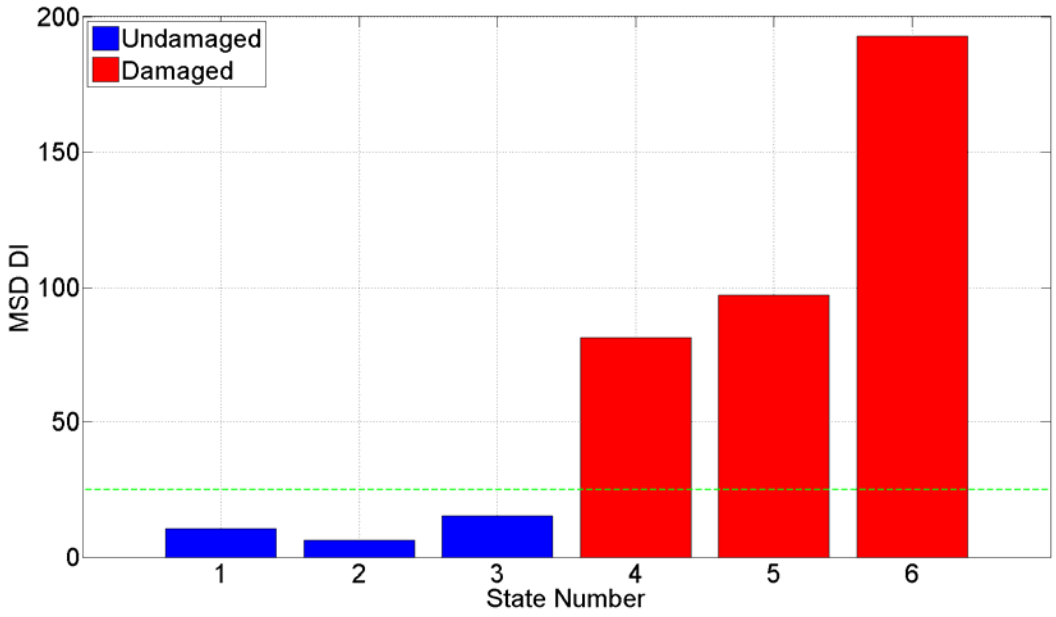

Figure 6.21 MSD using training data from State 1 to 3 in Case 2 of Test 1 (sensor 6)

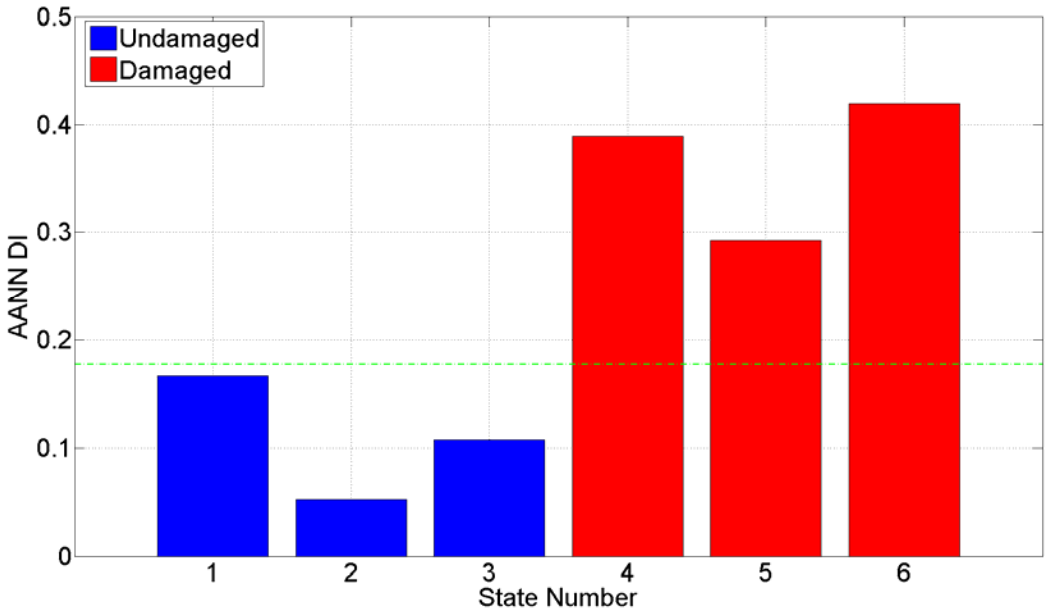

Figure 6.22 AANN using training data from State 1 to 3 in Case 2 of Test 1 (sensor 6)

In Case 3 of Test 1, real world damage detection procedure in presence of uncertainties was simulated. First 30 data sets from each undamaged condition (State 1 to 3) were used as training data (total 90 data sets). The relationship of the training data would be learned by the machine learning algorithms. If new data was obtained and fed into the machine learning algorithms, it would be classified as outlier or potential damage if the *DI* value was greater than the threshold value which was based on 95% confidence of interval, otherwise, it would be classified as undamaged condition if the *DI* value was less than the threshold value. The first group test data were made up of rest 20 data sets from each undamaged condition from State 1 to 3 (total 60 data sets). All the data sets from damaged conditions (State 4 to 6) were the second group test data which had total number of 150 data sets. Figure 6.23 and Figure 6.24 plots the *DIs* derived from the MSD algorithm and the AANN algorithm for all the data sets in Test 1, respectively. The 90 data sets of the training data are plotted in the first 90 observations. Following the training data, the first group of test data are plotted from observation 91 to 150 as Test data 1. Then the second group of test data are plotted from observation 151 to 300 as Test data 2. The control line separates undamaged conditions (below green line) from damaged conditions (above green line). From

both figures, even some outliers are observed in Test data 1, most data are classified as undamaged condition which matches the description in Table 6.2. In Test data 2, if real damage was presented in the structure, the machine learning algorithm were able to classify the test data as damaged condition even the effect from uncertainties were presented in the times series data. This damage procedure indicated that, in real world damage detection, if new data were fed into the machine learning algorithm, identified outlier would go away and the data would go back to undamaged condition if there was no damage in the structure. However, if there was damage in the structure, the identified outlier would not go away, and the data would stay in damaged condition.

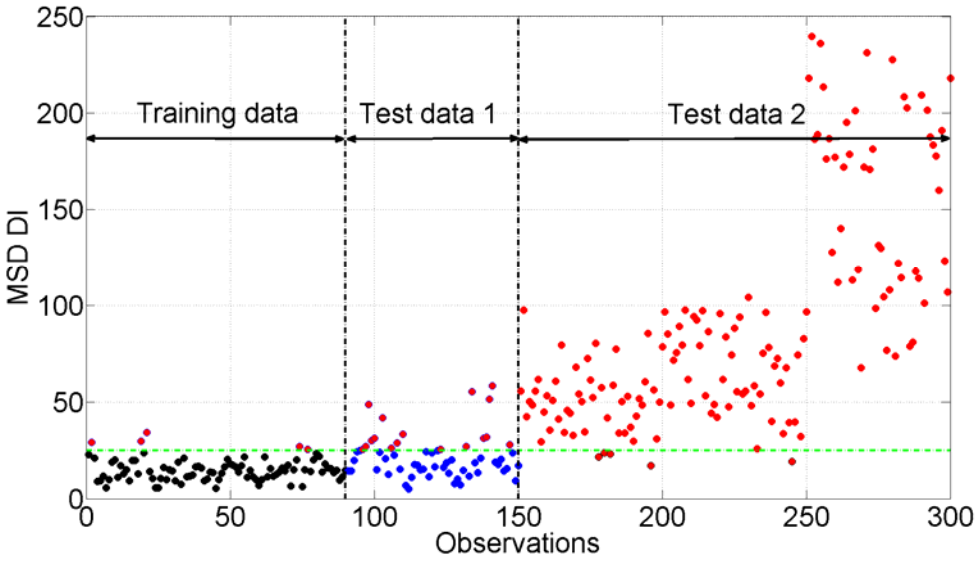

Figure 6.23 Damage detection based on MSD algorithm in Test 1

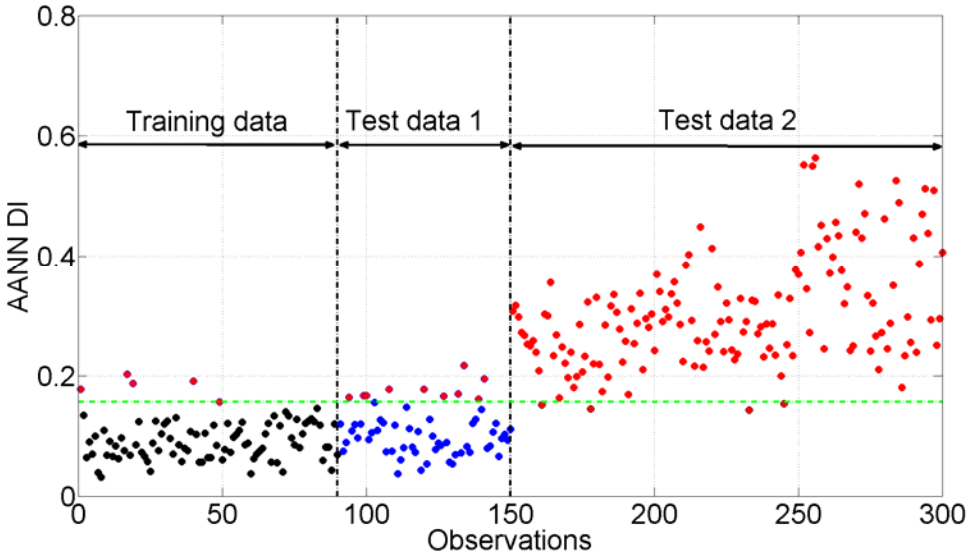

Figure 6.24 Damage detection based on AANN algorithm in Test 1

6.3.5b Results: Test 2

Similar to Test 1, the AR model order needs to be determined first. Figure 6.25 shows the AIC values calculated from sensor 6 of baseline condition in Test 2. Obeserved from the figure, the AIC values converges after AR order 15. Therefore, AR(15) model was used to extract feature vectors from all the time series data in Test 2. The goodness-of-fit of the AR(15) model can be seen in Figure 6.26, and Figure 6.27.

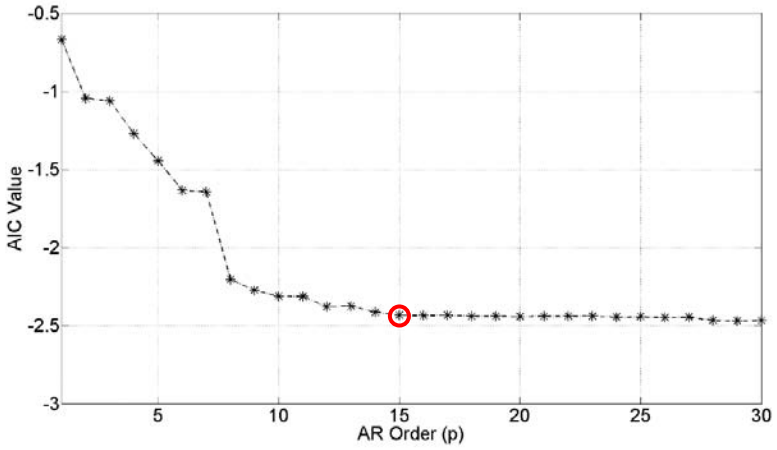

Figure 6.25 AIC values of AR model order in Test 2 (sensor 6 of State 1)

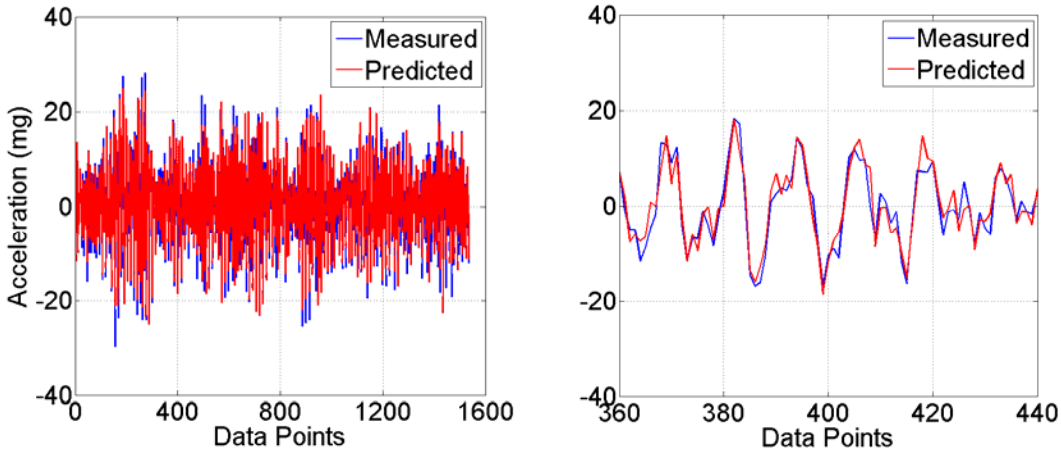

Figure 6.26 Comparison of the measured and predicted time history data using AR(15) model (sensor 6 of State 1 in Test 2)

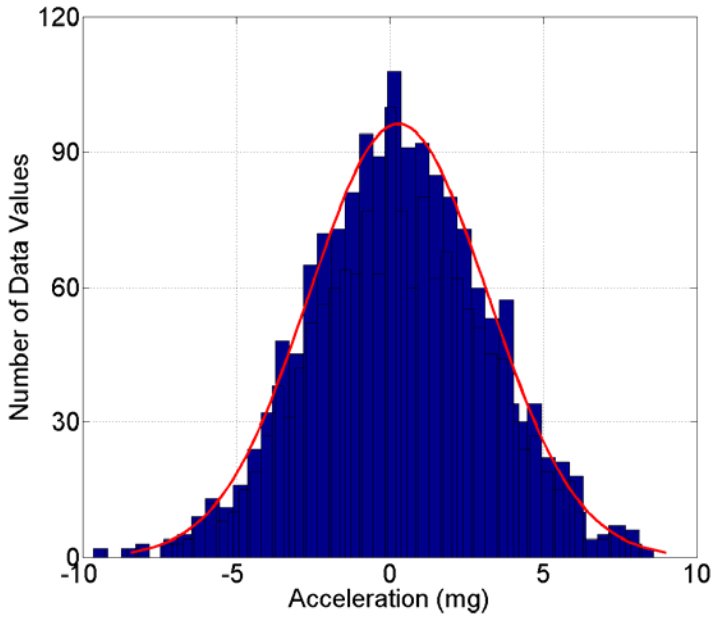

Figure 6.27 AR(15) residual errors histogram with Gaussian distribution (sensor 6 of State 1 in Test 2)

In Test 2, three cases (Case 1, Case 2, and Case 3) were also analyzed. Case 1 and Case 2 were trained with different training data. Case 3 showed real world damage detection situation by using

machine learning algorithms. In all the cases, the threshold value for both of the MSD and AANN algorithms were based on 95% confidence of interval. The AANN architecture was the same in Test 1.

In Case 1 of Test 2, training data were made up of 147 data sets from each 49 sets from State 1 to 3, while the test data were made up of one time series data set from each state condition from State 1 to 12. As a consequence, the feature vector matrix of training data in Case 1 was 15 × 147 (15 AR coefficients, and 147 data sets), the feature vector matrix of test data was 15 × 12. Figure 6.28 and Figure 6.29 present the damage detection results based on the MSD algorithm and the AANN algorithm, respectively. In the two figures, the green dash line is also the control line based on the threshold value, *DI* value over the control line is classified as damage condition, while undamaged condition is below the control line. Both algorithms can classify State 7 to 12 as damaged condition, however, they also classify State 4 to State 6 as damaged condition which are supposed to be undamaged condition shown in Table 6.3. It means that by training the two machine learning algorithms with only data from State 1 to 3 in presence some of operational variability (undamaged condition), the machine learning algorithms were not able to separate all operational effect from real damage.

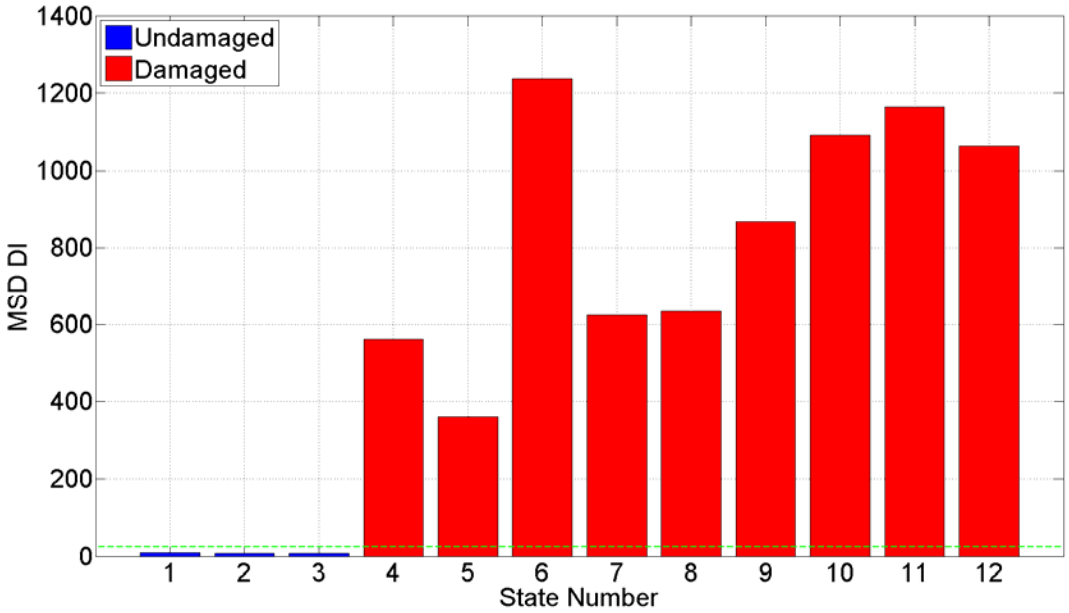

Figure 6.28 MSD using training data from State 1 to 3 in Case 1 of Test 2 (sensor 6)

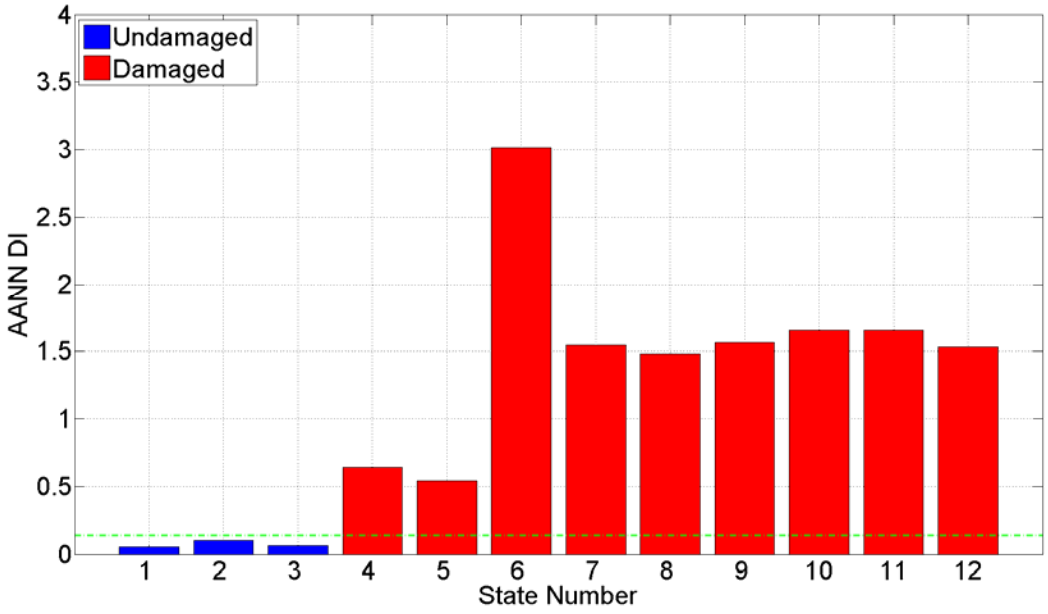

Figure 6.29 AANN using training data from State 1 to 3 in Case 1 of Test 2 (sensor 6)

In Case 2 of Test 2, training data were made up of 294 data sets with each 49 sets from State 1 to 6, while the test data were the same in Case 1 with one time series data set from each state condition from State 1 to 12. As a consequence, the feature vector matrix of training data in Case 2 was 15 × 294 (15 AR coefficients, and 294 data sets), the feature vector matrix of test data was 15 × 12. Figure 6.30 and Figure 6.31 present the damage detection results based on the MSD algorithm and the AANN algorithm, respectively. In the two figures, both algorithms can classify State 7 to 12 as damaged condition, and they classify State 2 to State 5 as undamaged condition which matches the description in Table 6.3. It means that by training the two machine learning algorithms with all undamaged conditions in presence of all assumed operational effect from State 1 to 6, the machine learning algorithms were able to separate all operational effect from real damage.

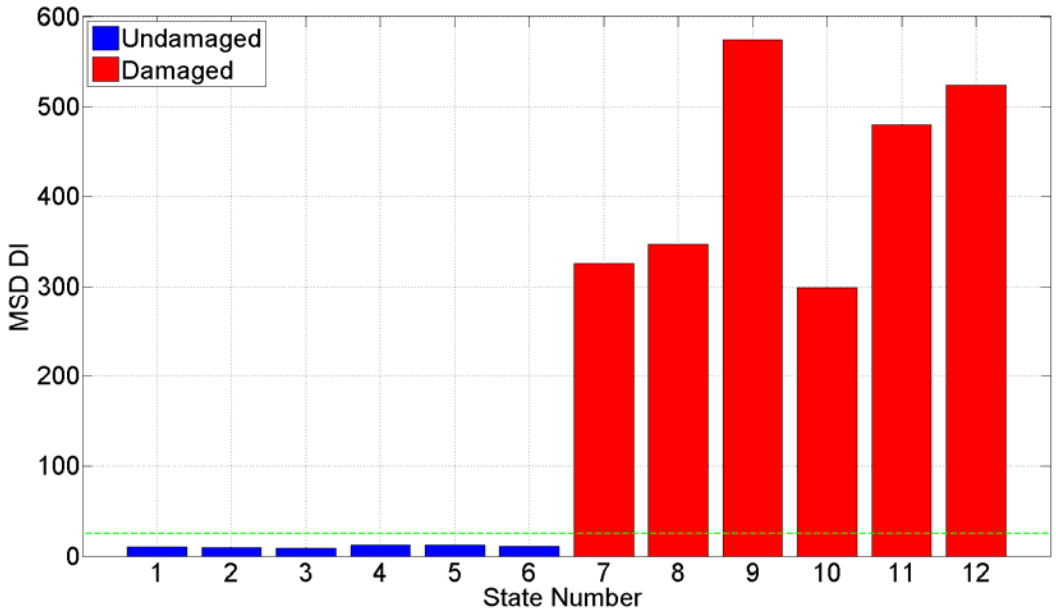

Figure 6.30 MSD using training data from State 1 to 6 in Case 2 of Test 2 (sensor 6)

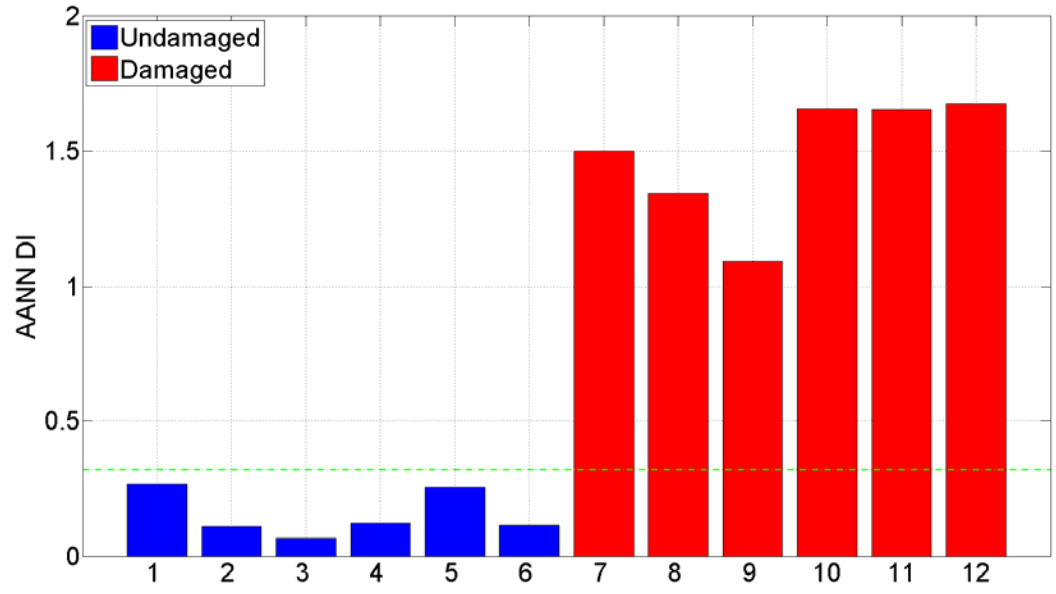

Figure 6.31 AANN using training data from State 1 to 6 in Case 2 of Test 2 (sensor 6)

Similar to Case 3 of Test 1, in Case 3 of Test 2, real world damage detection procedure in presence of uncertainties was simulated. First 30 data sets from each undamaged condition (State 1 to 6) were used

as training data (total 180 data sets). The threshold value which was also based on 95% confidence of interval. The first group test data were made up of rest 20 data sets from each undamaged condition from State 1 to 6 (total 120 data sets). All the data sets from damaged conditions (State 7 to 12) were the second group test data which had total number of 30 data sets. Figure 6.32 and Figure 6.33 plot the *DIs* derived from the MSD algorithm and the AANN algorithm for all the data sets in Test 2, respectively. The 180 data sets of the training data are plotted in the first 180 observations. Following the training data, the first group of test data are plotted from observation 181 to 300 as Test data 1. Then the second group of test data are plotted from observation 301 to 600 as Test data 2. The control line separates undamaged conditions (below green line) from damaged conditions (above green line). From both figures, even some outliers are observed in Test data 1, most data are classified as undamaged condition which matches the description in Table 6.3. In Test data 2, if real damage was presented in the structure, the machine learning algorithm were able to classify the test data as damaged condition even the effect from uncertainties were presented. This damage procedure also indicated that, in real world damage detection, if new data were fed into the machine learning algorithm, identified outlier would go away and the data would go back to undamaged condition if there was no damage in the structure. However, the identified outlier would not go away, and the data would stay in damaged condition if there was damage in the structure.

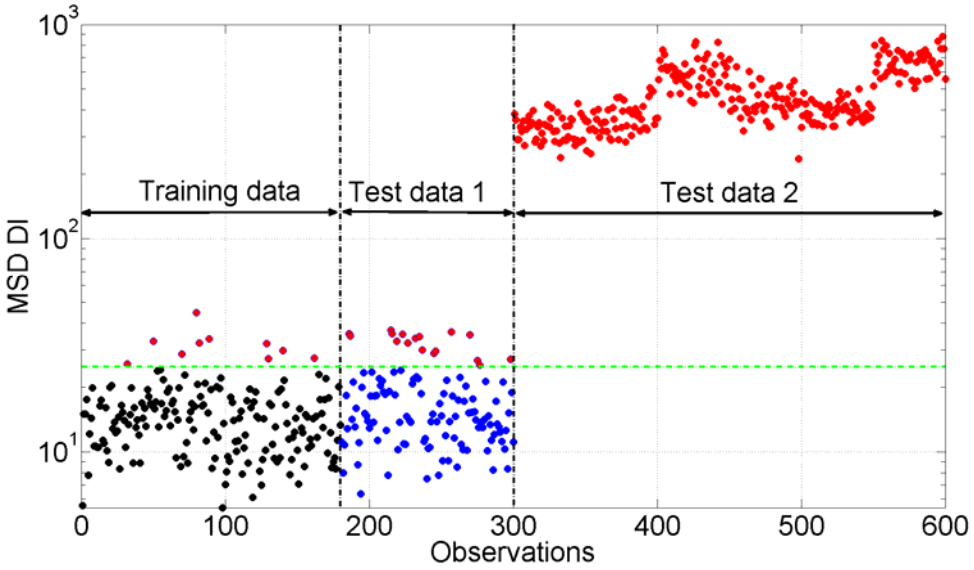

Figure 6.32 Damage detection based on MSD algorithm in Test 2

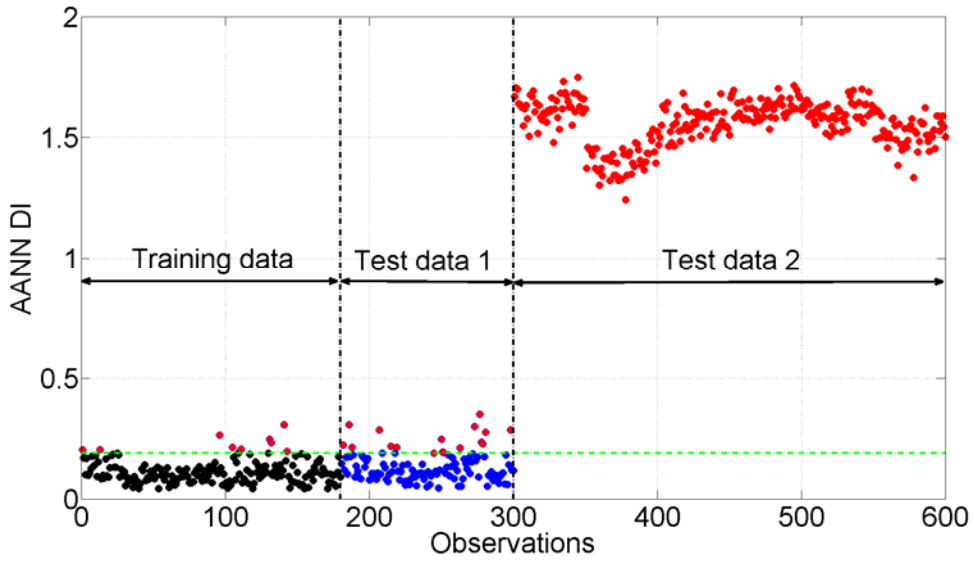

Figure 6.33 Damage detection based on AANN algorithm in Test 2

6.3.6 Observations from the results

From Test 1 and Test 2, the MSD and AANN machine learning algorithms were shown to effectively differentiate the undamaged and damaged state conditions if all the operational and environmental

conditions were included in the training data. The advantage of machine learning algorithm for damage detection is that the identification procedure doesn't use any direct measurement of the operational and environmental variability, their effects are included in the time series data. By learning the correlation of the feature vectors extracted from the time series data, the machine learning algorithms are able to detect the outlier which shows abnormal condition. However, the limitation is if a new data set obtained under an operational or environmental condition is no included in the training data, there is no guarantee that the state condition will be properly classified. Therefore, in real world practice, learning more state conditions under different operational and environmental effects is critical to the performance of the MSD and AANN machine learning algorithms. In addition, design the neural network architecture in terms of number of codes in mapping and bottleneck layers is critical to the performance of the AANN algorithm.

In order to quantify the damage detection performance of the MSN and AANN algorithm for a given threshold, type I and type II errors are employed herein. They are a common way of reporting the performance of a binary classification. In statistics, a type I error is the incorrect rejection of a true null hypothesis (false-positive indication of damage), while a type II error is the failure to reject a false null hypothesis (false-negative indication of damage). A null hypothesis is a statement that the thing being studied produces no effect or make no difference. In the context of damage detection, the null hypothesis is the statement "there is no damage in the structure", then type I error is incorrect to classify the data as damaged condition when the data is in undamaged condition, while type II error is failure to classify the data as damaged condition when the data is in damaged condition. Table 6.4 summarizes the number of type I and type II errors for both of the MSN and AANN algorithm in Case 3 of Test 1 and Case 3 of Test 2. In general, the AANN algorithm shows better performance than the MSD algorithm. The number of type I, type II and total errors in the AANN algorithms are all less than those in the MSD algorithm in both cases. This is expected since the AANN algorithm can learn the nonlinear relationship among the feature vectors, while the MSD is linear based. Secondly, both algorithms have better performance to avoid false indications of damage (less type II errors than type I errors). However, with the type II errors are all less 5%, both algorithms show reliability to detect damage. Regarding to the type I error which is

incorrect to classify the data as damage when the data is in undamaged condition, from previous study, it can be reduced by including more training data with operational and environmental variability are present. In addition, if the confidence of interval increases, then the threshold value in the MSD and AANN algorithm will also increase, then the type I error can be reduced as well.

Table 6.4 Number of type I and type II errors for each algorithm

Case No.	Algorithm	Error		
		Type I	Type II	Total
Case 3 in Test 1	MSD	17 (28.3%)	5 (3.3%)	22 (10.5%)
	AANN	10 (16.7%)	4 (2.7%)	14 (6.7%)
Case 3 in Test 2	MSD	17 (14.2%)	0 (0%)	17 (4.1%)
	AANN	15 (12.5%)	0 (0%)	15 (3.6%)

Another important observation from Figure 6.24, Figure 6.25, Figure 6.33, and Figure 6.34 can be found. In the case of damage detection, after setting up the training data sets and learned by the machine learning algorithms, if an outlier (potential damage) was presented, immediate decision regarding to it was a damage or not could not be made, some more data should be observed following the outlier. If the following data went back to normal condition, most likely, the previous outlier was a type I error, and it was caused by the fact that this data obtained from the presence of operational and environmental variability was not included in the training data sets. By including this condition into the training data, the data from similar operational and environmental condition will not be classified as outlier in future. This can be observed from the first group of test data sets in all the cases. However, if the following data stayed at the abnormal condition position for the rest of data sets, most likely, the previous outlier as long as the new outliers are real damage. This observation can also be found from the second group of test data sets in all cases. This observation can help us understand the performance of damage detection based on machine learning algorithms for real-world structures.

6.4 Application of Machine Learning Algorithms for Damage Detection on the Meriden Bridge

6.4.1 The Meriden Bridge

The Meriden Bridge discussed in Chapter 5 is employed as the test bed bridge in this study. Detail description of the bridge can be found in previous chapter. A long-term wired monitoring system was installed on the Meriden Bridge. Almost one-year monitoring data from March 2013 to March 2014 were investigated. Every hour, seven accelerometers captured the vibration of the bridge for five minutes with sampling rate of 2048Hz. In addition, environmental quantities such as temperature at three different locations were measured from an array of RTDs. Since real-time monitoring data was captured by the accelerometers, operational and environmental effects were included in the data. The recording system was down occasionally due to power outage, so the data were not recorded continuously every day. A total of 4177 data sets are available which consists 47.7% of the total 8760 data sets in one year. Note that the long-term monitoring system is still running, which permits one to validate the SHM system for damage detection with more data sets in future.

6.4.2 Test results and analysis

The procedure for implementing machine learning algorithms for damage detection has been developed and tested in previous section. The steps include: first, obtain time series vibration data from the monitoring structure under operational and environmental condition; second, extract damage-sensitive feature vectors from time series data and train the machine learning algorithm; third, transform each input feature vector into global *DI* based on different algorithms.; four, setup threshold for certain level of significance; five, detect outlier of damage based on the training data in step three and threshold value in step four. Note that in step two, different damage-sensitive feature vectors can be used based on different scenarios. In the experimental test, AR model coefficients were use as damage-sensitive feature vectors. That's because each data set was small, small number of AR model order were good enough to predict the whole time-series data. In addition, for the data set in each station condition, they were captured under similar condition, AR model with the same order number was suitable for all the data sets. However, using AR model coefficients as damage-sensitive feature vectors for the Meriden Bridge monitoring data are difficult. Each data set from the Meriden Bridge (5 mins with 2048 Hz sampling rate) is much larger

than the data set in the test study (6 secs with 256 Hz sampling rate), that means larger number of AR model order are desired to guarantee better data fit. With many uncertainties included in the time series data, different AR model orders were determined from different data sets. However, different AR model orders make it not available to be learned by the machine learning algorithms (number of feature vectors should be the same for all the data sets). Therefore, natural frequencies identified from the Meriden Bridge were used as the damage-sensitive feature vectors.

From previous study, seven natural frequencies from one-year monitoring data have been identified using the FDD algorithm from seven accelerometers, they should be accurate for capturing bridge condition at different time. A total number of 4045 observations estimated hourly from March 15th 2013 to January 19th 2014 are plotted in Figure 6.35 (temperature), and Figure 6.36 (identified seven natural frequencies). Note that, 132 data sets observed after January 19th was not used in this section. That's because couple of days' monitoring data were not available between the first 4045 observations and last 132 data sets. Extreme temperature from the last 132 data sets caused the bridge in extreme condition. Without previous data as learning data, they were not data test to be used as test data.

In order to test the feasibility of machine learning algorithms on damage detection for the Meriden Bridge, training data were determined to be the first 3703 observations which included natural frequencies identified from the highest temperature to the lowest temperature. It means that the natural frequencies from March 15th 2013 to January 4th 2014 were used as training data. The rest 342 observations from January 5th 2014 to January 19st 2014 were used as test data. Since no damage was introduced into the Meriden Bridge, all the data sets were assumed to be obtained from undamaged condition with the presence of operational and environmental variability. The temperature variation for data sets from training phase and test phase is shown in Figure 6.34, while all the seven natural frequencies used as training data and test data are presented in Figure 6.35. Note that the temperature and natural frequencies are plotted in concatenated format, which does not include the existence of gaps between data sets that were caused by interruption of the power supply.

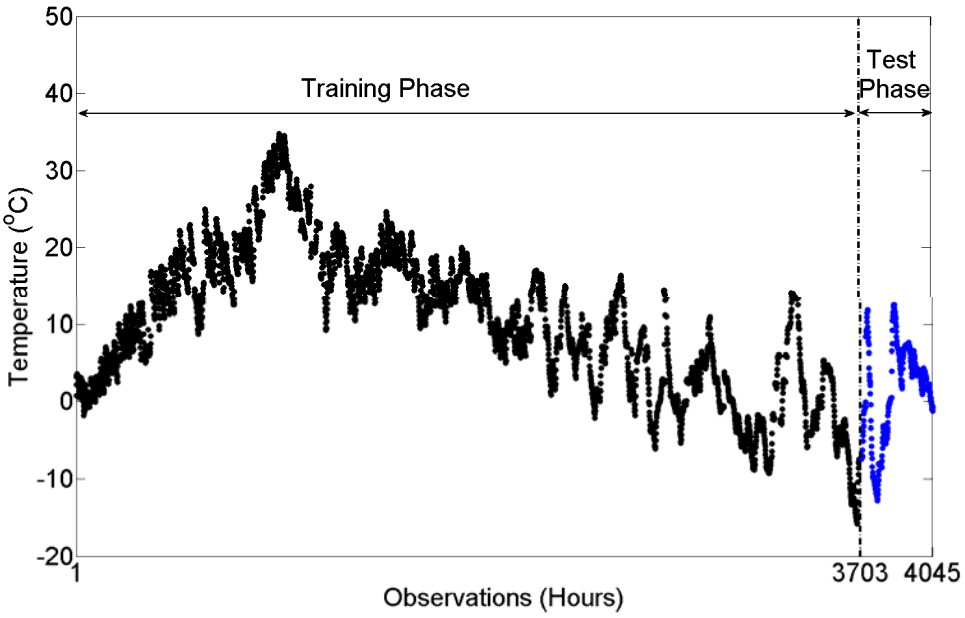

Figure 6.34 Temperature variation of the Meriden Bridge for training phase and test phase

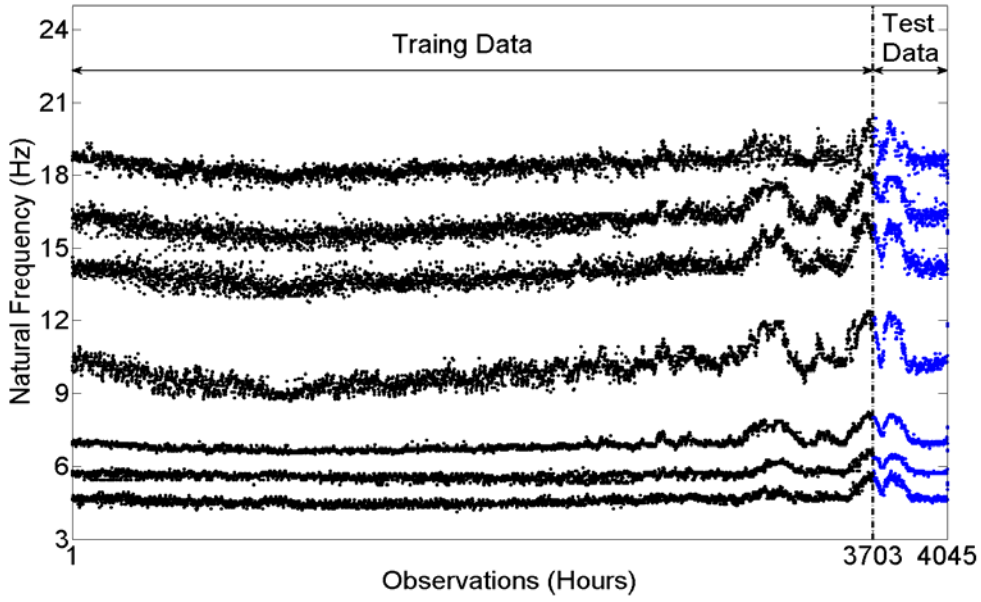

Figure 6.35 Natural frequencies of the Meriden Bridge as training data and test data

The MSD and AANN presented in previous section were implemented in an unsupervised learning mode where no information about the presence of damage was provided during the training phase. In training phase, underlying distribution of the damage-sensitive feature vectors and dependency of all the undamaged conditions under operational and environmental variability were learned by each algorithm. In the test phase, since test data sets were composed from assumed undamaged condition, the algorithms were expected not to detect damage. However, due to lack of training data from all the undamaged condition with the presence of operational and environmental variability, outliers were expected based on different algorithms. Since the MSD is a linear algorithm, while the AANN is a nonlinear algorithm, in the presence of nonlinear correlation between variables, the AANN algorithm should present greater accuracy than the MSD. The AANN algorithm is built up with a feedforward neural network with three layers: mapping layer, bottleneck layer, and de-mapping layer. Several trainings with different initial conditions were performed to increase the probability that the global minimum was achieved. Therefore, the network for the Meriden Bridge data has two nodes in bottleneck layer (represent changes of mass and stiffness), and seven nodes in mapping and de-mapping layer (no significant changes were observed with higher number of nodes). A confidence interval of 95% was used in both algorithms.

Figure 6.36 and Figure 6.37 show the results from the MSD and AANN algorithm, respectively. In both figures, the green dash line is a control line based on the threshold calculated from different algorithms. Black dots are baseline conditions from training phase, blue dots are from test phase. Since they are all below the green dash control line, they are classified as undamaged condition. In contrary, the red dots above the control line are all outliers. Several observations from the two figures can be found:

1) The MSD algorithm is not able to remove the nonlinear patterns from the data sets caused by extreme cold temperatures (below freezing point). It is indicated by the concentration of outliers in the period of extreme cold temperatures during both of the training phase and test phase. On the other hand, no concentration of the outliers are found from the AANN algorithm;

2) Both algorithms are modelling well the baseline condition in the training phase without extreme cold temperatures when the variables show nearly linear pattern;

3) More outliers are detected at the beginning of test phase in both algorithms. This can be explained that since the state conditions of the Meriden Bridge from the extreme cold temperature are not fully learned by the machine learning algorithms from training phase, they are not capable to classify them as undamaged condition;

4) However, in test phase, when the temperature increases above freezing point, the state condition of the Meriden Bridge goes back to normal. Note that all the *DIs* were derived from the time history data from the accelerometers in the presence of operational and environmental variability. It indicates that most likely, there is no damage in the Meriden Bridge. If there was damage in the Meriden Bridge, the *DIs* in the test phase should be continuously classified as outliers, and didn't go back to normal condition. As discussed in previous section, if more data sets from extreme cold temperature were learned in the training phase, the number of outliers caused by the presence of operational and environmental variability in test phase would decrease.

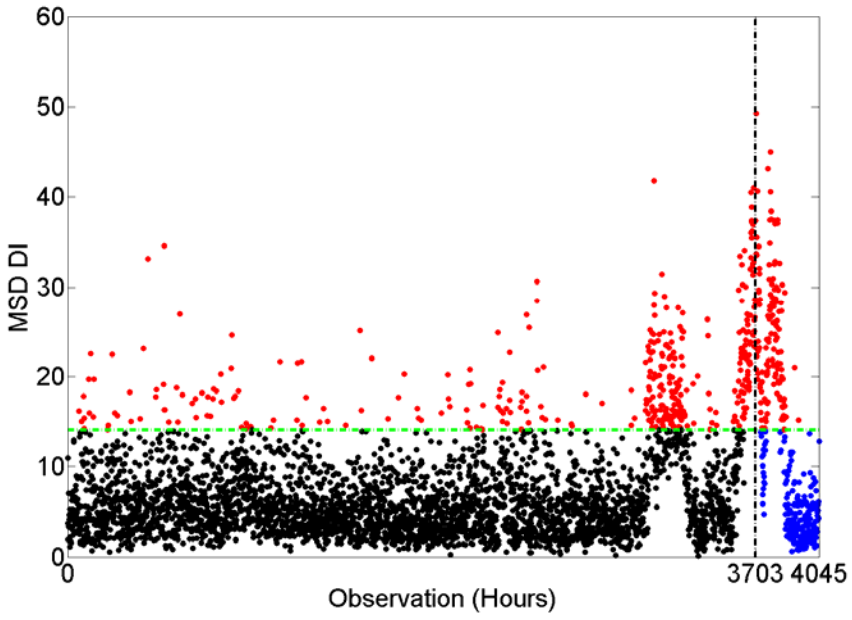

Figure 6.36 Damage detection for the Meriden Bridge based on MSN algorithm

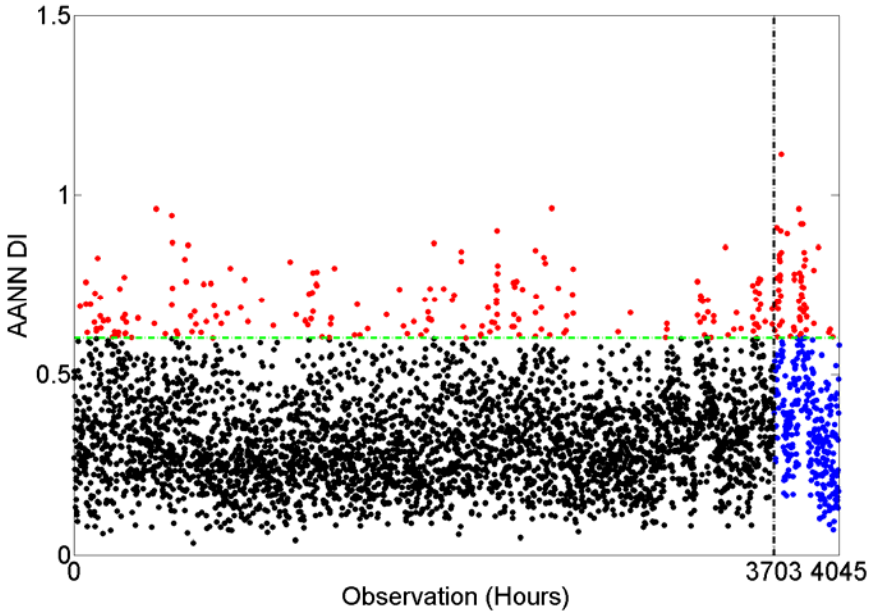

Figure 6.37 Damage detection for the Meriden Bridge based on AANN algorithm

Table 6.5 summarizes the number of type I and type II errors for both of the MSN and AANN algorithm in damage detection using feature vectors from the Meriden Bridge. Note that since no damage was introduced to the Meriden Bridge, the bridge was assumed to be undamaged, the type II error was not tested. Type I error in the test phase shows the false-positive error by classifying the undamaged condition as outliers. In the case of the MSN algorithm, relatively high percentage of type I error (40.4%), along with the concentration of outliers during the period with extreme cold temperatures indicates relatively poor classification performance. In fact, the MSD algorithm is based on the assumption that baseline data sets are multivariate Gaussian distributed. However, when nonlinearities are present in the observations such as the identified natural frequencies from the Meriden Bridge, this assumption might not be appropriate. On the other hand, as the AANN algorithm is able to learn the nonlinear relationship between variables, relatively low type I error indicate higher classification performance compared to the MSN algorithm. It can be concluded that the AANN algorithm might be more appropriate for long-term monitoring than the MSD algorithm.

Table 6.5 Number of type I and type II errors for each algorithm from the Meriden Bridge data

Algorithm	Error		
	Type I	Type II	Total
MSD	138 (40.4%)	N/A	138 (40.4%)
AANN	57 (14.9%)	N/A	57 (14.9%)

6.5 Discussion and Summary

As shown in this chapter, the feasibility of the MSN and AANN machine learning algorithms has been tested on a laboratory-scale truss bridge and a full-scale in-service highway bridge. First, the concept of the MSN and AANN algorithms were descried. The MSN is a linear algorithm based on the assumption that the feature vectors used as training data are Gaussian distributed, while the AANN is a nonlinear algorithm with a feedforward neural network to perform the mapping and de-mapping, where the network outputs are the reproduction of the network inputs.

In the lab test, system identification of the 12-bay truss bridge was first performed. Then the two algorithms were used to analyze vibration data from the truss bridge with two different tests. In Test 1, six station conditions were tested with first three as normal conditions assumed to be undamaged. Two different mass were added at the same location to assume two different environmental variability. A loose bolt between a truss element and steel bracket was introduced to assume real damage. The last three state conditions were damaged conditions in the presence of environmental variability. In Test 2, twelve state conditions were tested with first six as normal conditions assumed to be undamaged. The same mass was added at five different locations of the truss to assume five operational variability. The last six state conditions were assumed to be damaged with the loose bolt introduced into the truss bridge in the presence of operational variability. In both tests, AR model coefficients were used as damage-sensitive feature vectors. By training the algorithms with feature vectors from normal conditions in the presence of operational and environmental variability, the MSN and AANN algorithms were able to differentiate undamaged and damaged condition. However, the performance of the algorithms based on how many

state conditions with different operational and environmental variability were included in the training phase. In addition, the AANN showed better classification performance with lower number of false alarms compared to the MSN algorithm. Furthermore, if damage was existed in the structure, the *DIs* derived from both algorithms were continuously classified as outliers, and didn't return back to normal condition.

In the full-scale bridge test, seven identified natural frequencies from almost one-year monitoring data in presence of operational and environmental variability were used as damage-sensitive feature vectors. A total number of 4045 observations were used with first 3703 observations to be training data, and rest 342 to be test data. The training data were obtained from March 15th 2013 to January 4th 2014, which included data from the highest temperature to the lowest temperature during monitoring period, while the test data were from January 5th to January 19th 2014. The analysis of the result has shown that the MSD algorithm yielded relatively poor classification performance in terms of high number of false alarms and concentration of outliers since it was not able to remove the nonlinearity pattern present in the feature vectors. On the other hand, the nonlinear algorithm AANN had lower number of false alarm and no concentration of outliers which indicate it was able to remove nonlinearity pattern in feature vectors. It also concluded that the AANN algorithm was more appropriate for long-term monitoring. In addition, more outliers were classified at the beginning of training phase with extreme cold temperature present, when the temperature increased back to normal condition, the *DIs* derived from the both algorithms went back to normal condition which indicated that the outliers were not real damage rather than caused by not enough state condition in presence of operational and environmental variability were learned by the machine learning algorithms. By learning more state conditions from extreme operational and environmental variability, the number of false alarms could be reduced.

CHAPTER 7 CONCLUSIONS AND FUTURE WORK

7.1 Conclusions

The research presented in this dissertation provided a comprehensive framework for long-term SHM of full-scale bridge structures with uncertainties.

An inclusive literature review on SHM, and full-scale bridge monitoring applications with traditional wired monitoring system and WSSN has been provided, which indicates a potential of implementing WSSs on more SHM practices in terms of bridge condition assessment at a lower cost and higher density. In addition, extensive background on WSS technology, vibration-based energy harvesting, vibration-based SHM algorithms, data normalization and machine learning algorithms has served as a motivation and foundation of this dissertation.

While much of the WSS technology has been available for nearly a decade, there have been limited number of full-scale implementations due to its intrinsic limitations such as power supply. To overcome the power supply issue, power consumption of the Imote2 wireless platform with the SHM-A sensor board was firstly evaluated under different power consumption modes. Then, a wide-band vibration-based piezoelectric energy harvester were developed and validated from the lab test. An piezoelectric array of six pieces of piezoelectric cantilever beams with proof mass were tested in the lab, the experimental results matched well with the numerical model, and showed much robust performance compared to single piece of piezoelectric energy harvester. Furthermore, based on the power consumption the by Imote2, a wide-band piezoelectric array with larger size piezoelectric beam was designed to supply enough power for the Imote2. Effectively, this study presents a potential application of vibration-based energy harvesting system on supplying reliable power for WSSs.

Full-scale bridge health monitoring has been performed by installing WSSN and wired system on the Meriden Bridge. The WSSN included five Imote2 wireless sensors as leaf nodes and one Imote2 as gateway node. The bridge dynamic responses were captured by the five Imote2 sensors from white noise excitation. While the wired monitoring system included a total number of 38 sensors with different types.

The FDD algorithm was employed for extracting features from the monitoring data in terms of natural frequencies, and mode shapes. The analysis results from the WSSN were compared with the results from wired piezoelectric accelerometers and a FE model in SAP2000. By comparing identification results from WSSN, wired monitoring system and FE model, robust results have been found. The result of this work has enhanced the knowledge of applying WSSs on bridge health monitoring.

One-year monitoring data from the Meriden Bridge has been analyzed to understand the temperature effects on bridge natural frequencies. Temperature fluctuation was observed from the monitoring data which caused the variation of the identified seven natural frequencies of the Meriden Bridge. Significant changes of the natural frequencies were found when the temperature was below freezing point. Linear and nonlinear regression models have been employed to quantify the temperature effects on natural frequencies. The study provides a deep understanding how bridge modal properties are effected by environmental variability.

Due to the operational and environmental variability, it is very challenging to transit damage detection from lab tests to real world structures. Sometimes the changes of structural modal properties from operational and environmental variability can mask the changes from real damage, which makes false alarms on bridge condition assessment. In order to overcome this problem, a damage detection procedure based on machine learning algorithms has been developed and validated through a lab experimental test. A linear algorithm based on the MSD and a nonlinear algorithm based on the AANN have been employed in this study. The experimental test was performed on the 12-bay truss bridge with simulated undamaged and damaged condition in the presence of assumed operational and environmental variability. Test results showed that the classification performance of these two machine learning algorithms were based on the distribution of training feature vectors. With large enough distribution of the feature vectors in the training phase, both algorithms showed robust performance to differentiate damaged condition from undamaged condition in the presence of operational and environmental variability. The MSD showed worse classification performance compared to the AANN algorithm since it was not able to

learn nonlinear relationship between training feature vectors. In addition, the performance of the AANN algorithm depended on the architecture of the neural network.

With the experience of applying machine learning algorithms on damage detection from the experimental test, they were implemented to analyze the one-year monitoring data from the Meriden Bridge. The identified natural frequencies of the Meriden Bridge were slit into training data sets, and test data sets. The training data sets included natural frequencies obtained from the highest temperature to lowest temperature to guarantee large distribution of the feature vectors. The test data were composed of the rest data sets after training test data. Since no damage was introduced into the Meriden Bridge, the analysis results from the machine learning algorithms confirmed this assumption with the observation that most of the *DIs* were classified as undamaged condition. Since nonlinearity was present in the natural frequencies due to extreme cold temperature, the MSD showed relatively poor performance than the AANN algorithm, which indicates that the AANN algorithm is more appropriate to be implemented on long-term bridge health monitoring in terms of damage detection.

In conclusion, this research provided a comprehensive contribution to long-term SHM of bridge structures under uncertainties including vibration-based energy harvesting system, full-scale condition assessment by using WSSs, long-term temperature effects on bridge modal properties, and full-scale implementation of machine learning algorithm based damage detection procedure.

7.2 Future Work

While a comprehensive contribution has been made by the research in this study, future studies are suggested to extend the developed framework to be applicable for various full scale civil structures in a long-term manner.

One of the biggest challenges for implementing WSSN on long-term SHM is how to supply continuously and reliable power to the WSSs. A wide-band vibration based piezoelectric energy harvester has been developed and tested in the lab. However, the feasibility of the energy harvester devices in full-scale application was not tested in this study due to limited resources. A wide-band piezoelectric energy

harvester device for target excitation frequency range with large size for high power generation could be tested based on the framework developed in this dissertation. In addition, other energy harvesting device can also be explored on target infrastructure and environment in order to provide reliable energy harvesting capability for long-term monitoring of full-scale structures using WSSN.

The effects of temperature on natural frequency have been investigated on nearly one-year monitoring data from the Meriden Bridge. Since the long-term monitoring system is still on the Meriden Bridge, multi-year trend of temperature and natural frequency could be obtained in future.

Damage detection procedure based on machine learning algorithms has been developed in this study. Its feasibility has been validated in the experimental test with simulated damage in the presence of operational and environmental variability. However, how to introduce damage into the real world in-service structure is very challenging due to safety issues. Due to limited resource and time, damaged condition was not introduced into the Meriden Bridge. In addition, due to limited monitoring data sets, the bridge state conditions under extreme cold temperature were not fully learned by the machine learning algorithms. Therefore, continuous monitoring of the Meriden Bridge is desired, and more data sets could be used as training data by the machine learning algorithms. In addition, damage could also be introduced into to the Meriden Bridge by adding a dump truck on the bridge or clamping stiffness plate under the steel girder. By doing this, much more robust results of the machine learning algorithm on damage detection for real world structures with uncertainties could be achieved.

REFERENCES

[1] Abdel-Ghaffar, A.M., and Scanlan, R.H. (1985). "Ambient Vibration Studies of Golden Gate Bridge: I. Suspended Structure." *Journal of Engineering Mechanics*, 111(4), 463-482.

[2] Abdelkefi, A., Haji, M.R>, and Nayfeh, A.H. (2013). "Piezoelectric Energy Harvesting from Transverse Galloping of Bluff Bodies." *Smart Materials and Structures*, 22(1), 015014.

[3] Abe, M., Fujino, Y., Yanagihara, M. and Sato, M. (2000). "Monitoring of Hacucho Suspension Bridge by Ambient Vibration Measurement." *Nondestructive Evaluation of Highway, SPIE Proceedings*, 3995:237-244.

[4] Ajitsaria, J., Choe, S.Y., Shen, D., and Kim, D.J. (2007). "Modeling and Analysis of a Bimorph Piezoelectric Cantilever Beam for Voltage Generation." *Smart Materials and Structure*, 16, 447-454.

[5] Anton, S.R. and Sodano, H.A. (2007). "A Review of Power Harvesting using Piezoelectric Materials (2003-2006)." *Smart Materials and Structures*, 16, 1-21.

[6] ASCE Report Card for America's Infrastructure (2013). www.asce.org.

[7] Azarbayejani, M., Jalalpour, M., EI-Osery, A.I., and Taha, M.M.R. (2011). "Field Application of Smart SHM using Field Programmable Gate Array Technology to Monitor an RA Bridge in New Mexico." *Smart Materials and Structures*, 20, 085005.

[8] Beeby, S.P., Tudor, M.J., and White, N.M. (2006). "Energy Harvesting Vibration Sources for Microsystems Application." *Measurement Science and Technology*, 17, 175-195.

[9] Bernal, D. (2002). "Load Vectors for Damage Localization." *Journal of Engineering Mechanics*, ASCE, 0733-9399, 128(1):7-14.

[10] Brincker, R., Zhang, L., Andersen, P. (2001). "Modal Identification of Output-only Systems using Frequency Domain Decomposition." *Smart Materials and Structure*, 10, 441-445.

[11] Brownjohn, J.M.W. (2007). "Structural Health Monitoring of Civil Infrastructure." *Philosophical Transaction of the Royal Society A: Mathematical, Physical and Engineering Sciences*, 365, 589-622.

[12] Caicedo, Jm., Clayton, E., Dyke, S.J., Abe, M., and Tokyo, J. (2002). "Structural Health Monitoring for Large Structures using Ambient Vibration." *Proceeding of the ICANCEER Conference*, Hong Kong, August 15-20.

[13] Carrasco, C.J., Osegueda, R.A., Ferregut, C.M., and Grygier, M. (1997). "Localization and Quantification of Damage in a Space Truss Model Using Modal Strain Energy." *Smart Structures and Material: Smart Systems for Bridge, Structures, and Highways, SPIE*, 3043: 181-192.

[14] Cawley, P. and Adams, R.D. (1979). "The Location of Defects in Structures From Measurement Natural Frequencies." *Journal of Strain Analysis*, 14(2): 49-57.

[15] Celebi, M., and EERI, M. (2006). "Real-Time Seismic Monitoring of the New Cape Girardeau Bridge and Preliminary Analyses of Recorded Data: an Overview." *Earthquake Spectra*, 22, 609.

[16] Chan, T.H.T., Yu, L., Tan, H.Y., Ni, Y.Q., Liu, S.Y., Chuang, W.H., and Cheng, L.K. (2006). "Fiber Bragg Grating Sensors for Structural Health Monitoring of Tsing Ma Bridge: Background and Experimental Observation." *Engineering Structures* 28(5), 648-659.

[17] Cherkassky, V. and Mulier, F. (1998). "Learning from Data, Concepts, Theory and Methods." *Wiley Interscience*.

[18] Cho., S., Jo, J., Jang, S.A., Park, J., Jung, H.J., Yun, C.B., Spencer, B.F. Jr., Seo, J. (2010). "Structural Health Monitoring of a Cable-Stayed Bridge Using Smart Sensor Technology: Data Analysis." Smart Structures and Systems, 6(5-6), 461-480.

[19] Cook-Chennault, K.A., Thambi, N., and Sastry, A.M. (2008). "Powering MEMS Portable Devices – a Review of Non-Regenerative and Regenerative Power Supply Systems with Emphasis on Piezoelectric Energy Harvesting." *Smart Materials and Structures*, 17, 043001.

[20] Corke, P, Valencia, P., Sikka, P., Wark, T., and Overs, T. (2007). "Long-Duration Solar-Powered Wireless Sensor Networks." *Proceeding of the 4th Workshop on Embeded Network Sensors*.

[21] Cross, E.J., Koo, K.Y., Brownjohn, J.M.W., and Worden, K. "Long-Term Monitoring and Data Analysis of the Tamar Bridge." Mechanical Systems and Signal Processing, 35(1-2), 16-34.

[22] Crossbow Technology, Inc. (2009). "Imote2 Data Sheet." Revision A, PN: 6020-0117-02.

[23] Doebling, S.W. and Farrar, C.R. (1997). "A Statistical Comparison of Impact and Ambient Testing Results from the Alamosa Canyon Bridge." 15th International Modal Analysis Conference, IMAC, 1: 264-270.

[24] Doebling, S.W., Farrar, C.R., and Prime, M.B. (1998). "A Summary Review of Vibration-Based Damage Identification methods." Shock and Vibration Digest, 30(2), 91-105.

[25] duToit, N.E., Wardle, B.L. and Kim, S. (2005) "Design Considerations for MEMS-Scale Piezoelectric Mechanical Vibration Energy Harvesters." *Journal of Integrated Ferroelectric*, 71, 121-160.

[26] Erturk, A and Inman, D.J (2009). "An Experimentally Validated Bimorph Cantilever Model for Piezoelectric Energy Harvesting from Base Excitation." *Smart Materials and Structures*, 18, 025009.

[27] Erturk, A and Inman, D.J. (2008). "Issues in Mathematical Modeling of Piezoelectric Energy Harvesters." *Smart Material and Structure*, 17, 065016.

[28] Erturk, A and Inman., D.J. (2008a). "On Mechanical Modeling of Cantilever Piezoelectric Vibration Energy Harvester." *Journal of Intelligent Material Systems and Structures*, 19, 1311-1325.

[29] Fan, W. (2011). "Vibration-Based Damage Identification Methods: A Review and Comparative Study." *Structural Health Monitoring*, 10(1), 83-111.

[30] Farrar, C.R. (2001). "Historical Overview of Structural Health Monitoring*." Lecture Notes on Structural Health Monitoring Using Statistical Pattern Recognition*, Los Alamos Dynamics, Los Alamos, NM.

[31] Farrar, C.R. and Worden, K. (2007). "An Introduction to Structural Health Monitoring." *Physical and Engineering Sciences*, 365(1851), 303-315.

[32] Farrar, C.R., and Doebling, S.W. (1997). "Variability of Modal Parameters Measured on the Alamosa Canyon Bridge." *SPIE Proceedings*, 257-263.

[33] Farrar, C.R., and Worden, K. (2013). "Structural Health Monitoring: A Machine Learning Perspective." John Wiley & Sons, Ltd.

[34] Farrar, C.R., Cornwell, P.J., Doebling, S.W., and Prime, M.B. (2000) "Structural health monitoring studies of the Alamosa Canyon and I-40 bridges." *Los Alamos National Laboratory Report*: LA-13635-MA.

[35] FHWA (2001). "Reliability of Visual Inspection for Highway Bridges, Volume I: Final Report." U.S. Department Transportation, Federal Highway Administration.

[36] Figueiredo, E., Park, G., Farrar, C.R., Worden, K., and Figueiras, J. (2010) "Machine Learning Algorithms for Damage Detection under Operational and Environmental Variability." *Structural Health Monitoring*, 0(0), 1-14.

[37] Gao, Y., Spencer, B. F. Jr., and Bernal, D. (2004). "Experimental Verification of the Damage Locating Vector Method." *Proceeding of Interfacial Symposium on Smart Structure Technology*, Hawaii.

[38] Glynne-Jones, P., and White, N.M. (2001). "A Self-Powered System: a Review of Energy Sources." *Sensor Review*, 21, 91-97.

[39] Guo, Y., Yan, X. (2014). "The Application of the Structural Health Monitoring System for Long-Span Bridges Based on Multi-Sensor Integration." *WIT Transactions on Engineering Sciences*, 84.

[40] Hagood, N.W., Chuang, W.H., and von Flotow, A. (1990). "Modeling of Piezoelectric Actuator Dynamics for Active Structural Control." *Journal of Intelligent Material Systems and Structures*, 1: 327-354.

[41] Hu, X., Wang, B., and Ji, Han. (2013). "A Wireless Sensor Network-Based Structural Health Monitoring System for Highway Bridges." *Computer-Aided Civil and Infrastructure Engineering*, 28(3), 193-209.

[42] Huth, O., Feltrin, G., Maeck, J., Kilic, N. and Motavalli, M. (2005). "Damage Identification using Modal Data: Experiences on a Prestressed Concrete Bridge." *Journal of Structural Engineering*, ASCE, 131(12):1898–1910.

[43] Ibrahim, S.R. (1977). "Random Decrement Technique for Modal Identification of Structures." *Journal of Spacecraft and Rockets*, 14(11), 696-700.

[44] Ibrahim, S.R., and Milkulcik, E.C. (1976). "The Experimental Determination of Vibration Test Parameters from Time Reponses." *The Shock and Vibration Bulletin*, 46(5), 187-196.

[45] ISHMP (2009). "SHM-A Board Multimetric Imote2 Sensor Board, Datasheet and User's Guide." University of Illinois at Urbana-Champaign, Urbana, IL.

[46] Jang, S. (2010). "Structural Health Monitoring for Bridge Structures Using Wireless Smart Sensors." UIUC ProQuest Dissertation and Theses.

[47] Jang, S., Jo., H., Mechitove, K., Rice, J.A., Sim, S.H., Jung, H.J., Yun, C.B., Spencer, B.F., and Agha, G. (2010). "Structural Health Monitoring of a Cable-Stayed Bridge using Smart Sensor Technology: Deployment and Evaluation." *Smart Structures and Systems*, 6(5): 439-460.

[48] Juang, J.N., and Pappa, R.S. (1985). "An Eigensystem Realization Algorithm for Modal Parameter Identification and Modal Reduction." *Journal of Guidance, Control and Dynamics*, 8(5), 620-627.

[49] Kim, C.Y., Jung, D.S., Kim, N.S., and Kwon, S.D., and Feng, M.Q. (2003). "Effect of Vehicle Weight on Natural Frequencies of Bridge Measured from Traffic-Induced Test." *Earthquake Engineering and Engineering Vibration*, 2(1), 109-115.

[50] Kim, J.T., Rye, Y.S., Cho, H.M., and Stubbs, N. (2003). "Damage Identification in Beam Type Structures: Frequency-Based Method vs Mode-Shape-Based Method." *Engineering Structures*, 25: 57-67.

[51] Kramer, M.A. (1991). "Nonlinear Principal Component Analysis using Auto-associative Neural Network." *AIChE J*, 37(2), 233-243.

[52] Lee, J.W., Kim, J.D., Yun, C.B., Yi, J.H. and Shim, J.M. (2002). "Health-Monitoring Method for Bridge under Ordinary Traffic Loading." *Journal of Sound and Vibration*, 257 (2): 247-264.

[53] Li, J., Wu, B., Zeng, Q.C., and Lim, C.W. (2010). "A Generalized Flexibility Matrix Based Approach for Structural Damage Detection." *Journal of Sound and Vibration*, 329(22), 4583-4587.

[54] Liao, Y., and Sodano, H.A. (2008). "Model of a Single Mode Energy Harvester and Properties for Optimal Power Generation." *Smart Material and Structures*, 17, 065026.

[55] Liao, Y., and Sodano, H.A. (2010). "Modeling and comparison of bimorph power harvesters with piezoelectric elements connected in parallel and series." *Journal of Intelligent Material Systems and Structures,* 21, 149.

[56] Lu, F., H. Lee and S. Lim (2004). "Modeling and Analysis of Micro Piezoelectric Power Generators for Micro-Electromechanical-Systems Applications." *Smart Materials and Structures*, 13, 57-63.

[57] Lynch, J.P., and Loh, K.J. (2006). "A Summary Review of Wireless Sensors and Sensor Networks for Structural Health Monitoring." *The Shock and Vibration Digest*, 38(2), 91-128.

[58] Lynch, J.P., Sundararajan, A., Law, K.H., Kiremidjian, A.S., Carryer, E., Sohn, H., and Farrar, C.R. (2003). "Field Validation of a Wireless Structural Health Monitoring System on the Alamosa Canyon Bridge." *Proceeding of the SPIE*, 5057, 267-278.

[59] Maser, K., Egri, R., Lichtenstein, A., and Chase, S. (1996). "Field Evaluation of a Wireless Global Bridge Evaluation and Monitoring System." *Proceeding of the 11th Conference on Engineering Mechanics*, Fort, Lauderdale, FL, 2, 955-958.

[60] Moser, P., and Moaveni, B. (2011). "Environmental effects on the identified natural frequencies of the Dowling Hall Footbridge." *Mechanical Systems and Signal Processing*, 25(7), 2336-2357.

[61] NBIS (1998). "National Bridge Inspection Standards." Code of Federal Regulation, U.S. Government Printing Office via GPO Access, revised April 1, 1998.

[62] Nguyen, V.H., Mahowald, J., Stefan, M., and Golinval, J.C. (2014). "Damage Detection in Civil Engineering Structure Considering Temperature Effect." *Proceedings of IMAC XXXII Dynamics of Coupled Structures*, Orlando, FL.

[63] Noh, N.Y., Nair, K.K.,Kiremigjian, A.S., and Loh, C.H. (2009). "Application of Time Series Based Damaged Detection Algorithms to the Benchmark Experiment at the National Center for Research on Earthquake Engineering (NCREE) in Taipei, Taiwan." *Smart Structures and Systems*, 5(1), 000-000.

[64] Pakzad, S., Fenves, G., Kim, S., and Culler, D. (2008). "Design and Implementation of Scalable Wireless Sensor Network for Structural Monitoring." *Journal of Infrastructure System,* 14(1), 89-101.

[65] Pandey, A. K., Biswas, M. and Samman, M. M. (1991). "Damage Detection from Changes in Curvature Mode Shapes." *Journal of Sound and Vibration*, 145(2): 321-332.

[66] Paradiso, J.A., and Starner, T. (2005). "Energy Scavenging for Mobile and Wireless Electronics." *Cognition*, 4, 18.-27.

[67] Patil, D.P., Maiti, S.K. (2003). "Detection of Multiple Cracks using Frequency Measurements." *Engineering Fracture Mechanics*, 70: 1553-1572.

[68] Peeters, B., Maeck, J., and De, R.G. (2001). "Vibration-based damage detection in civil engineering: excitation sources and temperature effect." *Smart material and Structures*, 10, 518-527.

[69] Pei J.S., Kappor, C., Graves-Abe, T.L., Sugeng, Y.P., and Lynch, J.P. (2008). "An Experimental Investigation of the Data Delivery Performance of a Wireless Sensing Unit Designed for Structural Health Monitoring." *Structural Control and Health Monitoring*, 15(4), 471-504.

[70] Pothisiri, T. and Hjelmstad, K. D. (2003). "Structural Damage Detection and Assessment from Modal Response." *Journal of Engineering Mechanics*, ASCE, 129(2): 135-145.

[71] Raghunathan, V., Kansal, A, Hsu, J., Friedman, J. and Srivastava, M. (2005). "Design Considerations for Solar Energy Harvesting Wireless Embedded Systems." *IEEE International Conference on IPSN.*

[72] Rice, J.A. (2009). "Flexible Smart Sensor Framework for Autonomous Full-Scale Structural Health Monitoring." UIUC ProQuest Dissertation and Theses.

[73] Rice, J.A., Mechitov, K.A., Sim, S.H., and Spencer, B.F. Jr. (2011). "Enabling Framework for Structural Health Monitoring using Smart Sensors." *Journal of Structural Control and Health Monitoring*, 18(5), 574-587.

[74] Roundy, S., and P.K. Wright. (2004). "A Piezoelectric Vibration Base Generator for Wireless Electronics." *Smart Materials and Structures*, 13, 1131-1142.

[75] Roundy, S., P.K. Wright, and J. Rabaey. (2003). "A Study of Low Lever Vibration as a Power Source for Wireless Sensor Nodes." *Computer Communication*, 26, 1131-1144.

[76] Roundy, S., Wright, R.K, and Rabacy, J.M. (2004). "Energy Scavenging for Wireless Sensor Networs" *Norwell: Kluwer Academic Publishers*.

[77] Seyedpoor, S.M. (2012). "A Two Stage Method for Structural Damage Detection using a Modal Strain Energy Based Index and Particle Swarm Optimization." *Internal Journal of Non-Linear Mechanics*, 47(1), 1-8.

[78] Shahruz, S.M. (2006). "Design of mechanical band-pass filters for energy scavenging." *Journal of Sound and Vibration*, 292, 987-998.

[79] Shi, Z.Y., Law, S.S., and Zhang, L.M. (2002). "Improved Damage Quantification from Elemental Modal Strain Energy Change." *Journal of Engineering Mechanics, ASCE*, 128(5), 521-529.

[80] Shin, S., and Hjelmstad, K. D. (1994). "Damage Detection and Assessment of Structural Systems from Measured Response." *Civil Engineering Studies*, SRS 593, UILUENG-94-2013, Univ. of Illinois at Urbana-Champaign.

[81] Sodano, H, Park, G., and Inman, D.J. (2004). "A Review of Power Harvesting from Vibration using Piezoelectric Materials." *Shock and Vibration Digest*, 36, 197-205.

[82] Sohn, H. (2003). "A Review of Structural Health Monitoring Literature: 1996 – 2001." No. LA-13976-MS. Los Alamos National Laboratory.

[83] Sohn, H., Worden, K., and Farrar, C.R. (2002). "Statistical Damage Classification under Changing Environmental and Operational Conditions." *Journal of Intelligent Material Systems and Structures*, 13(9), 561-574.

[84] Soyoz, S., and Feng, M.Q. (2009). "Long-term Monitoring and Identification of Bridge Structural Parameters." *Computer Aided Civil Infrastructure Engineering*, 24, 82-92.

[85] Spencer Jr., B.F., Ruiz-Sandoval, M. and Kurata, N. (2004). "Smart Sensing Technology: Opportunities and Challenges." *Structural Control and Health Monitoring* 11, 349-368.

[86] Spencer, B.F. Jr., and Cho, S. (2011). "Wireless Smart Sensor Technology for Monitoring Civil Infrastructure: Technology Development and Full-scale Applications." *The World Congress on Advances in Structural Engineering and Mechanics*.

[87] Spencer, B.F.,Jr., and Yun, C.B. (2010). "Wireless Sensor Advances and Application for Civil Infrastructure Monitoring." NSEL Report 024.

[88] Sun, Z.K., Li, G.M., and Geng, S.H. (2013). "Study on Stayed-Cable Health Monitoring." *Advanced in Intelligent Systems and Computing*, 180, 1091-1098.

[89] Van Overshcee, P. and Bart D.M. (1996). "Subspace Identification for Linear System." *Kluwer Academic Publishers*.

[90] Vold, H., Kundrat, J., Rocklin, G.T., Russel, R. (1982). "A Multi-Input Modal Estimation Algorithm for Mini-Computer." *SAE Technical Paper Series*, No. 820194.

[91] Wenzel, H. (2009). "Health Monitoring of Bridges." *John Wiley & Sons, Ltd*.

[92] Williams, C.B. and R.B. Yates. (1996). "Analysis of a micro-electric generator for microsystems." *Sensors and Actuators*, 52, 8-11.

[93] Wong, K.Y., Chan, W.Y.K., Man, K.L., Mak, W.L.N., and Lau, C.K. (2000b). "Structural Health Monitoring Results on Tsing Ma, Kap Shui Mum, and Ting Kau Bridges." Proceedings of SPIE, 3995.

[94] Wong, K.Y., Lau, C.K., and Flint, A.R. (2000a). "Planning and Implementation of the Structural Health Monitoring System for Cable-Supported Bridges in Hong Kong." *Proceeding of SPIE*, 3995.

[95] Worden, K. and Manson G. (2007) "The Application of Machine Learning to Structural Health Monitoring." *Philosophy Transactions of the Royal Society A*, 365: 515-537.

[96] Worden, K. and Manson, G. (2000). "Damage Detection using Outlier Analysis." *Journal of Sound and Vibration*, 229(3), 647-667.

[97] Worden, K., Sohn, H., and Farrar, C.R. (2002). "Novelty Detection in a Changing Environmental: Regression and Interpolation Approaches." *Journal of Sound and Vibration*, 258(4), 741-761.

[98] Xia, Y., Chen, B., Weng, S., Ni, Y., and Xu, Y. (2012). "Temperature Effect on Vibration Properties of Civil Structures, a Literature Review and Case Studies." *Journal of Civil Structural Health Monitoring*, 2(1), 29-46.

[99] Xue, H., Hu, Y., and Wang, Q. (2008). "Broadband piezoelectric energy harvesting devices using multiple bimorphs with different operating frequencies." *IEEE Transactions on Ultrasonic, Ferroelectrics, and Frequency Control*, 55(9), 2104-2108.

[100] Yen, C.I., Juang, C.K., Lee, W.F., Chen, C.H., Chen, M.C., and Lin, Y.C. (2014). "Application of a High-Tech Bridge Safety System in Monitoring the Performance of Xibin Bridge." *Proceedings of the ICE-Forensic Engineering*, 167(1), 38-52.

[101] Zhu, D., Tudor, M.J., and Beeby, S.P. (2010). "Strategies for Increasing the Operating Frequency Range of Vibration Energy Harvesters: A Review. " Measurement Science ad Technology, 21(2), 022001.